Thi-Qar University Journal for Engineering Sciences

ISSN 2075-9746

The English Section

Contents

Computational Study of Flow and Heat Transfer in a Sudden Expansion Channel with Inclined Obstacles

Khudheyer S. Mushatet
College of Engineering
Thi-qar University

Qais A. Rishak
College of Engineering
Basrah University

Mohsen H. Fagr
College of Engineering
Thi-qar University

Abstract

The laminar flow through an obstacled sudden expansion channel is numerically investigated. Rectangular adiabatic inclined obstacles mounted behind the expansion region on the upper and lower wall of the channel were used. The effects of obstacles inclination angle, obstacles length, obstacles thickness and the number of obstacles on the flow and thermal fields for different Reynolds number and expansion ratio were examined. The angle of obstacles inclination was taken in the direction of streamwise flow and ranged from 30° to 90°. Three values of expansion ratio(ER=H/h) equal to 1.5, 1.75 and 2 were used. The choice of values of Reynolds number takes the consideration of symmetry state. The body fitted coordinates system is used to transfer the considered physical problem to computational domain in order to treat the complexity arising from applicable the boundary conditions near the inclined obstacles. The governing stream-vorticity equations expressed in generalized coordinates system were transformed to algebraic equations by using finite difference method. The solution of these equations was done by iteration method. The obtained results showed that there is a significant effect of obstacles angle on the hydrodynamic characteristics. The performed tests of the present results with related published results showed that there is an acceptable agreement.

Key words Sudden expansion channel, Laminar flow, Obstacles.

الخلاصة

اجريت في هذا البحث دراسة عددية لجريان طباقي خلال قناة ذات توسع فجائي مزودة بعوائق مستطيلة المقطع، مائلة ومعزولة تمت اضافتها الى المجرى في منطقة التوسع على الجدارين العلوي والسفلي بصورة متناظرة. يهدف البحث الى معرفة مدى تأثير زاوية ميلان هذه العوائق وطولها وسمكها بالاضافة الى عددها على الخصائص الحركية والحرارية للجريان ولقيم مختلفة من رقم رينولدز وكذلك لنسب باعية مختلفة. شمل البحث زوايا ميلان للعوائق من ٣٠° الى ٩٠° كما تم خلال البحث دراسة ثلاث نسب باعية هي ١.٥، ١.٧٥ وكذلك ٢. تم الاخذ بنظر الاعتبار بقاء الجريان متناظر عند اختيار قيم عدد رينولدز. استخدمت طريقة مواءمة الاحداثيات للجسم لتحويل المسألة محل البحث من الوسط الفيزياوي الطبيعي الى الوسط الحسابي لمعالجة التعقيد الناجم عن وجود العوائق المائلة. المعادلات الحاكمة للجريان والدوامية والمعبر عنها بنظام الاحداثيات المعمم تم تحويلها الى معادلات خطية من خلال طريقة الفروق المحددة ثم حلها بطريقة التكرار. النتائج التي اظهرها البحث بينت ان هناك تأثيرا ملحوظا لزاوية ميلان العوائق على الخصائص الحركية. اظهرت المقارنات التي اجريت لنتائج البحث الحالي مع نتائج الابحاث المنشورة مقبولية عالية للنتائج الحالية.

Introduction

The flow in a sudden expansion channels is encountered in many engineering applications. Although the flow is considered simple, the complexities arise due to the separation and reattachment after the expansion region. In recent studies, an increasing interest is focused on energy conservation systems. These systems include heat exchangers, cooling of electronic devices and solar collectors. The large number of previous studies focused on hydrodynamic and thermal behavior of the flow behind sudden expansion geometry. Therefore, non-published studies were done on using an inclined solid obstacles mounted behind the expansion region, and as a result, the effects of these obstacles on dynamic behavior of the flow and enhancement of heat transfer. The laminar flow of Newtonian fluid in planar and axisymmetric sudden expansion was studied by Scott et al. [1]. They covered the steady state flow at Reynolds number up to 200 and expansion ratio of 1.5, 2, 3 and 4. The results showed that the reattachment length and the eddy center location vary linearly with Reynolds number, but the relative eddy intensity was an exponential function of Reynolds number. Tao tang and Ingham [2] studied the steady laminar flow past a sudden expansion for incompressible fluid. The study covered Reynolds numbers up to 1000 and uniform inflow. The results showed that the eddy length increased linearly with Reynolds number for both small and large values of expansion ratios. Baloch et al. [3] investigated numerically the incompressible Newtonian flows through two and three dimensional expansions. The sudden expansion geometry had a square cross section. The obtained results show that for Reynolds number up to 10, a significant vortex activity was generated by fluid inertia giving recirculation zone and vortex enhancement. Battaglia et al. [4] performed numerical simulations and bifurcation calculations for flow of Reynolds number up to 200 in a two-dimensional sudden expansion channel. They found that the critical Reynolds number decreased with increasing expansion ratio. Thiruvengadam et al. [5] demonstrated the effects of flow bifurcation on temperature and heat transfer distributions in plane symmetric sudden expansion. They verified that the maximum Nusselt number that occurs on lower stepped wall is larger than the one that develops on the upper stepped wall and it develops near the side wall and not at the center of the duct. Battaglia and Papadopoulos [6] investigated experimentally and by two- and three-dimensional simulations the effect of three dimensionality flows of Reynolds number from 150 to 600 past 2:1 symmetric sudden expansion channel of 6:1 aspect ratio. They showed that when two-dimensional simulations were performed using the effective expansion ratio, the new results agreed well with the three-dimensional simulations and the experiments. The laminar flow through an axisymmetric sudden expansion using real-time digital particle

image velocimetry was studied by Hammed et al. [7]. They verified that the reattachment length and redevelopment length downstream of reattachment were linear functions of Reynolds number. The steady bifurcation phenomena for three dimensional flows through a plane–symmetric sudden expansion was investigated numerically by Chiang et al [8]. They showed that the bifurcation was dependent on flow Reynolds number, channel aspect ratio and expansion ratio. Simulations of three dimensional laminar forced convection in a plane symmetric sudden expansion were performed by Nie and Armaly [9]. They verified that the maximum Nusselt number was located inside the primary recirculation flow region and its location did not coincid with swirling flow impingement. The laminar incompressible flow in a symmetric plane sudden expansion was studied numerically by Wahba [10] where different iterative solvers on calculation of the bifurcation point were tested. He verified that the type of inflow velocity profile, whether uniform or parabolic has a significant effect on the onset of bifurcation. In the present work, a computational study has been made to study the dynamic of the flow behavior and thermal field in an obstacled sudden expansion channel. Inclined solid obstacles were mounted on upper and lower wall of the channel after the expansion region. The obstacles were inclined towards the flow stream. Different values of angle of inclination (AOI) $30° \leq AOI \leq 90°$ were used. The angle of inclination of obstacles, obstacles length and number of obstacles are studied for different values of Reynolds number and expansion ratio. The symmetry state is considered. The aim of the present study is to show the effect of inclined obstacles mounted behind expansion region on the flow behavior and thermal field.

1. Model description

The considered physical model is shown in Fig.1. It represents the upper half of plane symmetric sudden expansion. The upstream height is (h) and the downstream height is (H). The geometry provides a configuration within expansion ratio (ER=H/h) equals to 1.5, 1.75 and 2. The assumed fully developed flow at inlet leads to reduce the upstream length (L1) to be equal to the upstream height (h). The downstream length (L2) equals to 14 times the upstream height is considered where the effect of obstacles is vanished. The insulated obstacles were mounted symmetrically on the upper and lower walls of the expansion region and equal distance (l) between the obstacles was considered. The number of obstacles is varying as 1 and 3. Three obstacle lengths (Lo) equal to 0.1H, 0.15H and 0.2H and three obstacles thickness (th) equal to h/24, h/12 and h/6 were studied. Three values of angles of inclination (AOI) equal to 30°, 60° and 90° were examined. Different values of Reynolds

number (Re = 50, 100, 150 and 200) were selected taking by consideration the achievement of symmetric flow conditions.

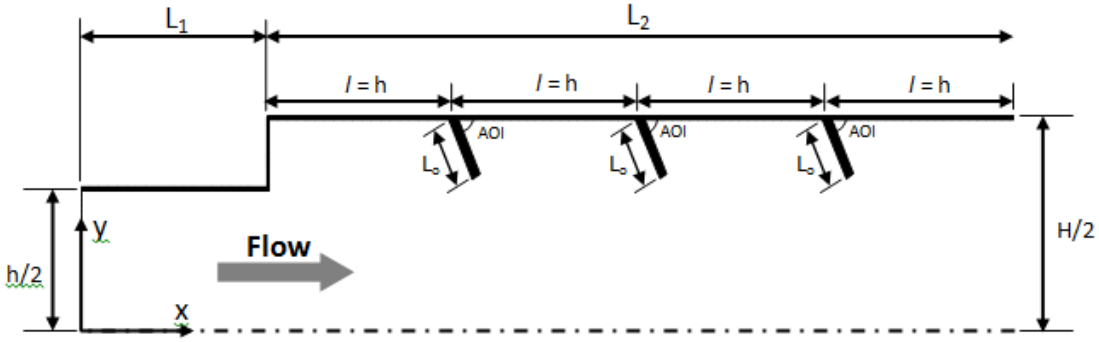

Fig.1 Schematic diagram of the considered problem

2.1. Mathematical model

The continuity, Navier–Stokes and energy equations for two dimensional steady state incompressible flow are described below by using the stream function - vorticity formulation after adopting the following assumptions:

- Fully developed at inlet.
- Constant thermo physical properties of the working fluid (air).
- Non-slip flow.
- Constant temperature at the expansion region walls.

Continuity equation:

$$\frac{\partial u}{\partial x}+\frac{\partial v}{\partial y}=0 \qquad (1)$$

Momentum equation in x-direction:

$$\frac{\partial u}{\partial t}+u\frac{\partial u}{\partial x}+v\frac{\partial u}{\partial y}=\upsilon\left(\frac{\partial^2 u}{\partial x^2}+\frac{\partial^2 u}{\partial y^2}\right)-\frac{1}{\rho}\frac{\partial p}{\partial x} \qquad (2)$$

Momentum equation in y-direction:

$$\frac{\partial v}{\partial t}+u\frac{\partial v}{\partial x}+v\frac{\partial v}{\partial y}=\upsilon\left(\frac{\partial^2 v}{\partial x^2}+\frac{\partial^2 v}{\partial y^2}\right)-\frac{1}{\rho}\frac{\partial p}{\partial y} \qquad (3)$$

Energy equation:

$$\frac{\partial T}{\partial t}+u\frac{\partial T}{\partial x}+v\frac{\partial T}{\partial y}=a\left(\frac{\partial^2 T}{\partial x^2}+\frac{\partial^2 T}{\partial y^2}\right) \qquad (4)$$

Differentiate Eq. (2) with respect to y and Eq.(3) with respect to x and then subtract Eq. (2) from Eq. (3) and rearrange the result:

$$\frac{\partial}{\partial t}(\frac{\partial v}{\partial x}-\frac{\partial u}{\partial y})+\frac{\partial u}{\partial x}(\frac{\partial v}{\partial x}-\frac{\partial u}{\partial y})+\frac{\partial v}{\partial y}(\frac{\partial v}{\partial x}-\frac{\partial u}{\partial y})+u\frac{\partial}{\partial x}(\frac{\partial v}{\partial x}-\frac{\partial u}{\partial y})$$
$$+v\frac{\partial}{\partial y}(\frac{\partial v}{\partial x}-\frac{\partial u}{\partial y})=\upsilon\left[\frac{\partial^2}{\partial x^2}(\frac{\partial v}{\partial x}-\frac{\partial u}{\partial y})+\frac{\partial^2}{\partial y^2}(\frac{\partial v}{\partial x}-\frac{\partial u}{\partial y})\right] \quad (5)$$

from the definitions of stream function and vorticity:

$$d\varphi = udy - vdx \quad (6)$$

$$\Omega=\frac{\partial v}{\partial x}-\frac{\partial u}{\partial y} \quad (7)$$

So, the governing equations will be:

$$\frac{\partial^2\varphi}{\partial x^2}+\frac{\partial^2\varphi}{\partial y^2}=-\Omega \quad (8)$$

$$\frac{\partial\Omega}{\partial t}+\frac{\partial\varphi}{\partial y}\frac{\partial\Omega}{\partial x}-\frac{\partial\varphi}{\partial x}\frac{\partial\Omega}{\partial y}=\upsilon\left(\frac{\partial^2\Omega}{\partial x^2}+\frac{\partial^2\Omega}{\partial y^2}\right) \quad (9)$$

$$\frac{\partial T}{\partial t}+\frac{\partial\varphi}{\partial y}\frac{\partial T}{\partial x}-\frac{\partial\varphi}{\partial x}\frac{\partial T}{\partial y}=a\left(\frac{\partial^2 T}{\partial x^2}+\frac{\partial^2 T}{\partial y^2}\right) \quad (10)$$

The above equations are dimensionlessed via using the following parameters :

$$X=\frac{x}{h}\ ,\quad Y=\frac{y}{h}\ ,\quad U=\frac{u}{u_\circ}\ ,\quad V=\frac{v}{u_\circ}\ ,\quad \psi=\frac{\varphi}{hu_\circ}\ ,\quad \tau=\frac{u_\circ t}{h}\ ,\quad \omega=\frac{\Omega h}{u_\circ}\ ,\quad \theta=\frac{T-T_\circ}{T_w-T_\circ}$$

So, equations (8-10) will become :

$$\frac{\partial^2\psi}{\partial X^2}+\frac{\partial^2\psi}{\partial Y^2}=-\omega \quad (11)$$

$$\frac{\partial\omega}{\partial\tau}+\frac{\partial\psi}{\partial Y}\frac{\partial\omega}{\partial X}-\frac{\partial\psi}{\partial X}\frac{\partial\omega}{\partial Y}=\frac{1}{\mathrm{Re}}\left(\frac{\partial^2\omega}{\partial X^2}+\frac{\partial^2\omega}{\partial Y^2}\right) \quad (12)$$

$$\frac{\partial\theta}{\partial\tau}+\frac{\partial\psi}{\partial Y}\frac{\partial\theta}{\partial X}-\frac{\partial\psi}{\partial X}\frac{\partial\theta}{\partial Y}=\frac{1}{\mathrm{Re}\,\mathrm{Pr}}\left(\frac{\partial^2\theta}{\partial X^2}+\frac{\partial^2\theta}{\partial Y^2}\right) \quad (13)$$

2.2. Grid generation

Due to presence of inclined obstacles, the physical domain becomes non-rectangular. So a suitable treatment for obstacles boundary conditions is needed to capture the inaccuracy arises for imposing a rectangular domain on this complex boundary. The grid generation method proposed by Thompson [11] is used to map the non- rectangular grids in physical domain into rectangular one in computational space. The most popular partial differential equation used for any complex-shaped bodies in two dimensional zone is an elliptic poison equation:

$$\zeta_{xx} + \zeta_{yy} = P(\zeta,\eta) \quad (14)$$

$$\eta_{xx} + \eta_{yy} = Q(\zeta,\eta) \quad (15)$$

Where P and Q are known functions used for controlling the grids clustering. It is worth to mention here that the grids adopted for the present work were generated at $P(\zeta, \eta) = Q(\zeta, \eta) = 0$.

This process is accomplished by addling the boundary conditions which specify ζ and η as functions of x and y. The dependent and independent variables are interchanged to produce a system of elliptic differential equations.

So, the governing equations, Eq. 11-13 will become:

$$\omega_\tau + \left(-\psi_\zeta \omega_\eta + \psi_\eta \omega_\zeta\right)/J = \left(\lambda\omega_\zeta + \sigma\omega_\eta + \alpha\omega_{\zeta\zeta} - 2\beta\omega_{\zeta\eta} + \gamma\omega_{\eta\eta}\right)/J^2\,\mathrm{Re} \quad (16)$$

$$\theta_\tau + \left(-\psi_\zeta \theta_\eta + \psi_\eta \theta_\zeta\right)/J = \left(\lambda\theta_\zeta + \sigma\theta_\eta + \alpha\theta_{\zeta\zeta} - 2\beta\theta_{\zeta\eta} + \gamma\theta_{\eta\eta}\right)/J^2\,\mathrm{Re}\,\mathrm{Pr} \quad (17)$$

$$\lambda\psi_\zeta + \sigma\psi_\eta + \alpha\psi_{\zeta\zeta} - 2\beta\psi_{\zeta\eta} + \gamma\psi_{\eta\eta} = -J^2\omega \quad (18)$$

Eq.16-18 are discretized by using finite difference scheme and then solved by iteration method with succesive over relaxation method (SOR).

2.3. Boundary conditions

In order to solve the mathematical model, the following boundary conditions were imposed On the upper wall:

$$\psi = 1 \quad , \quad \omega = \frac{-\alpha}{J^2}\psi_{\zeta\zeta}\ [12] \quad , \quad \theta = 1$$

On the obstacles:

$$\psi = 1 \quad , \quad \omega = \frac{-\alpha}{J^2}\psi_{\zeta\zeta}\ [12] \quad , \quad \frac{\partial\theta}{\partial n} = 0$$

Where n is a unit normal vector. On the symmetric line:

$$\psi = 0 \quad , \quad \frac{\partial\theta}{\partial Y} = 0$$

Fully developed conditions at inlet were imposed:

$$\frac{\partial\phi}{\partial X} = 0 \quad , \quad \psi = \psi(Y)$$

Where ϕ represents ψ, ω and θ.

At exit, to insure the smooth transition at the flow boundary, the following boundary conditions are used $\frac{\partial\psi}{\partial X} = 0$, $\frac{\partial\omega}{\partial X} = 0$, $\frac{\partial\theta}{\partial X} = 0$

2.4.Grid dependency

To ensure that the hydrodynamic and thermal parameters are not affected by the mesh, different grid densities were examined for each expansion ratio ER. For ER = 1.5, the grid densities were (390×15), (390×30) and (600×45). For ER = 1.75, the grid densities were (390×21), (390×35) and (600×48). While for ER = 2, the grid densities were (390×30), (390×40) and (600×60). The results showed that increasing in grid density more than (390×30), (390×35) and (390×40) for ER = 1.5, 1.75 and 2 respectively has no significant effect on the results as shown in Fig.2 and Fig.3. So, these grid densities were selected in the present work.

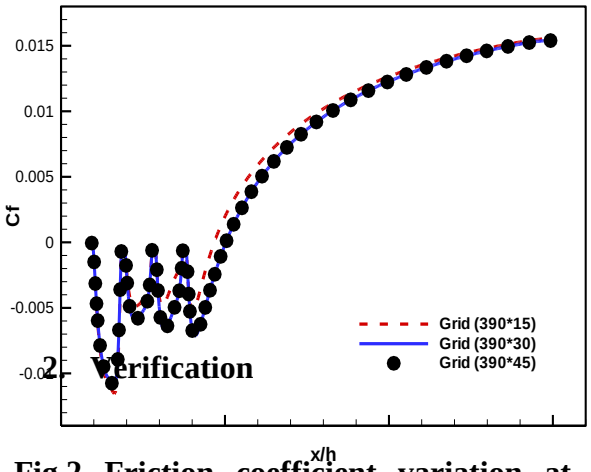

Fig.2 Friction coefficient variation at various grids at Re=150for ER=1.5, three obstacles, Lo=0.15H, th= h/24 and AOI=90°.

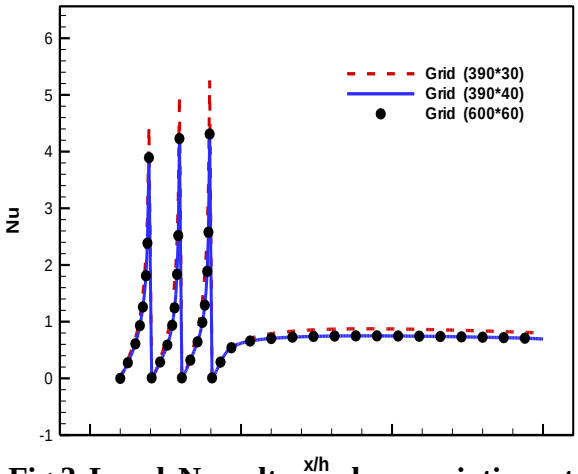

Fig.3 Local Nusselt number variation at various grids at Re=150for ER=2, three obstacles, Lo=0.2H, th= h/24 and AOI=60°.

2. Verification

3. Verification

To verify the present built home computer program, two tests were performed with related published results as show in Fig. 4 and Fig. 5. As the figures show, the comparison indicated an acceptable agreement.

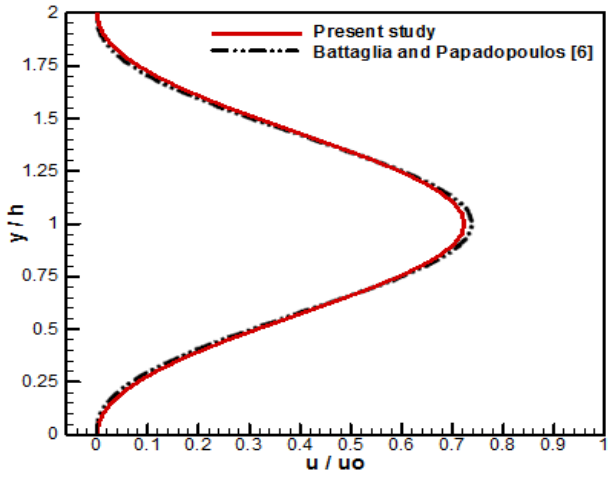

Fig.4 Comparison of present results of dimensionless streamwise velocity for ER=2 and x/h=4.5 at Re=171 with the predicted results of Battaglia and Papadopoulos [6].

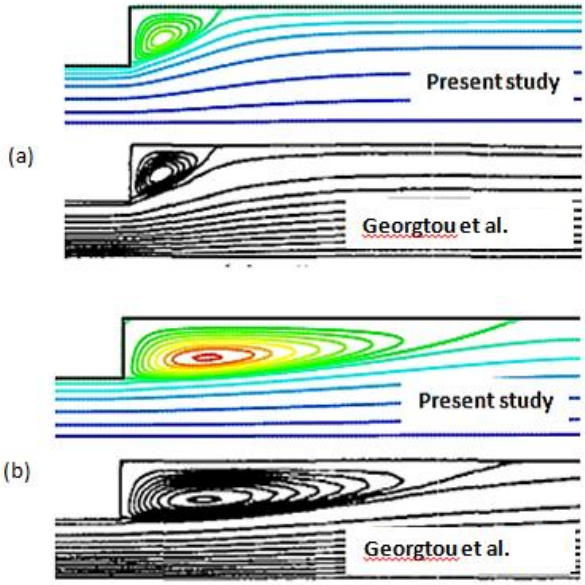

fig. 5 Comparison of present results of recirculation region for 2:1 expansion duct with the published results of Georgtou et al. [13].(a) Re =10. (b) Re =50.

4. Symmetry and asymmetry

fig.6 shows the streamwise velocity contours of flow at Re = 200 inside a channel of expansion ratio equals to 1.5 (case a), 1.75 (case b) and 2 (case c). This figure shows that at this Reynolds number, a two recirculation zones of equal size mounted symmetrically on upper and lower the centerline of the channel are developed. The streamwise velocity is primarily positive in the direction of flow except for the two recirculation zones that form immediately downstream of the expanding channel where the flow attaches the upper and lower walls. An effect of expansion ratio is that as it increases, the recirculation zone becomes larger at same Reynolds number due to the decreasing in the pressure drop. This effect can be seen by comparison cases a, b and c of fig.6.

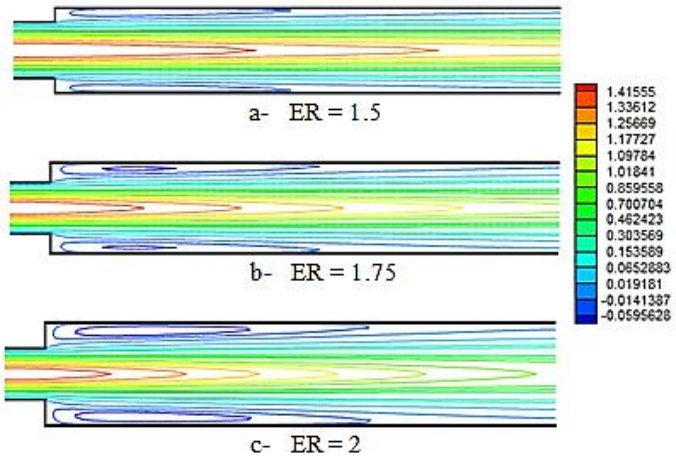

fig.6 Streamwise velocity distribution with symmetric flow pattern at Re=200.

The symmetry will disappear as Reynolds number accedes the critical Reynolds number as shown in fig.7 where the flow leaves the symmetric state (case a) to asymmetric state (case b) in which different sizes of recirculation zones are formed along the upper and lower walls. In this study, the symmetry state is taken in consideration which means that the values of studied Reynolds number will not accede 200.

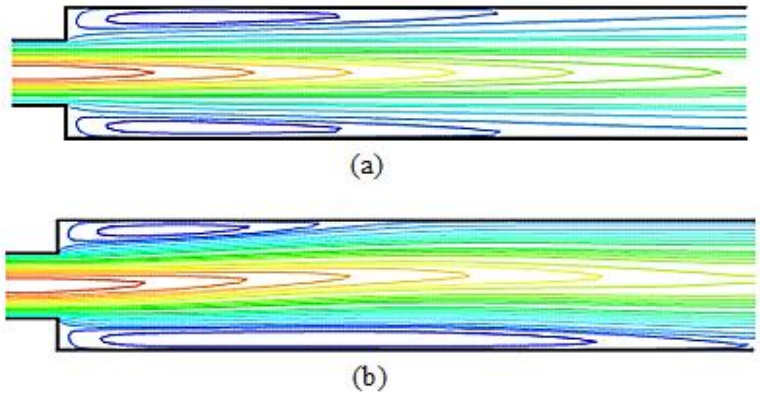

fig.7 Streamwise velocity contours for ER=2. (a) at Re = 200, (b) at Re =230.

5. Results and discussions

The two dimensional incompressible laminar flow in a sudden expansion obstacled channel has been numerically studied. Effects of number of obstacles, angle of inclination of the obstacles (AOI), length of obstacles (L_O) and Reynolds number (Re) on hydrodynamic and thermal parameters were tested for different expansion ratios.

5.1. Effects of number of obstacles on the hydrodynamic and thermal fields

The effect of number of obstacles on the flow structure at constant Reynolds number is shown in Fig. 8. The stream function contours and its recirculation zone for cases of no obstacles, one obstacle and three obstacles are shown. As the obstacles interrupt the development of the boundary layer, the recirculation zone downstream the obstacles is induced due to the flow separation. Therefore, increasing number of obstacles increases number of recirculation areas. The figure shows that the recirculation zone of the non obstacled channel develops to a longer zone of two recirculation areas created by adding one obstacle and by adding three obstacles, it becomes more longer with four recirculation areas.

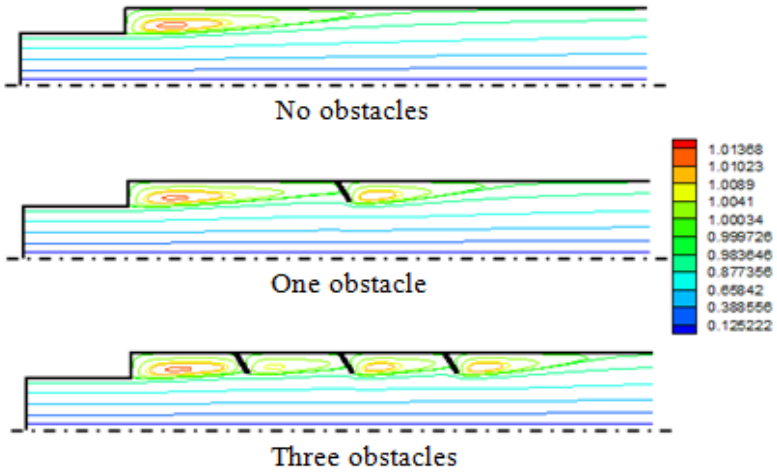

Fig. 8 Stream function contours at Re=150 for ER=1.5, L_O=0.15H and AOI=60°.

Fig.9 shows the effect of adding obstacles on the reattachment length. It is shown that the reattachment length is a linear function of the Reynolds number. It is also found that if the straight line representing reattachment length-Reynolds number relationship for not obstacled channel was to be extended, it will pass through the origin point. This trend is expected considering that the average shear rate at any chosen fixed streamwise distance normalized by the reattachment length is nearly constant [7]. Adding obstacles will remain the linear function of reattachment length-Reynolds number relationship but if it was to be extended, it will not pass through the origin. The extended line will shift to pass through a point represents the point of remote separation due to presence of obstacle. Note that the point of separation due to obstacle coincides with the free edge of the obstacle. Also, increasing number of obstacles increases reattachment length due to increasing flow separation.

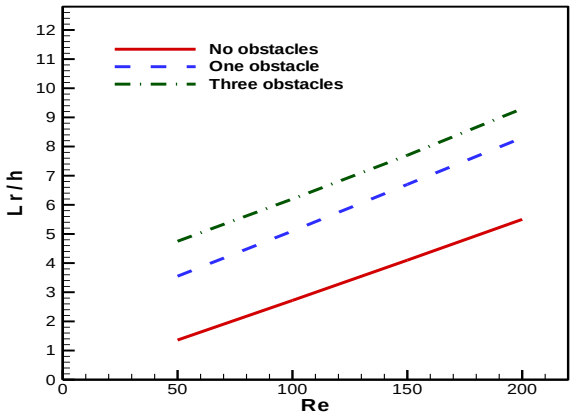

Fig. 9 Reattachment length-Reynolds number relationships for different obstacles number of AOI = 60° for ER = 1.75.

Fig.10 shows the average friction coefficient for the cases of different numbers of obstacles with respect to the Reynolds number. The friction coefficient changes its sign from negative to positive at the reattachment point. So, the longer recirculation region obtained by increasing number of obstacles will remain the negative sign friction coefficient for a longer axial distance. Therefore, the figure shows that average friction coefficient decreases by adding one obstacle, and more decreasing is shown by increasing obstacles number.

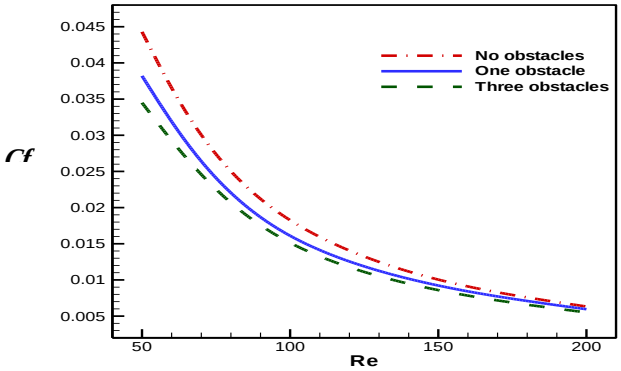

Fig. 10 Average friction coefficient at upper wall of expansion region with respect to Reynolds number for ER=1.5, L_O=0.15H and AOI=60°.

Fig. 11 represents the contours of dimensionless temperature for different number of obstacles. As the figure shows, the zone of high fluid temperature lies in the obstacled channel. The cause arises to increase recirculation zones due to presence of obstacles which increase the mixing and heat losses.

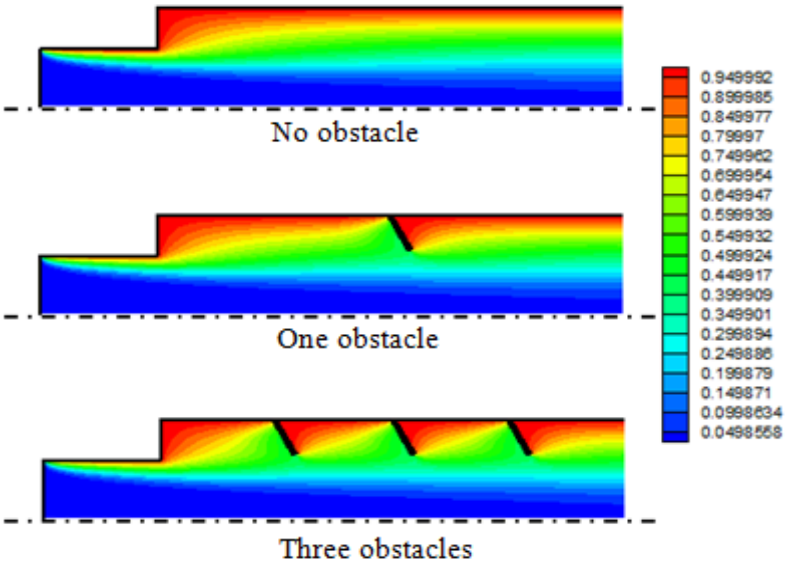

Fig. 11 Dimensionless temperature distribution at Re=150 for ER=1.75, L_O=0.2H and AOI=60°.

Fig. 12 shows the average Nusselt number variation with respect to the Reynolds number for cases of different obstacles number. As the obstacles number increases, the average Nusselt number increases. The increasing in the average Nusselt number is due to the intense mixing by the induced vortex.

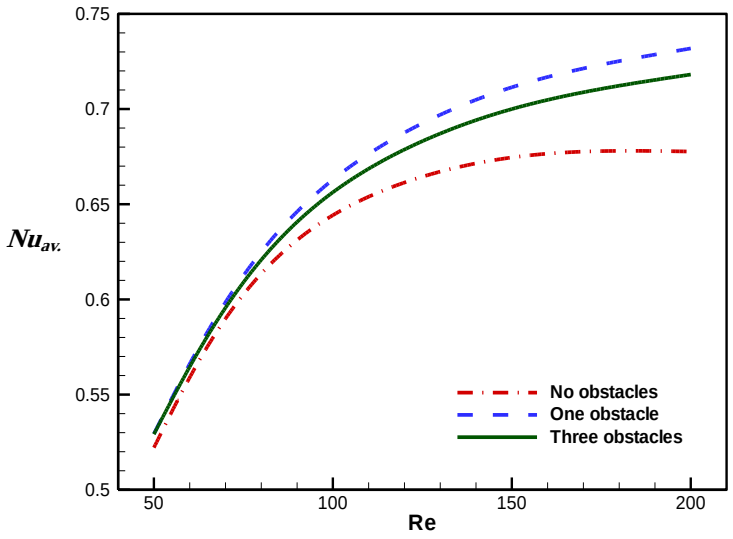

Fig. 12 Average Nusselt number at upper wall of expansion region with respect to Reynolds number for ER=2, L_O=0.2H and AOI=60°.

Table (1) shows the percentages increasing in the average Nusselt number when one and three obstacles are added comparing with case of non-obstacled channel.

Table (1) percentages increasing in the average Nusselt number for the case of ER = 1.5 with obstacles of L_O = 0.15H, th = h/6 and AOI = 90° at different Reynolds number.

No. of obstacles	Re = 50	Re = 100	Re = 150	Re = 200
1	32.503 %	25.712 %	23.219 %	21.852 %
3	59.284 %	51.203 %	47.947 %	46.133 %

5.2. Effects of the angle of inclination of obstacles on the hydrodynamic and thermal fields

The stream function distribution for different values of angle of inclination is seen in Fig. 13. As the figure shows, a vortex is observed downstream of the obstacles, which was induced due to the flow separation. The vortex was located close to the solid wall and its height was approximately equal to the extent of the flow blockage by the obstacles. The figure shows that the obstacles inclination angle has an effect on the area of the recirculation zone behind the obstacle. When the angle of inclination (AOI) increases from 30° to 60°, the recirculation zone becomes larger in its long and height. However, with further increment in AOI to 90°, it becomes smaller. The reason of this behavior is that the inclined obstacle will control the flow direction and as its angle increases from 30° to 60°, the flow toward duct center increases which enlarges the recirculation zone. But as its angle increases from 60° to 90°, the flow toward the duct center decreases compared with the flow toward the duct wall. However, the case of AOI =30° indicates the shortest recirculation zone.

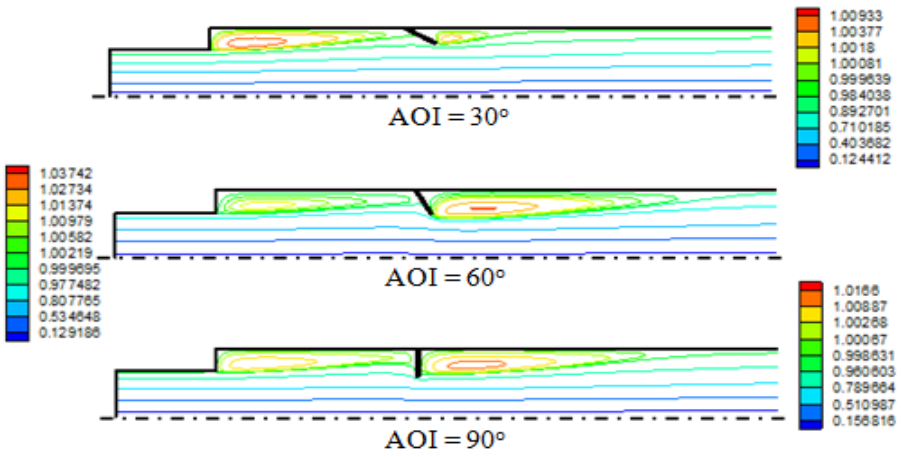

Fig. 13 Stream function contours at Re=150 for one obstacle case of ER=1.5 and L_O=0.2H.

Fig. 14 shows the effect of the angle of obstacles inclination on the reattachment length. Followed the separation behavior, it is shown that as the angle increases from 30° to 60°, the reattachment increases. But, as it increases from 60° to 90°, the reattachment length decreases but it remains larger than that for the case of 30°.

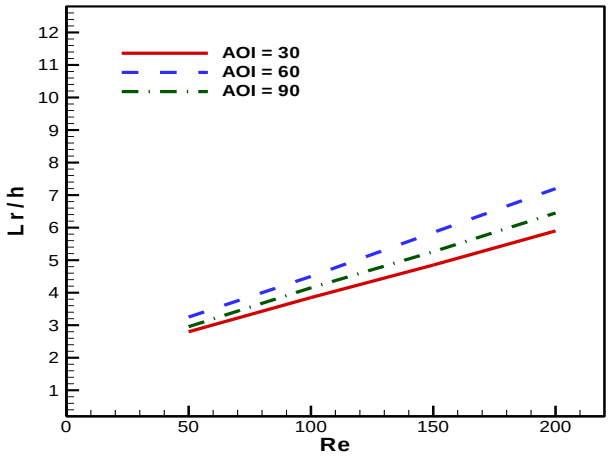

Fig. 14 Reattachment length for obstacled channels with one obstacle of L_O = 0.15H for ER = 1.75.

The effect of the obstacle inclination on the average friction coefficient ($C_{f\,av.}$) is shown in Fig. 15. It can be seen that the average friction coefficient for the case(AOI=60º) is less than that for other cases specially at low Reynolds number due to increasing in the recirculation region in which it still with negative sign for longer channel length.

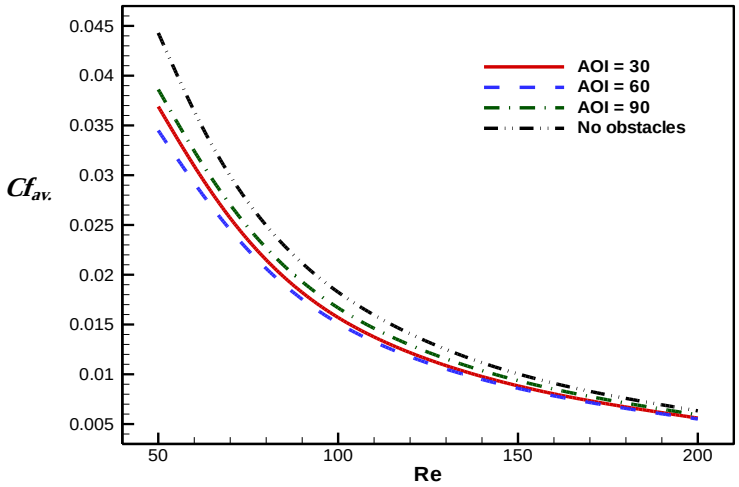

Fig. 15 Average friction coefficient at upper wall of expansion region for three obstacles case of ER=1.5 and L_O=0.15H.

Table (2) shows the percentages decreasing in the average friction coefficient when three obstacles of different inclination are added comparing with those of not obstacled channel.

Table (2) percentages decreasing in the average friction coefficient for the case of ER = 2, three obstacles of th = h/24 and L_O=0.15H at different Reynolds number.

AOI	Re = 50	Re = 100	Re = 150	Re = 200
30°	14.611 %	26.285 %	34.094 %	34.211 %
60°	16.712 %	28.936 %	45.140 %	50.712 %
90°	7.915 %	24.201 %	39.312 %	40.976 %

Fig. 16 shows the dimensionless temperature distribution for different values of obstacles inclination angles. Due to the higher improved mixing that obtained by increasing in the area of the recirculation zone when AOI = 60°, a better temperature distribution enhancement is seen.

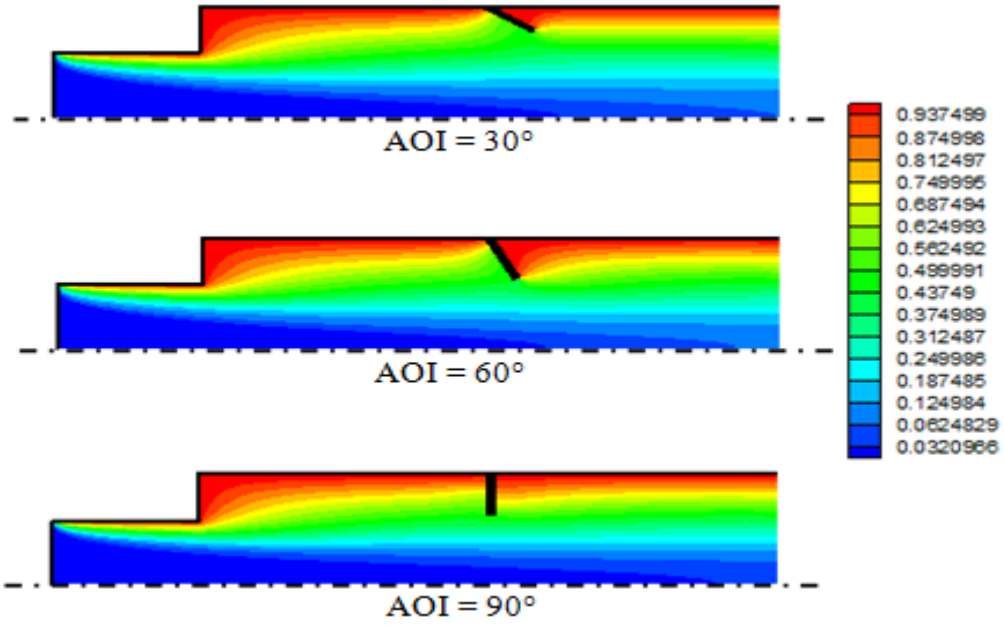

Fig. 16 Dimensionless temperature distribution at Re =100 for one obstacle case of ER=1.75 and L_O=0.2H.

The improvment in the Nusselt number by changing obstacles inclination angle can be seen in Fig. 17. This figure shows that the case of AOI = 60° obtains larger recirculation region, the average Nusselt number for this case has higher values as compared with other cases. Also, as Reynolds number increases, the difference between the average Nusselt number of different AOI cases increases as a result to the different increasing in the recirculation zones.

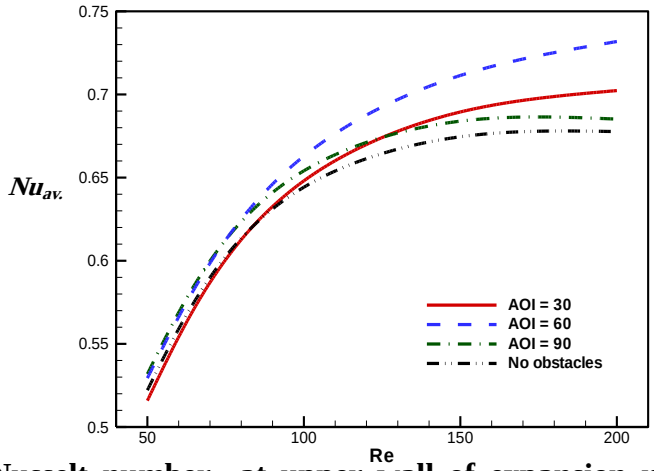

Fig. 17 Average Nusselt number at upper wall of expansion region with respect to Reynolds number for one obstacle case of ER=2 and L_O=0.2H.

5.3. Effect of obstacles length on the hydrodynamic and thermal fields

Fig. 18 shows the stream function contours with various inclined obstacles length L_O. It can be seen that more streamlines will separate due to increase the length of these obstacles which leads to increase the area of the recirculation zone downstream the obstacles as a result of the increasing in the pressure drop behind the obstacles.

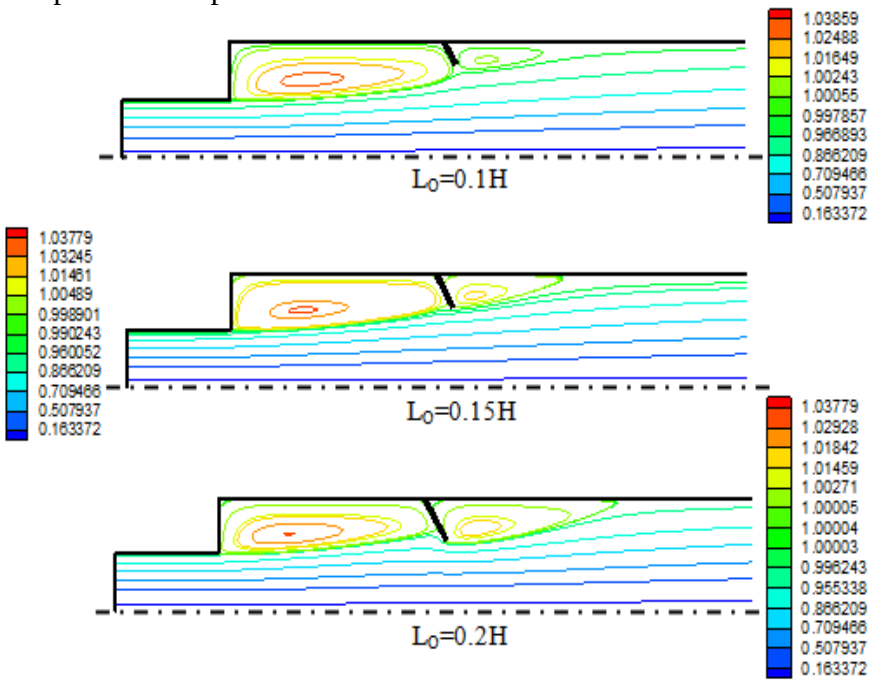

Fig. 18 Stream function contours at Re=50 for ER=2, one obstacle case and AOI=60°.

Fig. 19 shows the effect of obstacles length on the reattachment length. It is shown that as the obstacles length increases, the reattachment length increases due to increasing in the size of recirculation zone.

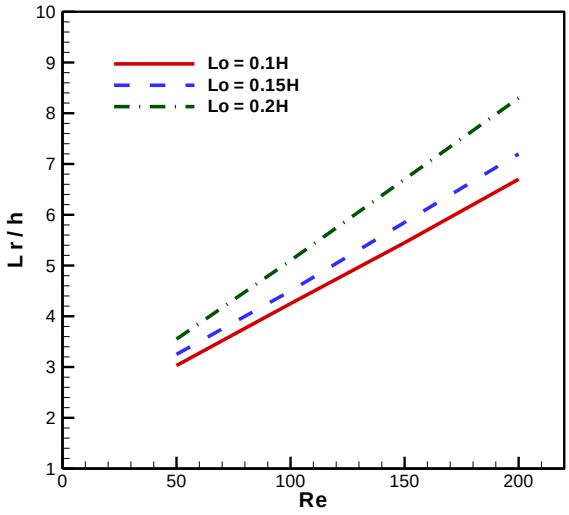

Fig. 19 Reattachment length-Reynolds number relationships for obstacled channels with one obstacle of AOI = 60° for ER = 1.75.

Fig. 20 shows the average friction coefficient for different inclined obstacle lengths with respect to the Reynolds number. As seen in this figure, the value of average friction coefficient for L_O=0.2H is lower than those of L_O=0.15H and 0.1H due to increase in the separation zone which leads the friction coefficient to remain with negative sign for longer channel length. Also, this figure shows that the dropping in average friction coefficient and its difference between the compared cases is decreased as the Reynolds number increases.

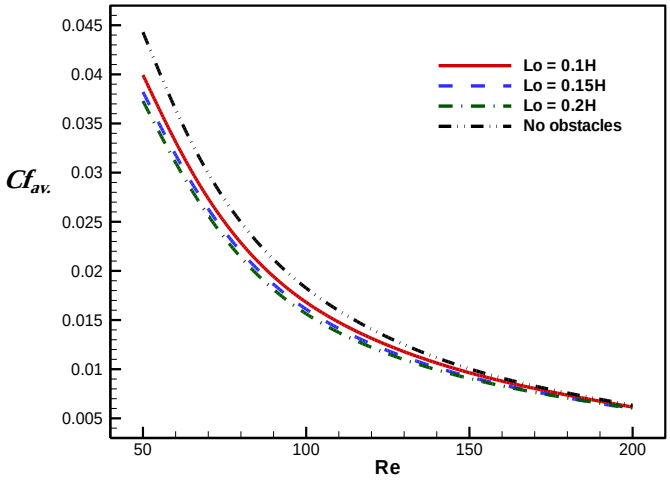

Fig. 20 Average friction coefficient at upper wall of expansion region with respect to Reynolds number for ER=1.5, one obstacle case and AOI =60°.

Table (3) shows the percentages decreasing in the average friction coefficient when three obstacles of different length are added comparing with those of non obstacled channel case.

Table (3) percentages decreasing in the average friction coefficient for the case of ER = 1.5, three obstacles of th = h/24 and AOI = 90° at different Reynolds numbers.

L_O	Re = 50	Re = 100	Re = 150	Re = 200
o.1H	7.123 %	4.301 %	2.887 %	3.542 %
0.15H	12.819 %	8.641 %	6.721 %	6.325 %
0.2H	15.031 %	13.934 %	13.203 %	12.001 %

Fig. 21 shows the dimensionless temperature distribution for cases of different inclined obstacle lengths (L_O). It is shown through this figure that the temperature distribution enhances as obstacle length increases specially at higher temperatures zone due to the improving in the fluid mixing.

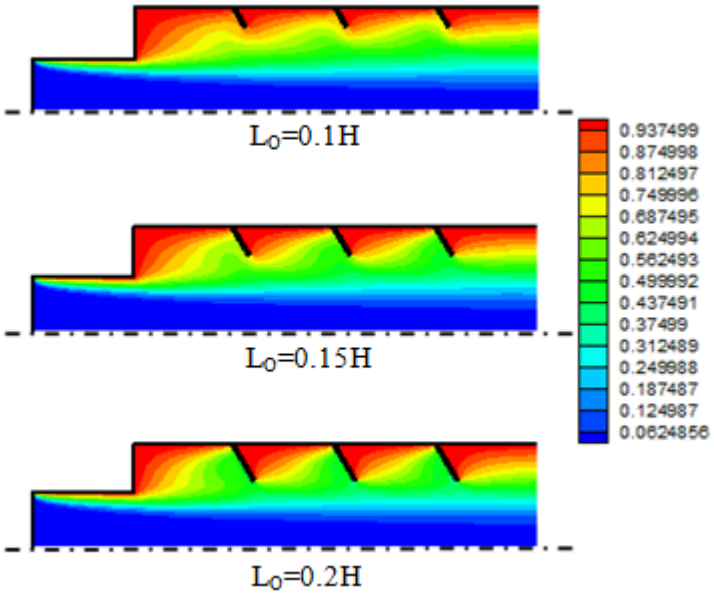

Fig. 21 Dimensionless temperature distribution at Re=200 for ER=2, three obstacle case and AOI=60°.

Fig. 22 shows the effect of obstacle length L_O on the average Nusselt number $Nu_{av.}$. It can be seen that that as the obstacle length increases, the average Nusselt number increases especially at higher Reynolds number. Also, there is a coincidence in the average Nusselt numbers for obstacles length L_O = 0.15H and L_O = 0.2H for (50≤ Re ≤100) is shown in this figure.

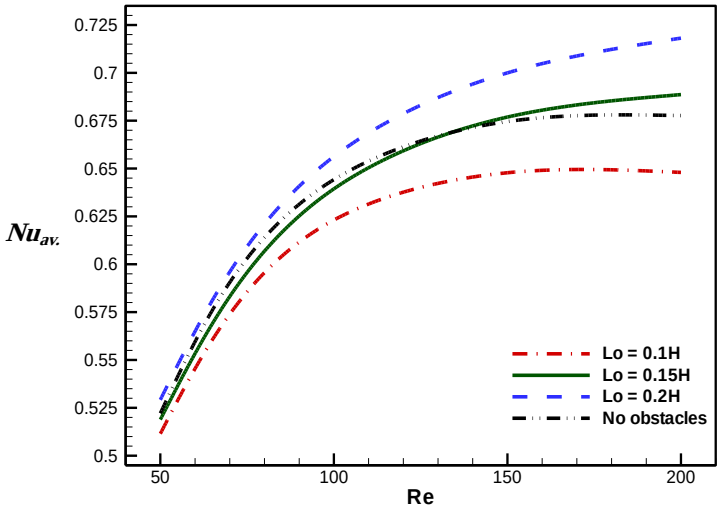

Fig. 22 Average Nusselt number at upper wall of expansion region with respect to Reynolds number for ER=2, three obstacles case and AOI =60°.

6. Conclusions

The laminar flow through a sudden expansion obstacled channel has been numerically analyzed. The obstacles were inclined towards the main flow stream. Different angles of inclination were tested as $30° \leq AOI \leq 90°$. The obstacles length (L_O) was changed as $0.1H \leq L_O \leq 0.2H$. The following conclusions can be obtained from the present study:

1- Increasing number of obstacles leads to decrease the friction coefficient and increase Nusselt number.

2- Increasing angle of inclination towards the main stream increasing the average rate of heat transfer. However, this increasing continues till AOI = 60° after that the rate of heat transfer decreases. The maximum values of average Nusselt number were noticed at AOI = 60°.

3- Increasing obstacles length leads to increase the rate of heat transfer and decrease the friction coefficient for all the studied angles of inclination.

4- Adding obstacles will shift the straight line that represents the reattachment length-Reynolds number relationship to pass through a point represents the point of remote separation.

7. Nomenclature

$C_{f\,av.}$ - Average coefficient of friction, [-]
ER - Expansion ratio (= H / h), [-]
H - Dimensionless downstream Channel height, [-]
h - Dimensionless upstream Channel height, [-]
J - Jacobian of direct transformation
$Nu_{av.}$ - Average Nusselt number, [-]
Re - Reynolds number(=Uh/ν), [-]
X ,Y - Dimensionless coordinates, [-]
ζ , η - computational domain coordinates
φ - stream function, [m^2/s]
ψ - dimensionless stream function, [-]
Ω - vortisity, [1/s]
ω - dimensionless vortisity, [-]
θ - dimensionless temperature, [-]

Pr - prandle number, [-]
T - temperature, [k]
U - Dimensionless streamwise velocity, [-]

α, β, γ – Transformation parameters
σ, λ - Geometrical parameters

References

[1] Scott P. S., Mirza F. A., Vlachopoulos J., A finite element analysis of laminar flows through planar and axisymmetric abrupt expansions, Computers and Fluids vol. 14, No. 4, pp. 423-432, (1986).

[2] Tao Tang, Ingham D. B., Multigrid solutions of steady two-dimensional flow past a cascade of sudden expansions, Computers and Fluids vol. 21, No. 4, pp. 647-660, (1992).

[3] Baloch A., Townsend P., Webster M. F., On two and three dimensional expansion flows, Computers and Fluids vol. 24, No. 8, pp. 863-882, (1995).

[4] Battaglia Francine, Simon J. Tavenery, Anil K. Kulkarniz, Charles L. Merkle, Biforcation of low Reynolds number flows in symmetric channels, American Institute of Aeronautics and Astronautics, (1996).

[5] Thiruvengadam M., Nie J. H., Armaly B.F., Bifurcated three-dimensional forced convection in plane symmetric sudden expansion, International Journal of Heat and Mass Transfer 48, pp. 3128–3139, (2005).

[6] Battaglia Francine, George Papadopoulos, Bifurcation Characteristics of Flows in Rectangular Sudden Expansion Channels, Journal of Fluids Engineering, Vol. 128 / pp. 671-679, (2006).

[7] Hammad K. J., Otugen M. V., Arik E. B., A PIV study of the laminar axisymmetric sudden expansion, Flow Experiments in Fluids 26, pp. 266-272, (1999).

[8] Chiang T. P., Tony W. H. Sheu, Robert R. Hwang, Sau A., Spanwise bifurcation in plane symmetric sudden expansion flows, Physical Review E,vol. 65, 016306, pp. 1-16, (2001).

[9] Nie J. H., Armaly B. F., Three-Dimensional Forced Convection in Plane Symmetric Sudden Expansion, Journal of Heat Transfer, Vol. 126 / pp. 836- 839, (2004).

[10] Wahba E.M., Iterative solvers and inflow boundary conditions for plane sudden expansion flows, Applied Mathematical Modeling 31, pp. 2553–2563, (2007).

[11] Thompson J. F., Thomas F., Mstia C. W., Automatic numerical generation of body fitted curvilinear coordinate system for field containing any number of arbitrary two dimensional bodies, J. Computational Physics, vol.15, pp. 299-319, (1974).

[12] Nagotov, E. F., "Application of numerical heat transfer" MCGraw Hill, (1978).

[13] Georgios C. Georgtou, William W. Schultz, Lorraine G. Olson, Singular finite elements for the problems sudden-expansion and the die-swell, International journal for numerical methods in fluids, Vol. 10, pp. 357-372 (1990).

Durability of Concrete Incorporating Corrosion Inhibitors Exposed to a Salt Solution of $CL^{-}+SO_4^{-2}$

Hayder Majeed Oleiwi
Civil Engineering Department
College of Engineering
University of Thi Qar
haider_alomary@yahoo.com

Abstract:

Laboratory investigations were performed in order to assess the effectiveness of three types of inhibitors, calcium nitrite , ethanolamine and Sika ferro gard 901(commercial inhibitor) with 1%, 2% and 3% concentration by weight of cement for each inhibitor to retarding corrosion of steel embedded in concrete. Concrete specimens were used to assess the effects of corrosion inhibitors on the compressive and tensile strength of concrete and corrosion of reinforcement.

Some of the specimens were subjected to wetting and drying cycles and reinforcement corrosion was evaluated by measuring corrosion potentials and corrosion current density. Other concrete specimens were immersed in the salt ($Cl^{-}+So_3^{-2}$) solution and reinforcement corrosion was accelerated by impressing an anodic potential of +12 V from a DC power supply and measuring the time-to-cracking of the concrete specimens. The results indicated that the concrete specimens incorporated corrosion inhibitors of calcium nitrite and Sika ferro gard 901 did not adversely affect the compressive and tensile strength of concrete. Furthermore, the time-to-cracking in specimens contains those two inhibitors (calcium nitrite and Sika ferro gard 901) were higher. Two percent of calcium nitrite followed by three percent of Sika ferro gard 901 were efficient in delaying the initiation of reinforcement corrosion and reducing the rate of reinforcement corrosion current density in the concrete specimens, while all the percentages of ethanolamine corrosion inhibitor were ineffective to delay corrosion of the rebar under the conditions of the study and it's adversely affect the strength.

Keywords: concrete, strength, corrosion inhibitors, corrosion potential, current density

ديمومة الخرسانة المخلوطة بمثبطات التآكل والمعرضة إلى محلول ملحي من الكلوريدات والكبريتات

المستخلص:

فحوصات مختبريه أنجزت لتقييم فعالية ثلاثة أنواع من المثبطات (نتريت الكالسيوم و ايثانول امين و سيكا فيرو كارد 901 (مثبط تجاري)) بنسب ١%و٢%و٣% من وزن السمنت لكل مثبط لتأخير التآكل في الحديد المطمور في الخرسانة. تم استخدام نماذج خرسانية لتقييم تأثير مثبطات التآكل على مقاومة الانضغاط ومقاومة الشد وتأكل حديد التسليح.

تم تعريض بعض النماذج إلى دورات من الترطيب والتجفيف لغرض تقييم التآكل في حديد التسليح من خلال قياس فرق جهد التآكل وقياس كثافة تيار التآكل (بطريقة فقدان الوزن). نماذج اخرى غمرت في المحلول الملحي الحاوي على أملاح الكلوريدات والكبريتات وتم تسريع التآكل في حديد التسليح عن طريق تسليط فرق جهد أنودي بمقدار ١٢ فولت وحساب وقت ظهور التشققات في النماذج الخرسانية. أشارت النتائج إلى أن النماذج الخرسانية الحاوية على مثبطات التآكل نتريت الكالسيوم وسيكا فيروكارد ٩٠١ لم توثر سلبا على مقاومة الانضغاط ومقاومة الشد. بالاضافة الى ذلك ، فان وقت ظهور التشققات في النماذج الحاوية على هذين المثبطين (نتريت الكالسيوم و سيكا فيروكارد ٩٠١) كان أعلى . استخدام ٢% من نتريت الكالسيوم و٣% من سيكا فيروكارد ٩٠١ كان الأكثر فعالية في تأخير بدء التآكل وكذلك في تقليل كثافة تيار التآكل لحديد التسليح في النماذج الخرسانية، بينما كانت جميع النسب المستخدمة للمثبط ايثانول امين غير فعالة في تأخير التآكل تحت ظروف الدراسة و له تأثير ضار على المقاومة.

1. Introduction

Corrosion of steel in concrete is one of the major causes of premature deterioration of reinforced concrete structures, leading to structural failure and the useful service-life of the structures is drastically reduced because of this phenomenon[1]. When these structures are exposed to aggressive substance containing chloride, the corrosion faults are frequently induced by the presence of chloride ions, these ions cause localized breakdown of the passive film that is initially formed on the steel due to the high pH of the concrete interstitial electrolyte. Once corrosion has initiated accumulation of corrosion products occurs on the steel surface. Since these products occupy a volume several times larger than that of the original steel[2], thus, the result is, an increase of the internal tensile stresses that generally induce cracking and spalling of the concrete cover. This situation facilitates further intrusion of aggressive agents and consequent acceleration of the corrosion process.

There are several sources of chlorides, chlorides incorporated in the concrete when it is mixed (e.g. from salty aggregated and salty mixing water) and chlorides penetrating in to concrete from the environment (e.g. from sea water, salty ground water and sea spray)[3] .

To minimize the corrosion processes a number of procedures can be assessed such as coating of concrete surface, surface treatment of the rebars, cathodic protection, chloride extraction and use of corrosion inhibitors.

ACI 116R-85 define a corrosion inhibitors as a chemical compound, either liquid or powder, can be mixed within the fresh concrete as an admixtures, usually in very small concentrations in order to reduce the risk of steel corrosion in reinforced concrete[4].

The corrosion inhibiting admixtures should not be as an alternative to the design specifications for durable concrete but to increased protection against corrosion [5]. Corrosion inhibitors can be divided into three types: anodic (e.g. Calcium nitrite, Sodium nitrite, Sodium benzoate, Sodium chromate), cathodic (e.g. sodium hydroxide, sodium carbonate, Phosphates, silicate and polyphosphates), and mixed (e.g. amine and aminoalcohol), depending on whether they interfere with the corrosion reaction preferentially at the anodic or cathodic sites or whether both are involved[6].

Several studies have been accomplished to evaluate the effectiveness of chemical admixtures in inhibiting reinforcement corrosion[7–9]. Early studies were concentrated on sodium nitrite, potassium chromate, sodium benzoate, and stannous chloride. Later work concentrated mainly on calcium nitrate. Craig and Wood[7], studied sodium nitrite, potassium chromate, and sodium benzoate using the polarization technique and found that sodium nitrite was the most effective corrosion inhibitor, but it had harmful effects on concrete strength. Similar results were also reported by Treadaway and Russel[8] who found that sodium nitrite inhibited corrosion of steel bars in the presence of chlorides, whereas sodium benzoate did not. Rosenberg et al.[10], studied the effect of calcium nitrite as an inhibitor in reinforced concrete. They used polarization techniques for evaluation of the inhibitors and reported that the relative corrosion rates for samples soaked in saturated sodium chloride solution for 90 days with 2% and 4% admixed calcium nitrite were about a factor of 15 times lower than those without the calcium nitrite admixture.

Tomazawa et al.[11], also supported effectiveness of calcium nitrite as a corrosion inhibitor in concrete. In accelerated tests with wetting and drying cycles at 80°C, calcium nitrite was found to be an effective inhibitor for long-term exposures even in marine environment.

Collins et al.[12], evaluated several inhibitors including (1) a calcium-nitrite-based inhibitor, (2) a monofluorophosphate-based inhibitor, (3) sodium tetraborate, (4) zinc borate (5) a proprietary oxygenated hydrocarbon produced from an aliphatic hydrocarbon, (6) a proprietary blend of surfactants and amine salts (MCI2020 which migrate through concrete), and (7) a proprietary alkanolamine inhibitor (MCI 2000). The results of the study, which involved monitoring of corrosion, compressive strength and resistivity, showed that the calcium-nitrite-based inhibitor was the most promising to mitigate corrosion in a repaired structure after removal of chloride-contaminated old concrete. On the other hand, both borate compounds were found to retard the setting of Portland cement.

Prowell et al.[13], evaluated some of the inhibitors studied by Collins et al.[12] and conducted ponding experiments where they monitored corrosion by measuring half-cell potential, linear polarization resistance, and chloride ion concentration for a period of 325

days. They reported that two proprietary inhibitors Alox 902 and MCI 2020 were the best performers.

Berke and Hicks [14], published long-term data to show the levels of chloride that a given level of calcium nitrate can protect. They also indicated that once corrosion initiates, the rates are lower with the addition of calcium nitrate.

Jamil et al.[15], conducted electrochemical impedance measurements in order to obtain information on the corrosion behavior of reinforcing steel in the presence of a penetrating amino-alcohol corrosion inhibitor. The investigation was performed in solutions contaminated with chlorides, in the presence of the inhibitor. The electrochemical results indicated that the inhibitor is able to penetrate through mortar, minimizing steel corrosion.

The significance of using corrosion inhibitors in aggressive exposures is ascribable to the fact that data are lacking on the performance of reinforced concrete that is subject to both chloride and sulfate salts.

This investigation was conducted to evaluate the effectiveness of three different types of corrosion inhibitors in reducing reinforcement corrosion in concrete subjected to chloride and sulfate salts with percentage equivalent to these present in soil and underground water in southern parts of Iraq. The performance of the selected inhibitors in reducing reinforcement corrosion was evaluated by adopting various techniques.

2. Experimental Works

2-1: Materials and Mixes

Sulfate resistance cement (Type V) was used, the chemical composition and physical characteristics are given in tables 1 and 2, which indicate compliance with the requirements of Standard Iraqi Specification 5/1984[16].

Table 1: Chemical composition of cement*

Chemical components	CaO	Sio_2	Al_2O_3	Fe_2O_3	**Lime Saturated Factor**	MgO	SO_3	L.O.I	**Insoluble residues**	C_3A
Content for tested cement,%	62	24	4	5	0.75	4.8	1.78	2.7	0.92	2.15
Limit of Iraqi specification No.5/1984, %	-	-	-	-	0.66-1.02	≤ 5	≤ 2.5	≤ 4	≤ 4	≤ 3.5

Table 2: Physical characteristics of cement*

Physical properties	Test results	Limit of Iraqi specification No. 5/1984, %
Setting time, min.		
-Initial setting	121	≥ 45
-Final setting	200	≤ 600
Compressive strength, MPa		
3 days	19	≥ 15
7 days	23.5	≥ 23

*: This test was done by construction laboratory at College of Engineering- University of Thi Qar.

Natural sand of 4.75 mm maximum size complying with the Standard Iraqi Specification 45/1984[17] has been used. The sieve analysis is given in table 3. The coarse aggregate is crushed gravel with maximum size of 20 mm has been used and its comply with Iraqi specification 45/1984, table 4. Tap water was used for mixing and curing operations. Steel deformed bars, φ 12 mm, conforming to ASTM-A615/A 615-06[18] specifications were used. The mechanical properties of steel are shown in table 5.

Table 3 :Grading of sand

Sieve size, mm	10	4.75	2.36	1.18	0.6	0.3	0.15
Percentage passing	100	99	90	75	52	15	2
Limits of Iraqi Specification No. 45/1984 (Zone 2)	100	90-100	75-100	55-90	35-59	8-30	0-10

Table 4: Grading of gravel

Sieve size, mm	37.5	20	10	4.75
Percentage passing	100	99	57	2
Limits of Iraqi Specification No. 45/1984 (5-20)mm	100	95-100	30-60	0-10

Table 5: Mechanical properties of steel bars*

Test results for steel bars		ASTM-A615/A 615-06 requirements
Nominal diameter, mm	12	-
Yield strength, MPa	566	≥ 420
Tensile strength, MPa	637	≥ 620
Elongation,%	10	Min. 9

*: This test was done by construction laboratory at College of Engineering- University of Thi Qar.

The mix proportion by weight of cement, fine and coarse aggregate were (1:1.72:2.8). The ingredient proportions are kept constant throughout the work. The cement content was 390 kg, w/c ratio was 0.52 for all concrete specimens.

Three types of inhibitors were used in this work (calcium nitrite(inorganic compound), ethanolamine(organic compound) and sika ferro gard 901(combination of organic and inorganic inhibitors)) with percentage of 1%, 2% and 3% by weight of cement for each inhibitor.

2-2: Preparation of The Salt Solution ($Cl^- + So_4^{-2}$)

The salts used in preparing the solution were pure NaCl, $CaCl_2.2H_2O$ and $MgSo_4.7H_2O$ with concentration of 4.5%, 0.55% and 1.79%, respectively to give concentration of Cl^- equal to 30000 ppm and So_4^{-2} equal to 7000 ppm to simulate sulfate and chloride salts in soil and underground water in southern parts of Iraq according to the report of National Center for Geological Survey [19]. Potable water was used as a solvent for these salts.

2-3: Specimens Details

100 mm x 100 mm x 100 mm concrete cubes were prepared for compression strength, concrete cylinders 150 mm diameter and 300 mm high were casted for tensile strength and reinforced concrete specimens of 100 x 100 x 100 mm with a centrally placed 12 mm diameter reinforcing steel bar of 50 mm long were casted for electrochemical measurements (corrosion assessment). Copper wire is connected to the steel rebar embedded in concrete for electrical connections . The specimens were cast with and without inhibitors ranging from 1% to 3% by weight of cement. Three specimens for each percentage of the corrosion inhibitors were tested, the specimens were covered with nylon sheet to minimize evaporation during 24 hrs after casting. Thereafter, the specimens were removed from the mould and cured in potable water for 27 days.

3. Techniques Used

3-1: Compressive Strength

After curing (24 hr. in air and 27 days in potable water) the specimens of compressive strength were tested according to BS 1881: Part 116: 1983[20].

3-2: Tensile Strength

ASTM C496-96[21] was adopted to test the concrete specimens for tensile strength after curing.

3-3: Half-Cell Potential (Corrosion Potential)

In normal conditions, the evolution of salts ingress is slow and has an evolution rate measured in years. In order to accelerate this process. After 28 days of curing, the specimens were exposed to sulfate and chloride solution using the wetting and drying cycles, consisting of 8 days immersion in the solution followed by 7 days drying period in open atmosphere. The corrosion potentials were measured according to ASTM C876[22]. Corrosion potentials were measured using a copper– copper sulfate reference electrode (CSE) and a high impedance voltmeter. The positive terminal of the voltmeter was connected to the working electrode (rebar) and the common terminal was connected to the reference electrode (CSE) . The cycle in continued for 120 days. From the results, potential with time plot is drawn using the average potentials obtained. According to ASTM C 876 potential values more negative than -350 mV CSE indicate more than 90% probability of corrosion activation. Figure (1) illustrate the test method.

3-4: Accelerated Corrosion

In this technique[23] the reinforced concrete specimens, after 28 days of curing, is placed in the salt ($Cl^- + So_4^{-2}$) solution and accelerate the corrosion of steel embedded in concrete by impressing a +12 V fixed anodic potential from a DC power supply until cracking of the specimens. The steel bar in the concrete specimens were connected to the positive terminal of a DC power supply to be anode. 100 x 100 mm stainless steel plate was placed in the solution tank and connected to the negative terminal of a DC power supply to be cathode.

For each specimen, the time taken for initial crack was recorded. Figure (2) illustrate the electrical connection. Battery, charger power 12V and AC conductor were used to overcome main electrical power outage.

Figure1: corrosion potential measurement

Figure 2: Electrical connection for applying a +12 V fixed anodic potential to accelerate the corrosion

3-5 : Corrosion current density by weight loss method [24]

For the determination of corrosion rate by (weight loss) measurement, the initial weight of the rebar samples was taken in 4-digit electronic balance. After the curing period was over, all the specimens were completely immersed in chloride and sulfate solution for 8 days and then subjected to drying for another 7 days in open air at room temperature (wetting and drying cycles). All the concrete specimens were subjected to eight complete cycles.

After testing, the concrete specimens were broken and the reinforcing steel bars were removed. The procedure stated in ASTM G1-03[25] was adopted for the cleaning of corroded steel bars and for the determination of mass loss. The corrosion rate was calculated using the following equation given in ASTMG1-03[25].

$$\text{Corrosion rate (mm/year)} = \frac{(K \times W)}{(A \times T \times D)}$$

Where:

K: a constant equal to 8.76×10^4

W: mass loss in grams

A: actual corroded area of steel bar in cm^2 after removal from specimen and visually examining

T: time of exposure in hours

D: density of steel (7.85 g/cm^3).

Using Faraday's law, the corrosion rate in (mm/year) obtained from mass loss measurement was converted to corrosion current density ($\mu A/cm^2$) by assuming uniform corrosion occurred over the steel surface by the following equation [24].

$$\text{Corrosion rate(mm/year)} = \frac{(0.00327 \times a \times Icorr.)}{(n \times D)}$$

Where:

Icorr.: corrosion current density in $\mu A/cm^2$

a: atomic weight of iron(55.84 amu)

n: no. of electrons exchanged in corrosion reaction(2 for iron)

D = density of steel (7.85 g/cm^3).

4. Results and Discussion

4-1: Compressive Strength

Figure(3) shows the average compressive strength of the control concrete specimens (0% corrosion inhibitor) and those containing the corrosion inhibitors after 28 days of curing. The experimentally obtained results showing the value of compressive strength of the specimens incorporating ethanolamine corrosion inhibitors was less than of the control specimens and the decrease was about 3.5-13.8% depending on percentage of inhibitor, the maximum reduction was about 13.8% when 3% of this corrosion inhibitor was added and that is may be due to retarding effect of the inhibitor and the air content might be slightly increased. This reduction was also confirmed during another research project [26].

From Figure (3) it is indicated that there is slightly increased in compressive strength when percentage of Sika ferro gard 901 corrosion inhibitor increased and that is indicate there is no adverse effect on the compressive strength of concrete.

The strength for concrete containing 2% of calcium nitrite corrosion inhibitor was about 10% higher than for control specimens. In 3% calcium nitrite there was reduction in the rate of increasing. K.Y. Ann et al.[27], indicates that an increase in dosage of corrosion inhibitor may not guarantee the properties of concrete. The cause of the reduction in compressive strength is not well known.

4-2: Splitting Tensile Strength

Figure (4) shows the splitting tensile strength with percentage of inhibitor addition and it's illustrate the same behavior for compressive strength with slightly different in reduction or increasing in value of tensile strength. With 1% inhibitor addition, there was no adverse effect for tensile strength except ethanolamine inhibitor there was a slightly reduction than the control concrete. With 2% of calcium nitrite inhibitor addition, the tensile strength was about 5% higher than the control concrete. With 3% inhibitor addition, the figure illustrate that, as the percentage of calcium nitrite and ethanolamine inhibitor level increases, the split tensile strength decreases but there is slightly increase with Sika ferro gard 901 inhibitor.

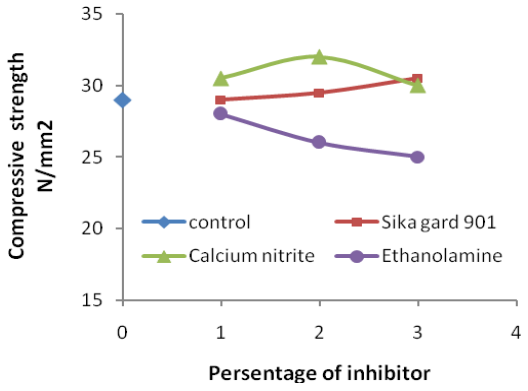

Figure 3: Compressive strength at 28 days of concrete specimens incorporating corrosion inhibitors

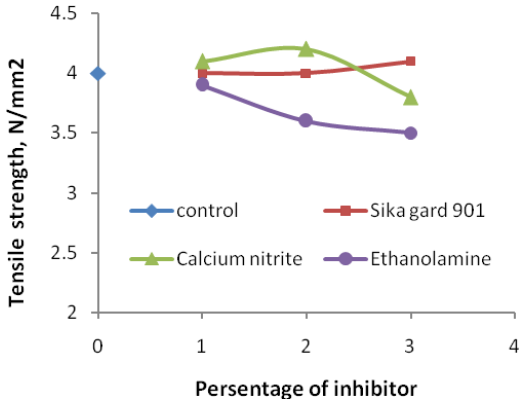

Figure 4: Splitting tensile strength at 28 days of concrete specimens incorporating corrosion inhibitors

4-3: Half-Cell Potential (Corrosion Potential)

The corrosion potentials on steel in the concrete specimens incorporating with 1% of the selected corrosion inhibitors are showed in Figure (5). From the figure it is observed that the corrosion potentials on steel in the all concrete specimens were more negative than – 350 mV CSE after about 30 days of exposure indicating the corrosion activation of the rebar based on the ASTM C 876 criteria.

Figure (6) shows the corrosion potential corrosion with time for 2% inhibitor added concrete in the solution under alternate wetting and drying conditions and it is illustrate that concrete specimens containing calcium nitrite was less negative -350 mV CSE indicating the passivity of reinforcing steel even after 120 days of test period and it was -274 mV CSE. Concrete specimens incorporating Sika ferro gard 901 was showing a more negative potential than -350 mV CSE after 60 days of exposure. Control specimens and that incorporating

ethanolamine inhibitor were more negative -350 mV CSE after 30 day of exposure and it were -552 and -605 mV CSE respectively after 120 days of exposure indicating the corrosion activation.

Figure (7) shows the corrosion potential with time for 3% inhibitor added concrete in the salt solution under alternate wetting and drying conditions. In 3% inhibitor added , the control concrete specimens and incorporating with calcium nitrite and ethanolamine are showing a more negative potential than -350 mV CSE after 30 days of exposure indicating the active condition of the rebar while concrete specimens with Sika ferro gard was less negative -350 mV CSE along of period of exposure. The corrosion potentials on steel in the control, Sika ferro gard 901, calcium nitrite and ethanolamine concrete specimens were -552, -316, -410 and -626 mV CSE respectively after 120 days of exposure. Comparing with control specimens, the potentials in the concrete specimens incorporating sika gard 901 and calcium nitrite were less negative (more positive) than the control concrete specimens.

Figures (6) and (7) can be showed the potentials in the concrete specimens incorporating 3% calcium nitrite were unexpectedly more negative than those incorporating 2% calcium nitrite under the conditions of this study, it were after 120 days of exposure -274 and -410 mV CSE for 2% and 3% calcium nitrite respectively. The same result was obtained by Al-Amoudi et al.[22] when they were used concrete specimens prepared with seawater and incorporating calcium nitrite with 2% and 4%.

Figures (5-7) show that corrosion potential of ethanolamine inhibitor was decreasing and it's more negative than control when increased the percentage of inhibiter, it was after 120 day of exposure conditions -573, -605 and -626 mV CSE with 1%, 2% and 3% of ethanolamine inhibitor respectively, that is means this inhibitor ineffective to delay corrosion of the rebar under the conditions of the study.

4-4: Accelerated Corrosion

The time to cracking of control concrete specimens and those incorporating with corrosion inhibitors are shown in figure 8. From this figure it can be observed that the time to cracking is maximum in the Specimens incorporating calcium nitrite and Sika gard 901 corrosion inhibitors addition, it were ranged (90-98) hours, indicating the lower permeability of the concrete when compared to control and ethanolamine specimens. There was no clear effect to the percentage of inhibitor.

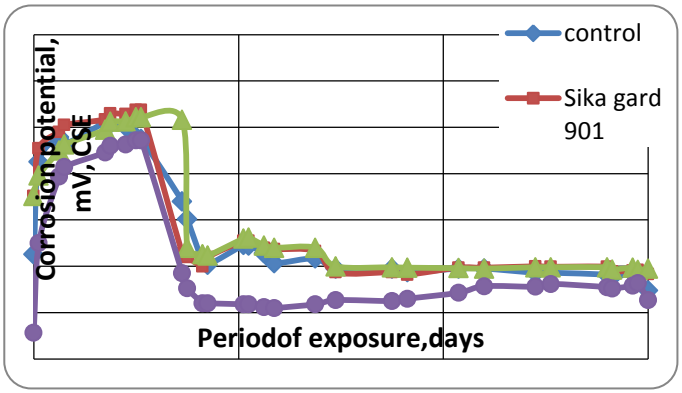

Figure 5: Corrosion potential on steel in the concrete specimens incorporating with 1% inhibitor

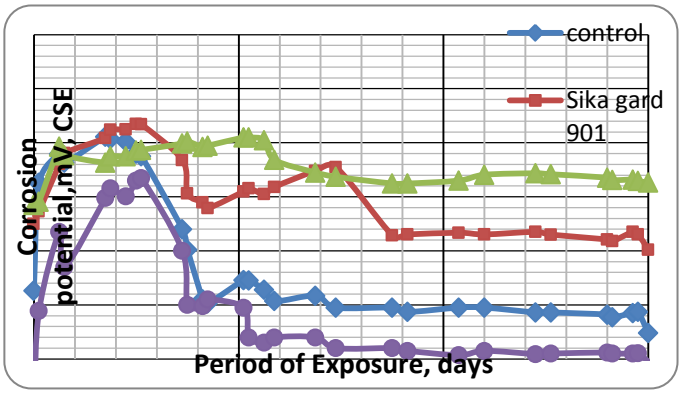

Figure 6: Corrosion potential on steel in the concrete specimens incorporating with 2% inhibitor

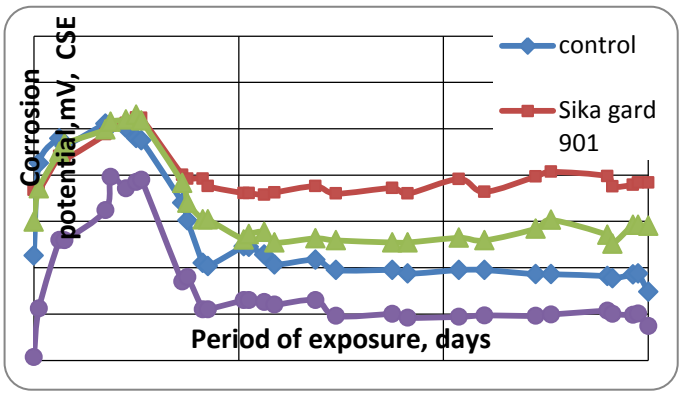

Figure 7: Corrosion potential on steel in the concrete specimens incorporating with 3% inhibitor

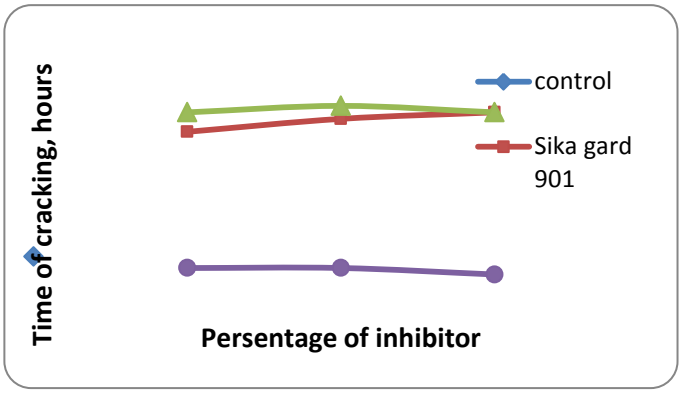

Figure 8: Time of cracking for concrete specimens incorporating inhibitors

4-5: corrosion Current Density by Weight Loss Method

The average corrosion current density calculated in $\mu A/cm^2$ for rebar embedded in concrete after 120 days of exposure in the solution with different type and percentage of added inhibitors from 1% to 3% by weight of cement are shown in figure (9).

Figure 9 shows the corrosion current density (Icorr) values in the concrete specimens with 1% corrosion inhibitors were in the range of (0.714–0.886) $\mu A/cm^2$ while in the concrete specimens with 2% corrosion inhibitors were in the range of (0.602–0.963) $\mu A/cm^2$. The Icorr values in the concrete specimens with 3% corrosion inhibitors were in the range of (0.696–0.963) $\mu A/cm^2$ and 0.911 $\mu A/cm^2$ for control. The effective corrosion inhibitors were calcium nitrite and Sika ferro gard 901 in the study conditions, the minimum Icorr values were noted in the concrete specimens with 2% calcium nitrite inhibitor , followed by those incorporated with 3% Sika gard 901 inhibitor, The decrease in the Icorr was 33.9% and 23.6% respectively comparing with control specimens.

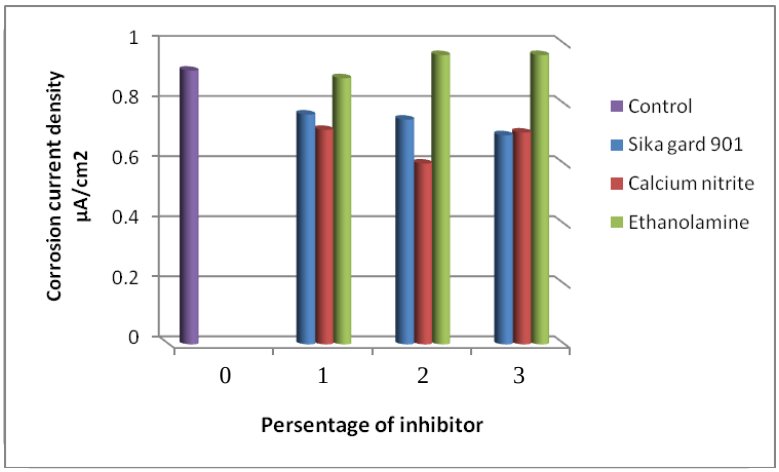

Figure 9: Corrosion current density for concrete specimens incorporating inhibitors

5- Conclusions

1. There is no adverse effect on the compressive and tensile strength of concrete specimens incorporating calcium nitrite and Sika ferro gard 901 corrosion inhibitors. The results showing maximum increasing were about 10% and 5% in the compression and tensile strength respectively when 2% of calcium nitrite inhibitor was used comparing with the control specimens and there was a slightly increasing with specimens containing Sika ferro gard 901.
2. Corrosion potential studies revealed that the best performance was shown by 2% of calcium nitrite corrosion inhibitor followed by 3% of Sika ferro gard 901 corrosion inhibitor, the corrosion potentials were -274 and -316 mV CSE, respectively, and they were less negative (more positive) than -350 mV CSE indicating the passivity of reinforcing steel.
3. Ethanolamine corrosion inhibitor ineffective to delay corrosion of the rebar under the conditions of the study and there was adverse effect on the compressive and tensile strength.
4. Calcium nitrite and Sika ferro gard 901corrosion inhibitors increased the time to cracking of concrete specimens to about 90% higher comparing with control specimens.
5. The minimum corrosion current density values were obtained in the concrete specimens with 2% calcium nitrite inhibitor, followed by those incorporated with 3% Sika ferro gard 901 inhibitor, the percentage reduction in the values of corrosion current density was 33.4% and 23.6% than that in the control specimens, respectively.

References

1. Saricimen H., 1993,"Concrete durability problems in the Arabian Gulf region", a review. In: Proceedings of 4th International Conference on Deterioration and Repair of Reinforced Concrete in the Arabian Gulf, Manama, Bahrain, p. 943–959.
2. Tuutti K., 1982, "Corrosion of Steel in Concrete", Swedish Cement and Concrete Research Institute, Stockholm, Sweden,.
3. Poulsen E., 1994, "chloride profiles", Analysis and interpretation of observation, AEC laboratory, Denmark, P. 47-62.
4. Page C., Treadaway K., Bamforth P. , 1990, " Corrosion of reinforcement in concrete", London, Elsevier Applied Science, p. 825–850.
5. Nathan C., 1973, " Corrosion inhibitors", National Association of Corrosion Engineers, p. 279.
6. Soylev T.A., Richardson M.G., 2008," Corrosion inhibitors for steel in concrete: State-of-the-art report", Construction and Building Materials 22(4), p. 609–622
7. Craig R.J., Wood L.E., 1970,"Effectiveness of corrosion inhibitors and their influence on the physical properties of portland cement corrosion inhibitor in concrete", Transportation Research Record no 328, p. 77.
8. Treadaway K.W.J., Russell A.D., 1968, "The inhibition of the corrosion of steel in concrete", Highways Public Works 36(19), P.40.

9. Slater J.E., 1983, "Corrosion of metals in association with concrete", ASTM Special Publication No. 818, p.53.
10. Rosenberg A.M., Gaidis J.M., Kossivas T.G., Previte R.W., 1977, "A corrosion inhibitor formulated with calcium nitrite for use in reinforced concrete", ASTM STP629, p. 89–99 .
11. Tomazawa F., Masuda Y., Tanaka H., Fukushi I., Takakura M.,Hori T., Higashi S., 1987, "An experimental study on effectiveness of corrosion inhibitor in reinforced concrete under high chloride content conditions", Nihon Architecture Society.
12. Collins W.D., Weyers R.E., Al-Qadi I.L., 1993, " Chemical treatment of corroding steel reinforcement after removal of chloride-contaminated concrete", Corrosion 49(1), P. 74.
13. Prowell B.D., Weyers R.E., Al-Qadi I.L., 1993,"Evaluation of corrosion inhibitors for the rehabilitation of reinforced concrete structures", Research sponsored by Strategic Highway Research Program and carried out at Virginia Polytechnic Institute and State University, Blacksburg, VA, the paper was provided by the manufacturer of MCI2000.
14. Berke N.S., Hicks M.C., 2004," Predicting long-term durability of steel reinforced concrete with calcium nitrate corrosion inhibitor", Cement and Concrete Composites 26(3), p.191–198.
15. Jamil H.E., Shriri A., Boulif R., Montemor M.F., Ferreira M.G.S., 2005," Corrosion behavior of reinforcing steel exposed to an aminoalcohol based corrosion inhibitor", Cement and Concrete Composites 27(6), p.671–678.

١٦. المواصفة القياسية العراقية رقم ٥ ،١٩٨٤، "السمنت البورتلاندي"، الجهاز المركزي للتقييس والسيطرة النوعية.

١٧. المواصفة القياسية العراقية رقم ٤٥ ،١٩٨٤، "ركام المصادر الطبيعية المستعمل في الخرسانة والبناء"، الجهاز المركزي للتقييس والسيطرة النوعية.

18. ASTM Standard A 615/A 615M-06a,"Standard specification for deformed and plain carbon-steel bars for concrete reinforcement", American Society for Testing and Materials.
19. Alhadithy R.Y.M., 2003," Durability of high performance concrete incorporating high reactivity metakaolin and rice husk ash", MSc thesis, University of Technology, p.47.
20. British Standard BS 1881- part 116,1983, " Method for determination of compressive strength of concrete cubes", British Standards Institution.
21. ASTM Standard C 496- 96,"Standard test method for splitting tensile strength of cylindrical concrete specimens", American Society for Testing and Materials.
22. ASTM Standard C 876 – 91 (Reapproved 1999), "Standard test method for half-cell potentials of uncoated reinforcing steel in concrete", American Society for Testing and Materials.
23. Al-Mehthel M., Al-Dulaijan S., Al-Idi S.H., Shameem M., Ali M.R., Maslehuddin M., 2009, "Performance of generic and proprietary corrosion inhibitors in chloride-contaminated silica fume cement concrete" Construction and Building Materials 23(5), p.1768–1774

24. Pradhan B., Bhattacharjee B., 2009, "Performance evaluation of rebar in chloride contaminated concrete by corrosion rate", Construction and Building Materials 23(6), p.2346-2356.
25. ASTM Standard G1-03,"Standard practice for preparing, cleaning and evaluating corrosion test specimens ", American Society for Testing and Materials.
26. Schutter G.D., Luo L.,2004, "Effect of corrosion inhibiting admixtures on concrete properties", Construction and Building Materials 18 (7), p. 483–489.
27. Ann K.Y., Jung H.S., Kim H.S., Kim S.S., Moon H.Y., 2006, "Effect of calcium nitrite-based corrosion inhibitor in preventing corrosion of embedded steel in concrete", Cement and Concrete Research 36 (3),p. 530 – 535
28. Al-Amoudi O.S.B., Maslehuddin M., Lashari A.N., Almusallam A.A., 2003," Effectiveness of corrosion inhibitors in contaminated concrete", Cement and Concrete Composites 25 (4-5),p. 439–449.

Effect of Adding Horizontal Rings on the Thermal Behavior of Cylindrical Liquid Enclosure Exposed to High Heat Flux

Dr. Mohammed Hamed Mahmoud
Asst. Professor
Mech. Eng. Dept.
Al- Mustansiriyah University

Eng. Ali Jaber Alkhakani
Mech. Eng. Dept.
Al- Mustansiriyah University
Baghdad - Iraq

Abstract :

Power generation by using concentrated solar thermal energy on liquid enclosures is one of the most promising renewable energy technologies. In this work, a developed liquid enclosure fitted with various number and configurations of horizontal metal rings have been analyzed, fabricated and tested. The influence of adding metal rings arrangement is investigated for its potential to enhance radial heat conduction to the center-line of the enclosure from the side-walls. Experiments were carried out for fluid in both static and dynamic modes of operation inside the enclosure that subjected to high heat flux.

A developed two-dimensional CFD model to predict the transient flow and thermal fields within liquid enclosure subjected to heat flux has been developed and tested. The developed numerical model takes into consideration energy transport between the liquid inside enclosure and the solid material of the enclosure. The numerical simulations have been compared with experimental measurement. The computational code has been found in a good level of agreement with the experimental data except for liquid at the peak part of the enclosure.

The results indicate that adding metal rings produce significant impact on the transient temperature difference inside enclosure during both static and dynamic modes. The six-ring model is found to be more effective for enhancing radial heat transfer than other three models that have been tested. The in-line arrangement is found to provide better thermal effect as compared to the staggered rings.

Two new correlations for natural heat transfer inside liquid enclosures subjected to high heat flux have been formulated (one for no-ring model and the other for six-ring model). The natural Nusselt number is found to be around a constant value for Rayleigh number less than (5×10^8).

The recommended use of metal rings inside liquid enclosures subjected to heat flux, and the predicted Nusselt number correlation, will add to local knowledge a significant mean to gain more heat in large scale concentrated solar power plants.

Keywords : *horizontal rings, liquid enclosure, concentrated solar energy, Nusselt number.*

Introduction:

The heating and cooling processes within liquid cylindrical enclosures often occurs in many engineering applications and industrial processes, such as, industrial food production, domestic solar water heaters, petroleum exploration and metallurgic industry, among others [1] . Another application is related to chilled-water storage unit in air-conditioning systems. This chilled storage is charged at night during hours of maximum coefficient of performance, and discharged at the next day (or in the hours of electricity cutoff) to meet the load demand [2]. Generally, these processes involve a heat transfer of a fluid that has initially a uniform temperature. The design of such systems, demands an understanding of the transient temperature fields that arises in liquid enclosure during charging/discharging and relaxation periods (i.e. in the absence of external flow).

In the recent few years a significant effort has been invested into the determination of the flow profiles and heat flow distribution within the Concentrated Solar Thermal (CST) systems. (CST) is a method where by the solar radiation that falls on a given surface is focused on a smaller surface to increase its intensity. (CST) is a proven renewable energy technology that harnesses solar irradiation in its most primitive form for electricity generation and industrial applications [3]. In many ways, the design and operation of solar thermal power generation systems is more complex and challenging than that of conventional fossil fuel power–plants. Therefore, technologies are required to concentrate, absorb and transfer solar thermal energy to the working fluid [4].

Several works concerning about this field are available in the literature, involving experimental and numerical analysis. Experimental investigations by Shyu et al. [5] showed that degradation of thermocline in storage tank with thicker walls is more pronounced due to larger axial heat conduction in the tank wall. It was concluded that the heat loss to the ambient was the major factor in degradation of the thermal stratification in an un-insulated tank.

Hariharan and Badrinarayana [6] studied the effect of ambient and operating conditions on temperature distribution of hot water storages. They observed that temperature gradient improves with increasing temperature difference and water flow rate.

Zachar et al. [7] studied numerically the impact of a baffle plate facing the inlet jet on temperature fields in vertical tanks. According to their study, the use of large baffle plates allows the preservation of the thermal gradient even for high flow rates.

Altuntop et al. [8] analyzed numerically the effect of using different obstacles on thermal behavior in hot water tanks. The results indicate that the obstacle types having gap in center appear to have better thermal gradient than those having gap near the tank wall. However, the numerical model ignored the effect of tank wall in the calculations. Also, no experimental work has been conducted to validate these numerical results.

Haltiwanger and Davidson [9] investigated experimentally the effect of adding cylindrical baffle in a cylindrical water thermal storage. The results indicate that the baffle increases the storage side convective heat transfer.

Ham et al. [10] concluded that two-dimensional models can take the mixing between layers into account, which includes more factors than that of one-dimensional level. They

concluded that further research should be focus on enhancement of temperature gradient between layers.

A comprehensive examination of literature in the field indicates that there are a significant number of studies related to the problem of the thermal water enclosure. However, the majority of these works have ignored the thermal effect of the solid enclosure materials. Also, most of these previous works consider either the enclosure is adiabatic, or the direction of heat flow is out of the enclosure. Also, it seems that most of previous researches have been focused on thermal response for solar domestic hot storage tanks and very little work has been done on thermal gradient evaluations for liquid energy storage packed with solid materials. In fact, just recently Valmili et al. [12] concluded that there are no insufficient experimental data related to heat transfer and energy transport inside liquid enclosures that packed with solid materials.

However, the authors of this paper did not find in the literature any work related to thermal response of liquid enclosure packed with metal material and subjected to heat flux at the same time.

On the other hand, and as far as known, laboratory measurements of natural heat transfer coefficient in conventional liquid enclosures that subjected to heat flux are very limited in open literatures. Actually, it has been noted that there are only a few simple correlations for limited boundary conditions [13-20]. Further, unlike the conventional liquid enclosures, there is a lake for heat transfer correlations that related to liquid enclosures fitted with solid materials and subjected to heat flux at the same time. However, these seem to be proprietary data.

Keeping the above in view, the main objectives of the present research are to:

1- Provide knowledge of the thermal effects of adding several new metal rings inside liquid enclosure that subjected to high heat flux. The rings should be suitable to incorporate into existing liquid enclosures. Also, these metal rings should be in good thermal contact with the inner enclosure wall to increase the enclosure ability to absorb and store more thermal energy from the walls.
2- Develop a two-dimensional numerical model based upon the conservation equations of mass, momentum and energy to represent the transient flow and thermal fields within the liquid enclosure during both static (with no liquid flow) and dynamic (with liquid flow) modes of operation. The developed model should take in consideration the thermal interaction between the liquid and the solid materials of the enclosure.
3- Test and validate the developed numerical model against a directly measured experimental data of a laboratory scale liquid enclosure that is made locally for this purpose. The enclosure should be exposed to heat flux and packed with several metal rings.
4- Formulate suitable correlations for heat transfer coefficient inside liquid enclosure that subjected to high heat flux and fitted with new arrangement of horizontal rings (at the same time).

Numerical Model :

The numerical model proposed in this work consists of cylindrical vertical tank as shown in Figure (1) whose geometrical aspect ratio is (H/2R), and is subjected to heat flux. The governing equations in the enclosure are the mass continuity equation, the momentum equations in the axial and radial directions, the energy equation of the liquid and an additional energy equation for the solid material of the enclosure. Assuming the working fluid is incompressible, Newtonian and two-dimensional, the transient conservation equations can be written as:

$$\frac{\partial \rho}{\partial t} + \frac{\partial}{\partial x}(\rho . u) + \frac{1}{r}\frac{\partial}{\partial r}(\rho . v . r) = 0 \quad \ldots\ldots\ldots\ldots \quad (1)$$

$$\frac{\partial \rho}{\partial t}(\rho_L . u) + \frac{\partial}{\partial x}(\rho_L . u^2) + \frac{1}{r}\frac{\partial}{\partial r}(\rho_L . r . u . v) = -\frac{\partial P}{\partial x} + \frac{\partial}{\partial x}\left(\mu \frac{\partial u}{\partial x}\right) + \frac{1}{r}\frac{\partial}{\partial r}\left(\mu . r . \frac{\partial u}{\partial r}\right) - \rho_L . g \quad \ldots\ldots\ldots\ldots \quad (2)$$

$$\frac{\partial}{\partial t}(\rho_L . v) + \frac{\partial}{\partial x}(\rho_L . u . v) + \frac{1}{r}\frac{\partial}{\partial r}(\rho_L . r . v^2) = -\frac{\partial P}{\partial r} + \frac{\partial}{\partial x}\left(\mu \frac{\partial v}{\partial x}\right) + \frac{1}{r}\frac{\partial}{\partial r}\left(\mu . r . \frac{\partial v}{\partial r}\right) - \mu . \frac{v}{r^2} \quad \ldots\ldots\ldots\ldots \quad (3)$$

$$\frac{\partial}{\partial t}(\rho_L . Cp_L . T) + \frac{\partial}{\partial x}(\rho_L . Cp_L . T . u) + \frac{1}{r}\frac{\partial}{\partial r}(\rho_L . Cp_L . T . v . r) = \frac{\partial}{\partial x}\left(K_L . \frac{\partial T}{\partial x}\right) + \frac{1}{r}\frac{\partial}{\partial r}\left(K_L . r . \frac{\partial T}{\partial r}\right) \quad \ldots\ldots\ldots\ldots \quad (4)$$

$$\frac{\partial}{\partial t}(\rho_S . Cp_S . \overline{T}) - \frac{\partial}{\partial x}\left(K_S . \frac{\partial T}{\partial x}\right) + \frac{1}{r}\frac{\partial}{\partial r}\left(K_S . r . \frac{\partial T}{\partial r}\right) \quad \ldots\ldots\ldots\ldots \quad (5)$$

Equation (5) is an additional energy equation in the present improved numerical model used to include the solid material effect at different enclosure heights.

For static mode (i. e. without liquid flow), the initial condition is null velocities in whole enclosure when the hot water in the upper part and the cold water in the lower part. The boundary conditions are no–slip condition at symmetry line, lateral wall and enclosure top and bottom. The heat gain to the liquid is through lateral walls and enclosure top. The bottom of the enclosure is considered perfectly insulated.

For dynamic mode simulations, the liquid is initially at a prescribed temperature profile with the entry of hot or cold liquid during charging or discharging processes. The boundary conditions are the same for the natural heating simulations, but considering null shear stress at the symmetry line.

The boundary conditions for the momentum and energy equations, at the inlet jet, were (u = u_{in}) ; (v = 0) and (T = Tin). At the outlet jet, boundary conditions were ($\partial u/\partial x$ = 0) ; v = 0 and ($\delta T/\delta x = o$). In simulations, the boundary condition symmetry is applied along the vertical line (r = o), therefore, the calculations domain was just half the physical body.

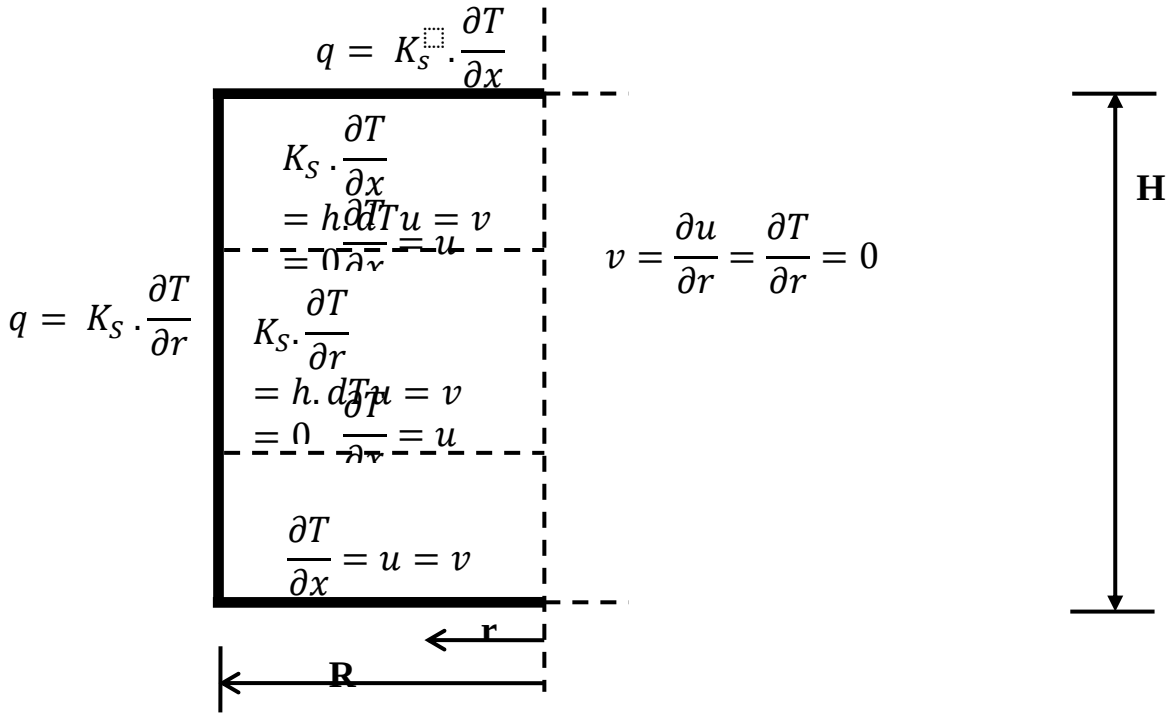

Figure (1): Boundary conditions of the mathematical model.

The above model requires solution of the conservation of the mass momentum and energy equations for the multiple zone enclosure the separated by multi-horizontal metal circular rings. The above transient equations are solved using the finite volume method in cylindrical structured mesh. To solve the algebraic linear equations resulting from the discretization of the governing equations, the Tri-Diagonal Matrix Algorithm (TDMA) was employed.

The solution of the transient problem was carried out in a completely implicit form. For each time step, the iterative process was applied until reaching the convergence criterion. Solutions are assumed to converge when the following convergence criterion is satisfied by every dependent variable at every grid point in the computational domain;

$$\left|\frac{\Phi_{new}-\Phi_{old}}{\Phi_{new}}\right| \leq \Phi$$

Where Φ in general could be any dependent variable. In this work, Φ is less than (10^{-3}) for continuity and momentum equations and Φ is less than (10^{-6}) for energy equations. The simulations run with a time step of (1-3) seconds.

In the formulation of the mathematical model, the physical properties of the water (ρ, μ, K) are considered uniform in space and updated in time as a function of water average temperature, ($T_{av.}$) in K.

Density, [kg/m^3]

$$\rho = 863 + 1.21 * T_{av.} - 0.00257 * T_{av.}^2$$

Dynamic viscosity, [kg/m.s]

$$\mu = 0.0007 * \left(\frac{T_{av.}}{315}\right)^{-5.5}$$

Thermal conductivity, [W/m.K]

$$K = 0.375 + 8.84 \times 10^{-4} * T_{av.}$$

Experimental Work:

In this work, thermal behavior of water enclosure subjected to high heat flux is investigated experimentally. The tests were preformed to obtain the temperature profile inside the enclosure during both static (stagnation) and dynamic (charging/discharging) modes of operation. Figure (2) shows the experimented apparatus.

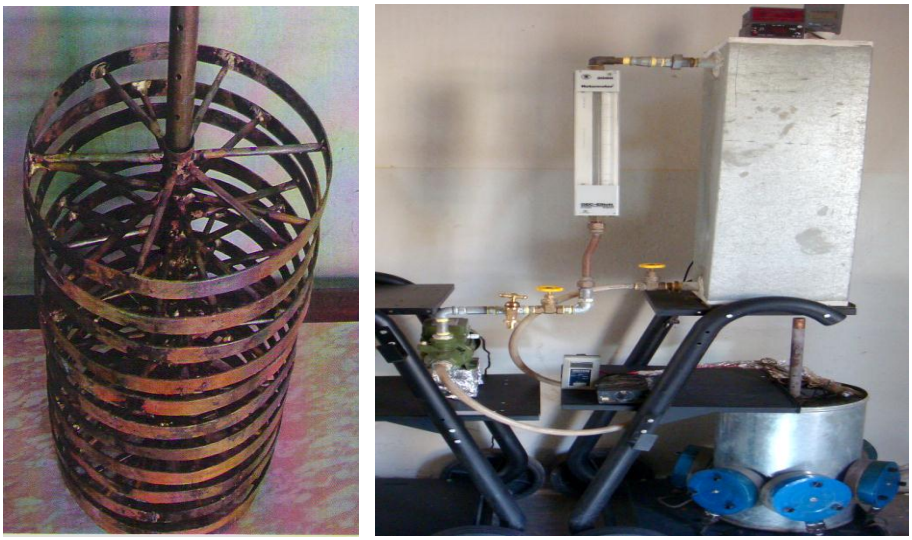

Figure (2): Experimental setup.

The test section of the present experimental work consists of a vertical cylindrical water enclosure with an immersed, removable, screen rings fitted inside the enclosure. The laboratory scale enclosure is constructed from galvanized steel with an inside diameter of (305) mm and a height of (550) mm. The main purpose of using metal screen rings is to increase the heat transfer from the external enclosure wall to the inside water by conduction. In addition, these screens packing should provide a torturous path for the water flow through the enclosure. The system of removable screen packing includes up to twelve horizontal rings through and around which the storage water should pass. As shown in Figure (3), the screen ring packing is fitted inside the enclosure in two arrangement systems (in–line and staggered).

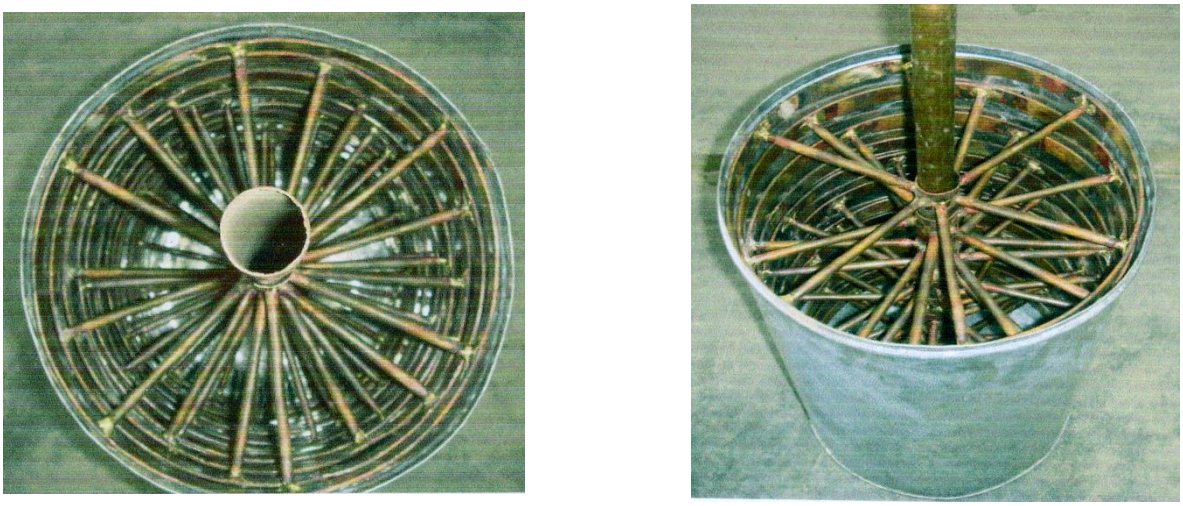

(a): In-line arrangement (b): Staggered arrangement

Figure (3): Removable in–line and staggered screen ring packing fitted inside the enclosure.

During the experimental measurements, the external wall of the enclosure is heated by electric heating elements to a uniform wall temperature. These heating elements should simulate the solar energy heat flux. The water enclosure is covered by an insulated box, so there is no heat loss from it. Therefore, the heat gain to the enclosure is equal to the power of the electric heating elements. The effect of heat gain on thermal gradient inside enclosure will be investigated experimentally. The temperature range investigated of approximately 28°C to 87°C .

The experiments were divided into two categories:

I) Static experiments (without water flow).

II) Dynamic experiments (with charging /discharging water flow).

In the first experiments the water was heated until a specified temperature was reached, and the temperature was monitored during this process. The temperature measurements were taken with 5-min intervals along three hours. In later experiments, after reaching the specified temperature, hot water was discharged at constant mass flow from the top of the enclosure whereas an identical quantity of cold water was charged through its base. The temperature profiles were also measured along the process. After a predefined volume of cold water was charged and the thermocline formed, the charge/discharge process was interrupted, and the degradation of the thermocline zone was observed by monitoring the temperature profiles.

The filling of the tank produces fluid motion that persists for some time and may affect the results. It has been determined that after about two minutes of waiting time between fillings and test running, the detrimental vertical motion had dissipated. In general, tests were started after five minutes of filling and the decay in the temperature distribution beyond this point is studied. The detailed of the thermocouple distribution inside the water enclosure are shown in Figure (4).

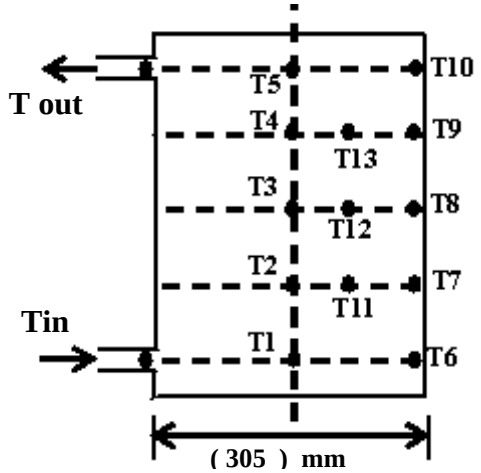

Fig. (4): Locations of the thermocouples inside the water enclosure.

The thermocouples were located at fixed distances of 10 cm intervals along a vertical plane and were attached to a vertical rod, which was inserted into the enclosure at the top. The positions of the thermocouples were chosen based on previous numerical simulation of the temperature profiles. The highest radial temperature gradients occur in the middle part of the enclosure. For this reason, thermocouples were more concentrated in this region, as shown in Figure (4).

Thirteen calibrated thermocouples are distributed at five levels within the enclosure to measure the water temperature. Besides the thirteen thermocouples, twelve others were used; two to measure the water temperature at inlet and outlet of the enclosure, three to measure the water temperature inside the auxiliary water tank, six to measure the external wall temperature and another one for the external environment, where the experiments were performed. The experimental rig has been equipped with an acquisition data system based on a PC to continuously record the temperature values.

Experiments were performed three to four times to check the repeatability and accuracy of the measurements taken. It was found that the temperature data could be repeated to within 4%, indicating a fairly high level of accuracy.

Results and Discussions:

The thermal behavior during static and dynamic operation conditions are important issues and both should be investigated. Static mode represents the most frequent state of the enclosure and dynamic mode has great relations with real time analysis.

The temperature distributions of water in the enclosure that subjected to uniform heat flux are investigated experimentally and theoretically during both static mode of operation (Fig. 5) and dynamic mode of operation (Fig. 6). In general the numerical simulation was able to accurately reproduce the time–dependent heating process in the enclosure. The temperature profiles of the enclosure were examined during 180 min. period with an initial uniform temperature of 31 °C. For both static and dynamic modes of operation, the CFD calculations give an underestimated temperature at the middle of the enclosure height and an overestimated temperature at the top and bottom of the enclosure. However, the numerical and experimental results showed that there is a slight temperature decrease in the middle of the tank height, while a strong thermal stratification exists only at the lower part with a temperature decrease to the bottom of the enclosure.

It can be seen that the numerical model predicts well the transient temperature distribution in the tank during both dynamic and static modes of operation except water at the peak part of the enclosure, where the numerical results were higher than experimental ones.

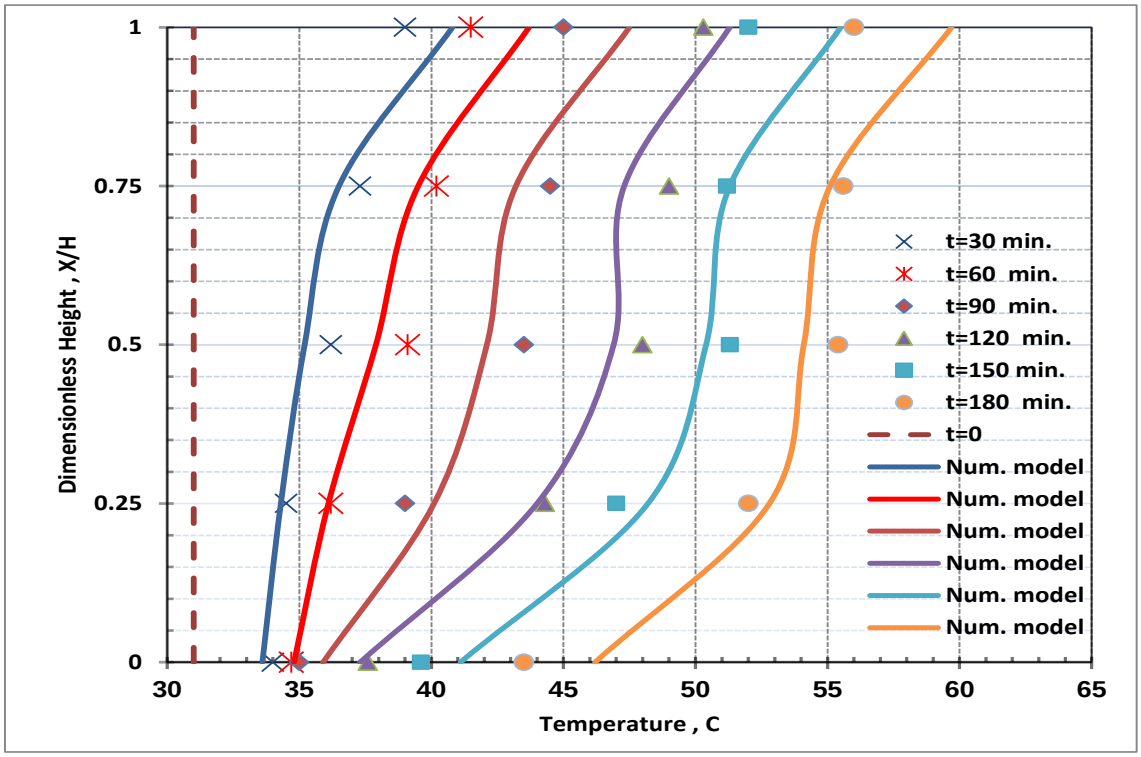

Figure (5) : Comparison between the numerical model temperature profiles and experimental data during static mode of operation.

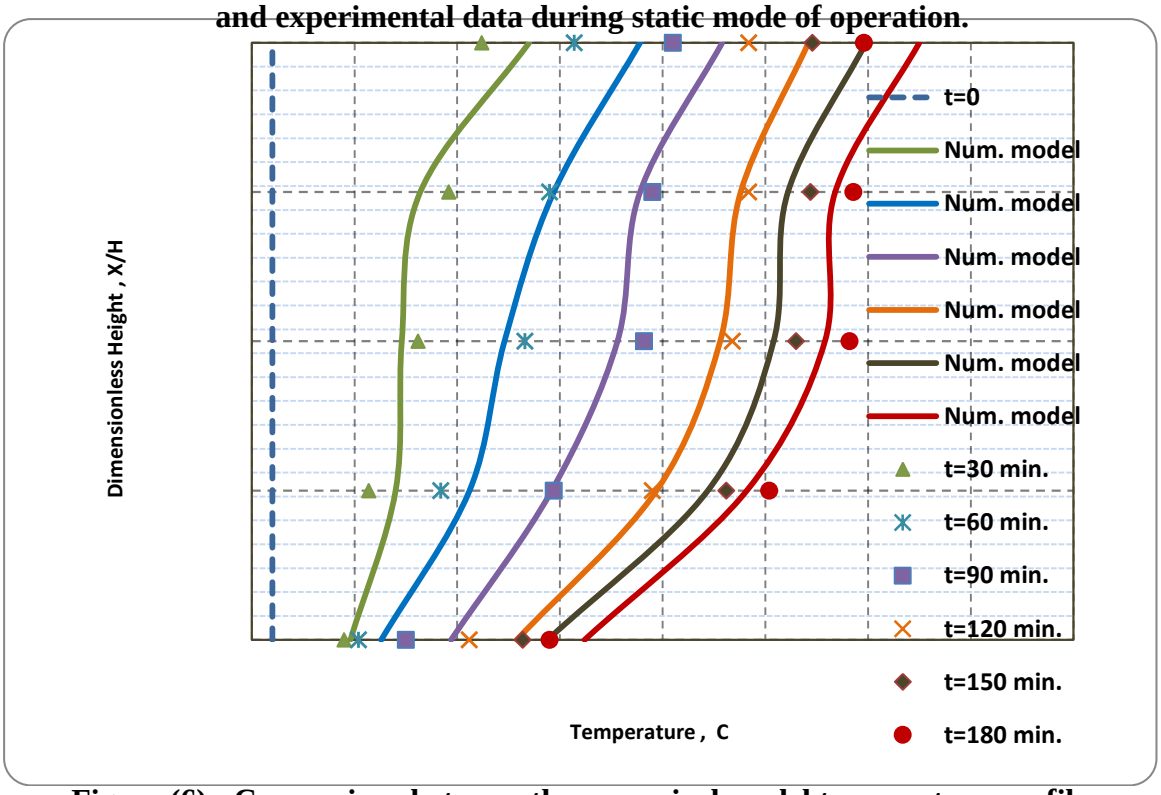

Figure (6) : Comparison between the numerical model temperature profiles and experimental data during dynamic mode of operation.

The influence of ring arrangement is investigated for its potential for enhancing radial conduction heat transfer to the centerline of the enclosure. The impact of adding 3-rings in-line and 3-rings staggered arrangements on axial water temperature profile is shown in Figure (7) during static mode and in Figure (8) during dynamic mode of operation. For the static mode, the thermal response of no rings model is found to have a similar behavior to that for in-line rings and staggered rings but with increase in temperature when adding rings.

However, the enhancement in water temperatures is nearly equal in the enclosure with in-line and staggered arrangements as shown in Figure (7).

For the dynamic mode (Figure 8), the thermal response with rings is clearly different from tank with no rings. However, the in-line arrangement gives higher temperature profile for most of the enclosure height. On the other hand, horizontal rings with staggered configuration add substantial hydraulic resistance to the moving fluid during the dynamic mode. Therefore, it is concluded that using in-line arrangement is better than using staggered rings. During the dynamic mode, an obvious temperature gradient or thermocline has been formed between hot water at the top and cold water in the bottom. It is seems that the thermal stratification within the tank have been achieved because of horizontal rings that increasing the radial heat transfer from the vertical tank wall.

In this work, the water mass flow rate of 1, 2 and 3 liters per minute have been studied. For the studied mass flow rates, the increase of inlet jet velocity do not modifies significantly the thermal response profiles. Therefore, only results with mass flow rate of 2 L/min will be shown up. Also, it may be concluded that in solar energy systems the operational mass flow rate can be increased without damage on stratification profiles. It must be mentioned that the diameter of the inlet and outlet jets have a diameter of ¾ inch, so that, for this mass flow rate, the flow is laminar.

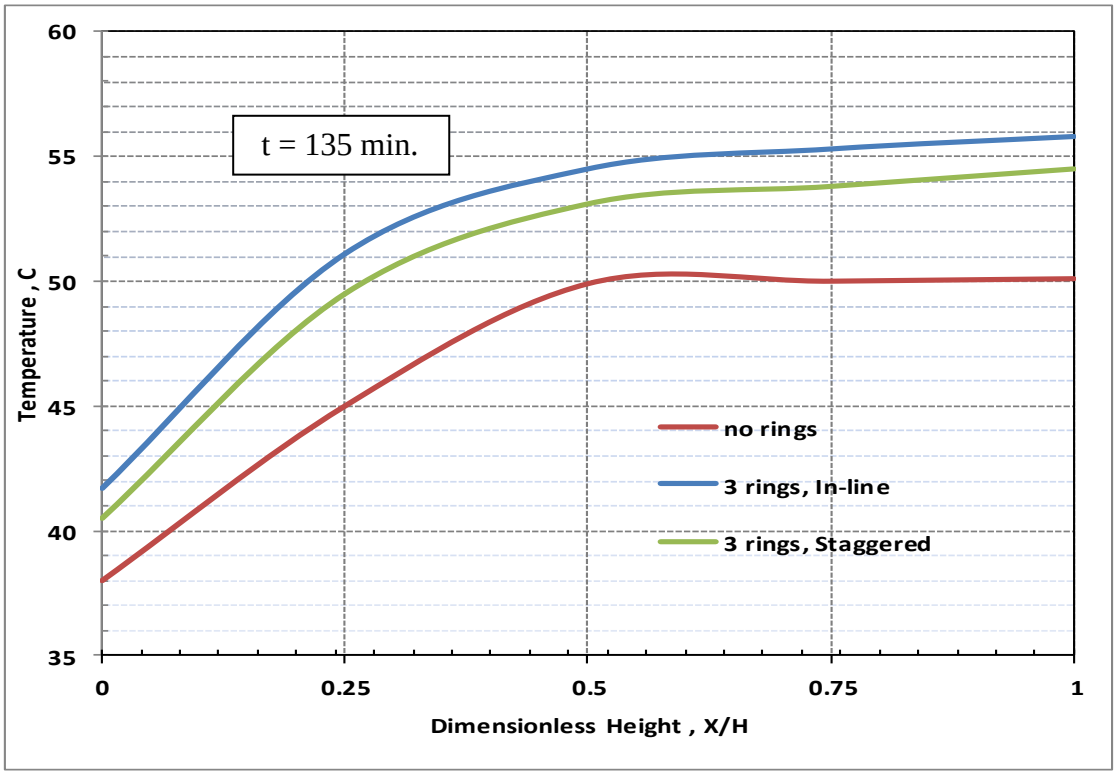

Figure (7) : Effect of metal rings arrangement on the water temperature distribution during static mode of operation.

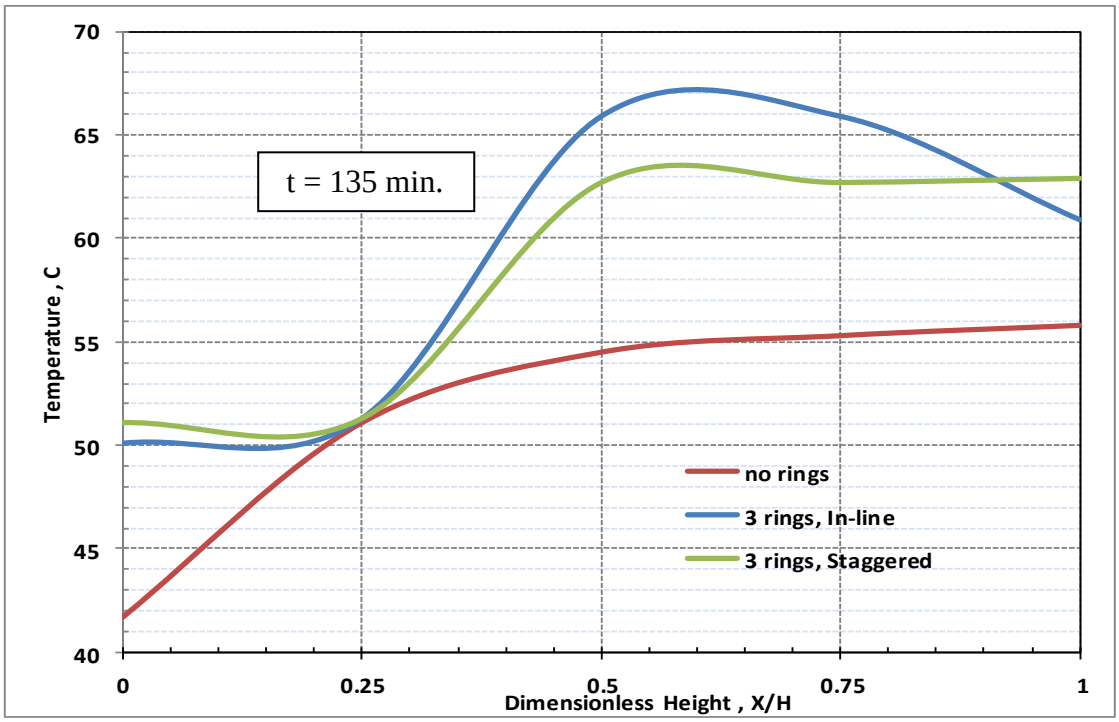

Figure (8) : Effect of metal rings arrangement on the water temperature distribution during dynamic mode of operation.

Figure (9) and (10) show the effect of adding metal rings on the transient temperature distribution at center-line and near wall during static mode (Fig. 9) and during dynamic mode (Fig. 10). In these figures data with and without the rings are compared. It is clear from these figures that water enclosure with no rings behaves differently from that contains metal rings, that is the rings have a significant impact on the center line temperature distribution. The horizontal rings are produce irregular, turbulent flows that additionally enhance heat transfer, and therefore creates rise in the water temperature of the enclosure after about 5 min.

An indication of the complexity of the temperature profiles during the static mode can be seen in Figure (9). It is clear from this figure that using (12) rings is useful only after about 45 min.. However, using 3 and 6-rings give a similar response in enhancing the heat transfer but the 6 rings model produce high fluctuation in the temperature profile. With the progress of time, it's noticed that the 3-rings model always enhance the heat transfer as compared to tank without rings.

During dynamic mode, as can be seen in Figure (10), the general trends are the same but the differences between the predictions increase with the increase in time. The use of (3) and (6) metal rings led to a greater degree of enhancing conduction heat transfer. Using (6) rings inside the enclosure produce high fluctuation in the temperature profile. This secondary effect may be due to a local instability in the flow near wall (such as a transition to turbulence) which causes the hot, near wall, fluid to be injected into the center line at intermediate levels along the enclosure height.

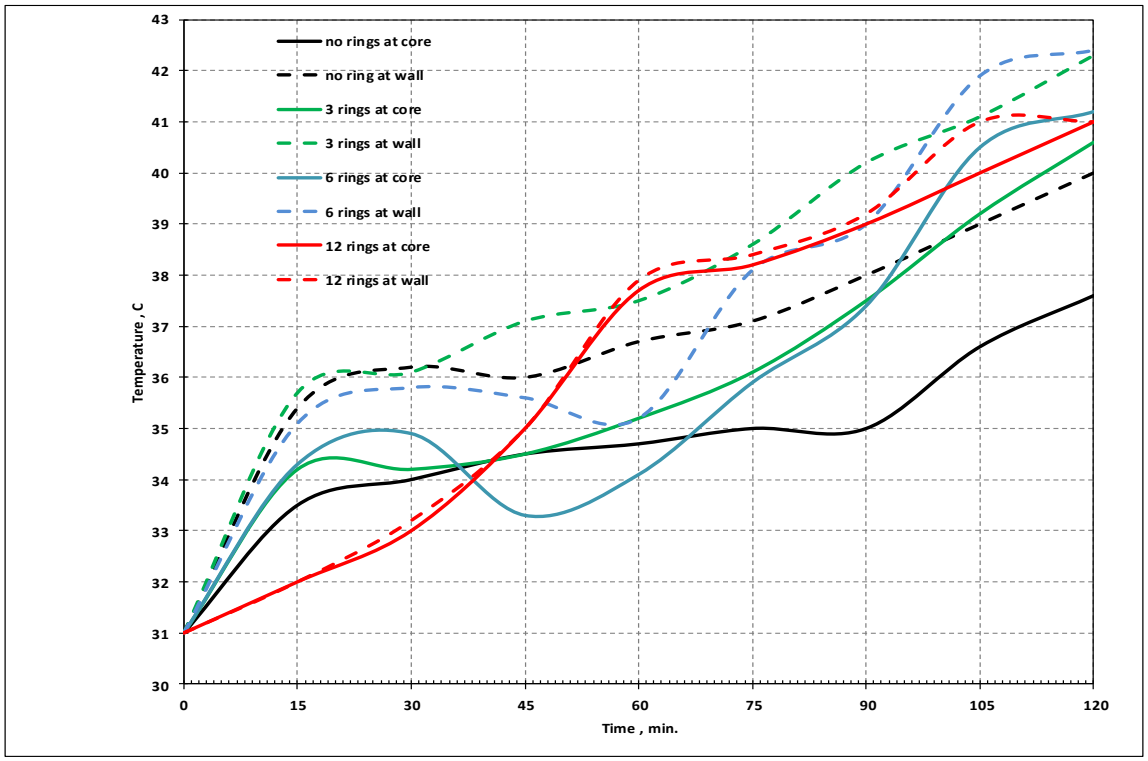

Figure (9) : Effect of adding horizontal rings on water transient temperature at center-line and near-wall during static mode of operation.

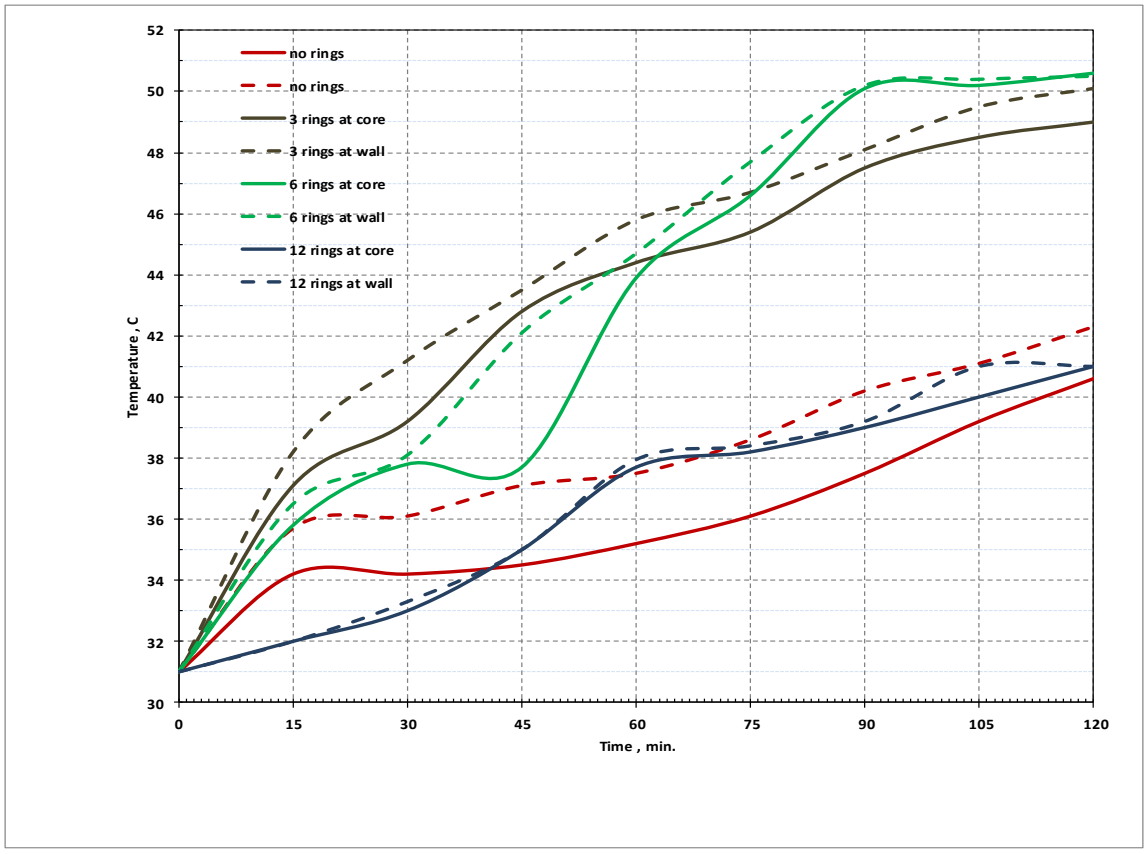

Figure (10) : Effect of adding horizontal rings on water transient temperature at center-line and near-wall during dynamic mode of operation.

It is clear that there is thermal boundary layer develops initially along the heated walls. Due to this heat gain to the conducting side-wall, the fluid close to the enclosure wall has a higher temperature than the fluid at the center of the enclosure. The relative hotter fluid flows up along the tank wall while the fluid with lower temperature flows downwards. It is noticed that at the beginning of heating the side wall water temperature begins to rise immediately, but the center–line temperature does not begin to change until warm water sinks to its level .

In general, it is found that using horizontal metal rings led to less difference between near–wall and center-line temperature due to increasing radial heat conduction from side-wall to the core water. It is clear that using 12 rings make this difference very low during both dynamic and static modes. However, when using (3) or (6) rings this difference became higher but with an increase in the main water temperature, especially during dynamic mode. From all above, it is concluded that using 6-rings model is more useful during both static and dynamic modes for enhancing radial heat conduction from side-wall to water.

Figure (11) and (12) show the temperature distribution along the enclosure radius during static and dynamic modes of operation. As expected, the water close to the conductive metallic wall has a higher temperature than the fluid at the center of the enclosure due to heat gain at wall. The relative hotter fluid close to the wall rises up along the wall, while in the center of the tank, the water with lower temperature flows down to a lower level. During the static mode (Fig.11), it is observed that the center-line temperature is much lower than the near-wall temperature for the case of no metal rings. In the other side, it is clear that there was a very little radial temperature variation during the dynamic mode for the case of no rings. It seems that the side-wall fluid is mixed toward enclosure core due to dynamic motion of water. In general, for both modes of operation, the presence of positive horizontal metal rings increases the radial heat conduction from side-wall to center-line. It is observed that using 3 and 6 rings provide higher radial conduction during static mode. It is found that using 6 rings during dynamic mode provide the higher temperature rise for main enclosure core among the three considered models.

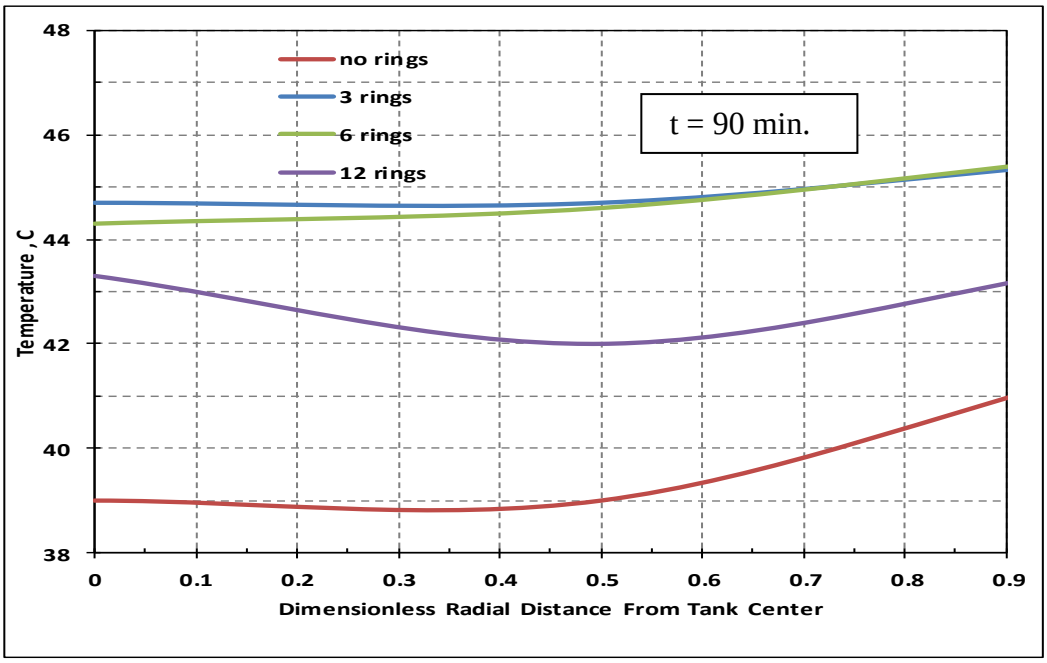

Figure (11) : Radial temperature distribution during dynamic mode .

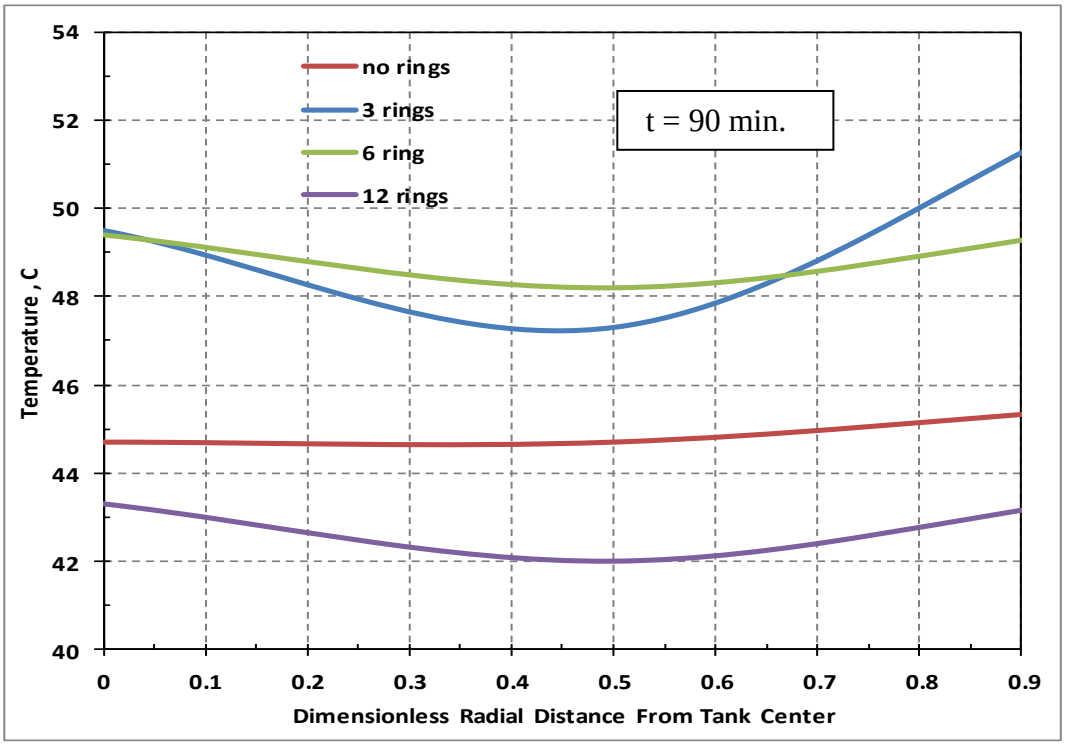

Figure (12) : Radial temperature distribution during dynamic mode .

Predication of laminar natural Nusselt number correlations :

A laminar natural convection inside vertical cylinder was mainly investigated by numerical methods of solving the Navier-Stokes and energy equations [13]. Different heat transfer open literatures and textbooks present empirical correlations for natural convection heat transfer that related to limited boundary conditions [13-20]. These correlations usually account for steady-state processes and comprise cases of either constant surface temperature or constant heat flux. However, in practice, none of these theoretical cases normally occurs. Seara et al.[21] stated that data and correlations to calculate transient natural convection coefficients obtainable in textbooks or in more specific open literature are quite different from the experimentally data. Therefore, they conclude that more research should be carried out in this area.

In this work, it is evident from results that the predication produce by the present numerical model are reasonable in general, however, it is obvious that there are some discrepancy between the experimental data and the computational results for the static mode of operation (Fig. 5). This discrepancy is believed to be due to the effect of natural Nusselt number correlation used in the numerical model. Therefore, the experimental results will be used to formulate new suitable correlations for natural heat transfer inside liquid enclosures subjected to high heat flux.

The local heat transfer coefficient of water inside the enclosure (h_x) is defined as;

$$h_x = K / \Delta T \ . \ \partial T / \partial r \Big|_r$$

The reference temperature difference (ΔT) is the difference between the average temperature of the cross-section of the enclosure (Tav_x) and the side-wall temperature ($T_{x,R}$) at the same height ;

$$\Delta T = T_{x,R} - Tav_x$$

Where, $$Tav_x = 1/\pi \ . \ R^2 \cdot \int_o^R T \Big|_x .2 \pi r \ .dr$$

So, the Nusselt number is calculated by;

$Nu_x = h_x \ . \ x \ / \ K$

Qureshi and Gebhart [22] have proposed a range of ($Ra = 1.2 \times 10^{13} - 4 \times 10^{13}$) for the start of transition from laminar to turbulent flow for water tank with uniform heat flux. Holzbecher and Steiff [17] observed that the transition to turbulent regime is at ($10^{13} < Ra < 10^{14}$). So in this work, the laminar Rayleigh number is taken below 10^{13} .

The mean Nusselt number as a function of enclosure height is shown in Figure (13) at $Ra = 5.1 \times 10^9$. Two models are considered, water enclosure with no-rings and enclosure fitted with 6-rings inside it. The effect of metal rings is clear for enhancing the free convection inside water tanks subjected to high heat flux. However, the lower heat transfer coefficient may be expected near the enclosure bottom for both cases due to lower temperatures.

The results of the calculations are presented in Figure (14) for both no-ring model and 6-ring model. The results of the predicted Nusselt correlations are of a power fit to the data, and may be expressed for no-ring model as ;

$$\mathbf{Nu = 29.98 \times Ra^{0.0975} \quad at \quad 8 \times 10^7 \leq Ra \leq 5 \times 10^{10}}$$

and for six-ring model as ;

$$\mathbf{Nu = 125.5 \times Ra^{0.0633} \quad at \quad 8 \times 10^7 \leq Ra \leq 5 \times 10^{10}}$$

As shown in figure (14), for ($Ra \leq 5 \times 10^8$) the dependence of $Nu = f(Ra)$ is found to tend to the value of (Nu = constant) corresponding to thermal conductivity of motionless liquid. The Nusselt number is found to fluctuate about some average value of 200 for no-ring model and 400 for 6-ring model. The validity of the predicted correlations determined in this work is shown in Figure (14) by comparing them with heat transfer correlation available in open literatures (dashed lines). To the best of authors' knowledge, no previous work has determined natural Nusselt number correlation for liquid enclosure fitted with solid material and subjected to heat flux at the same time. So, no comparison with other results can be done.

The improvement in natural Nusselt number of liquid enclosure subjected to heat flux and fitted with 6-rings arrangement is found to be about two times the value for conventional liquid enclosure with no-rings.

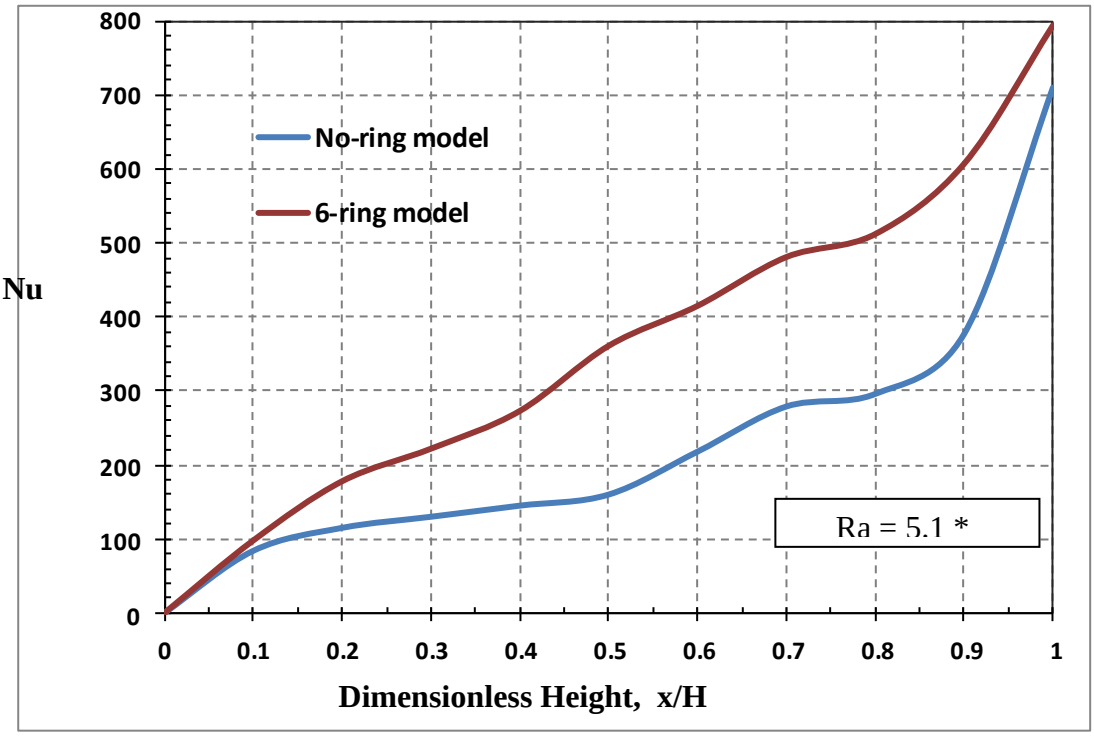

Figure (13) : Relation between vertical height with predicted Nusselt number inside water enclosure subjected to high heat flux.

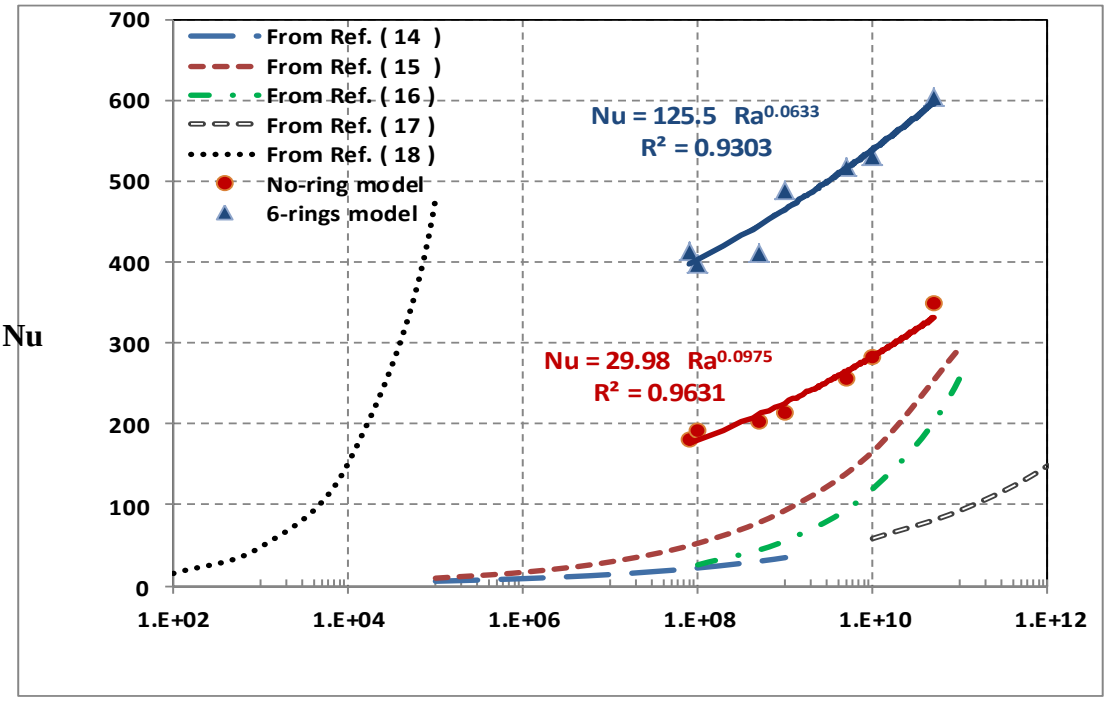

Figure (14) : Comparison between predicted Nusselt number correlations with available open literature correlations.

Conclusions :

In this work, various metal rings were added inside vertical cylindrical enclosure that subjected to high heat flux. The primary objective of the rings is to gain more heat transfer to the liquid inside enclosure. The transient temperature distributions of water were investigated experimentally and theoretically during both static and dynamic modes of operations. The two-dimensional computational code was based upon the conservation equations of mass, momentum and energy, and developed by adding fourth equation that take in consideration energy transport between liquid and the solid material of the enclosure.

The predicted profiles have been found close to those obtained experimentally, except for water at peak part of the enclosure, where the numerical results were higher than experimental ones. The developed numerical simulation has been provided a better understanding and planning of the experimental tests.

Adding metal rings has been found to produce a significant enhancement in radial heat transfer from side-wall to the main liquid inside enclosure. The results indicated that using in-line arrangement is better for enhancing heat transfer than using staggered rings. It has been found that the optimum number of rings is six. This six-ring model is found to be more effective for enhancing heat transfer as compared to the other cases under investigation during both static and dynamic modes of operation.

In order to provide the practical engineers with more reliable Nusselt number correlations, two new correlations for natural heat transfer inside liquid enclosures subjected to high heat flux have been formulated as ;

$$Nu = 29.98 \times Ra^{0.0975} \quad , \text{(for no-ring model)}$$

and, $$Nu = 125.5 \times Ra^{0.0633} \quad , \text{(for six-ring model).}$$

The new correlations are applicable for local Rayleigh number within the rang of (8×10^7 to 5×10^{10}). The validity of the predicted correlations have been compared to correlations available is open literatures. The natural Nusselt number is found to be around a constant value for Rayleigh number below (5×10^8). The improvement in natural Nusselt number of liquid enclosure with six-ring model is found to be about two times the value for conventional liquid enclosure with no-rings.

The recommended use of metal rings inside liquid enclosures subjected to heat flux, and the predicted Nusselt number correlation related to it, will add to local knowledge a significant mean to gain more heat in large scale concentrated solar power plants.

References:

1- Dehghan, A. and A. Barzegar, "Thermal performance behavior of a domestic hot water solar storage tank during consumption operation", Energy Conversion and Management , 52, 2011.

2- Abdulsada, Ghanim. K and Mohammed H. Mahmoud, "Enhancing Thermal Stratification in Liquid Storage Tanks During Relaxation Periods", Engineering and Development Journal, Vol. 12, No.1, 2008.

3- Akinjiola, O. P. and U. B. Balachandran, "Concentrated Solar Thermal (CST) system for fuelwood replacement and household water sanitation in developing countries", Journal of Sustainable Development; Vol. 5, No. 6, 2012.

4- Mc Govern R. and W. Smith, "Optimal concentration and temperatures of solar thermal power plants", Energy Conversion and Management, 60, 2012.

5- Shyu RJ. Lin JY. And Fang LJ., "Thermal analysis of stratified storage tanks", ASME J. Solar Energy Eng., 111, 1989.

6- Hariharan K., and K. Badrinarayana, "Temperature stratification in hot water storage tanks", Energy, 16 (7), 1991.

7- Zachar A. Farkas I. and Szlivka F., "Numerical analyses of the impact of plates for thermal stratification inside a storage tank with upper and lower inlet flows", Solar Energy, 74, 2003.

8- Altuntop, N., M. Arslan, V. Ozceyhan and M. Kanoglu, "Effect of obstacles on thermal stratification in hot water storage tanks", Applied Thermal Eng., Vol. 25, 2005.

9- Haltiwanger, J. and J. Davidson, "Discharge of a thermal storage tank using an immersed heat exchanger with an annular baffle", Solar Energy, Vol. 83, pp 193-201, 2009.

10- Han, Y., R. Wang and Y. Dai, "Thermal stratification within the water tank", Renewable and Sustainable Energy Reviews, Vol. 13, pp 1014-1026, 2009.

11- Mawire, A. and S. H. Taole. "A comparison of experimental thermal stratification parameters for an oil/pebble-bad thermal energy storage (TES) system during charging", Applied Energy, 88, 2011.

12- Valmiki, M., W. Karaki, P.Li, J. Lew, C. chan and J. Stephens , "Experimental investigation of thermal strong processes in a thermocline tank", Journal of Solar Energy Engineering, Vol. 134, 4 , July 2012.

13- Martynenko, O. and P. Khramtsov, Free Convection Heat Transfer, Springer Berlin Heidelberg, 2005.

14- Polezhaev, V.I., " Non-stationary Laminar Heat Convection in a Closed Domain for a Given Heat Flux", Nlekh. Zhidkosti Gaza, No.4, 109, 1970.

15- Hiddink, J, J. Schenk and S. Bruin, "Natural convection heating of liquids in closed container", Appl. Sci. Res., 32 , 217 , Aug. 1976.

16- Goldstkin, R. and S. Tokuda, "Heat transfer by thermal convection at high Rayleigh numbers", Int. J. Heat Mass Transfer, 23, 5, 1980.

17- Holzbecher, M. and A. Steiff, "Laminar and turbulent free convection in vertical cylinders with internal heat generation", Int. J. Heat Mass Transfer, 38, 15, 1995.

18- Lemembre, A. and J.P. Petit, "Laminar natural convection in a laterally heated and upper cooled vertical cylindrical enclosure", Int. J. Heat Mass Transfer, 41, 16, 1998.
19- Bejan, A. and A.D. Kraus, Heat Transfer Handbook, John Wiley and Some Inc., USA, 2003.
20- Incropera, F.P., D.P.De Witt, T. Bergman and A. Lavine, Fundamentals of Heat and Mass Transfer , 7th edition , John Wiley and Sons Inc., USA , 2011.
21- Seara, J., F. Uhia and A. Dopazo, "Experimental transient natural convection heat transfer from a vertical cylindrical tank", Applied Thermal Eng., Vol.31, Aug. 2011.
22- Qureshi, Z.H. and B. Gebhart, "Transition and transport in buoyancy driven flow in water adjacent to a vertical uniform flux surface", Int. J. Heat Mass Transfer, 21, 1978.

Nomenclatures:

Cp : specific heat at constant pressure
D :diameter of the enclosure
G : gravitational acceleration
Gr : Grashof number
H : convection heat transfer coefficient
H : height of the enclosure
H/D: aspect ratio
K :thermal conductivity
Nu :Nusselt number
P :pressure
Pr :Prandtl number
q : heat flux
r : radial coordinate
R : radius of the enclosure
Ra : Rayleigh number
t : time
T : Temperature
u : velocity in x-direction
v : velocity in r–direction
x : Axial direction

Greek Letters:
α : thermal diffusivity
β : thermal expansion coefficient
μ : dynamic Viscosity
ρ : density
ν : kinematic viscosity

Subscripts:
L : Liquid
S : Solid

Designing of Soft Core Processor System with Direct Memory Access (DMA) Mode

Mazin Rejab Khalil **Rafal Taha Mahmood**

Basrah University. College of Engineering

E-mail: mazin_r_khalil@yahoo.com **E-mail: rafal_1985_r@yahoo.com**

Abstract

A soft core processor system is constructed using embedded design techniques and it is configured on Field Programmable Gate Arrays (FPGAs). The system is accommodated to act with Direct Memory Access (DMA) mode using suitable Xilinx Intellectual Property (IP) core. A dual data rate synchronous dynamic random access memory (DDR_SDRAM) with 64 Mbyte capacity is introduced to the system and accessed by the DMA controller. The controller is performed to transfer programmable quantity of data from source address to destination address without intervention of the processor.

Spartan-3E slice is used and programmed using Xilinx Platform Studio (XPS) which is provided by Xilinx integrated software environment at (ISE 10.1). The system performance is tested by transferring data from matlab media to the DDR_SDRAM and vice-versa, mat lab 2012a version software is used for this type of data transfer.

تصميم نظام المعالج المصغر ذات النواة المبرمجة بتقنية الوصول المباشر للذاكرة

مازن رجب خليل **رفل طه محمود**

المستخلص :

تم تصميم نظام معالج ذات نواة مبرمجة باستخدام تقنيات الانظمة المطمورة لينفذ على البوابات المنطقية القابلة للبرمجة الحقلية وبنظام الوصول العشوائي للذاكرة . تم ربط ذاكرة للوصول العشوائي نوع DDR_SDRAM بسعة ٦٤ ميكا بايت بنظام المعالج المصغر لغرض استخدامها في نظام الوصول المباشر DMA وتم اضافة مسيطر على الذاكرة بشكل نواة قابلة للبرمجة لتمكين النظام من العمل بطريقة الوصول المباشر للذاكرة وذلك لنقل البيانات بين الذاكرة (كمصدر) والأجهزة المحيطة (كهدف) للوصول وبالعكس . تم استخدام شريحة Spartan_3e وبرمجتها باستخدام بيئة ISE10.1 الصادرة من شركة Xilinx وتم اختبار أداء النظام باستخدام بيئة matlab اصدار ٢٠١٢ لنقل البيانات بين الذاكرة وبيئة matlab وبالعكس بطريقة الوصول المباشر للذاكرة .

1. Introduction

Direct memory access (DMA) system is used usually to transfer certain quantity of data between source and destination address without processor intervention.

In [1] a DMA controller is designed to act with Micro blaze processor system configured on Spartan-3A FPGAs. The system is designed to perform data transfer between the internal block RAM and external peripheral.

In [2] a DMA system is depicted to act with multiprocessor connected via On-chip Processer Bus (OPB).

In [3] a DMA mode is proposed to act as a universal synchronous/ a synchronous Receiver/Transmitter (USART) IP soft core in Altera kit with AVALON bus.

In this work a DDR-SDRAM external memory is used instead of the limited capacity internal block RAM with newest version of Processor Local Bus (PLB v4.6). A communication interaction between a matlab media and the designed soft core processor system is suggested to transfer data between them according to DMA techniques.

DMA is a feature of modern computers that allows certain hardware subsystems within the computer to access system memory for reading and/or writing independently of the central processing unit. Computers that have DMA channels can transfer data to and from devices with much less CPU overhead than computers without a DMA channel [3].

The processing unit which controls the DMA process is known as DMA controller. Typically the job of the DMA controller is to setup a connection between the memory unit and the I/O device; the data can be transferred with much less processor overhead. Figure (1) shows the block diagram of DMA operation. When an interrupt signal is activated, the processer goes to idle case and open circuit its connection with buses. The buses become under the control of the DMA controller[4].

The XPS Central DMA Controller operates on the PLB using independent master and slave interfaces. It responds as a slave when its registers are being read and written. It initiates read and write transactions as a master when a DMA operation is in progress. The master and slave connections of the XPS Central DMA operate as 32-bit PLB agents. However, either the master or slave can connect to a PLB with wider data paths (64-bit or 128-bit) and conduct transactions with wider slaves or masters[5].

DMA Operation forwards fast data transfer between source and destination compared with data transfer with processor intervention.

Figure (2) shows the block diagram of the DMA controller core [5].

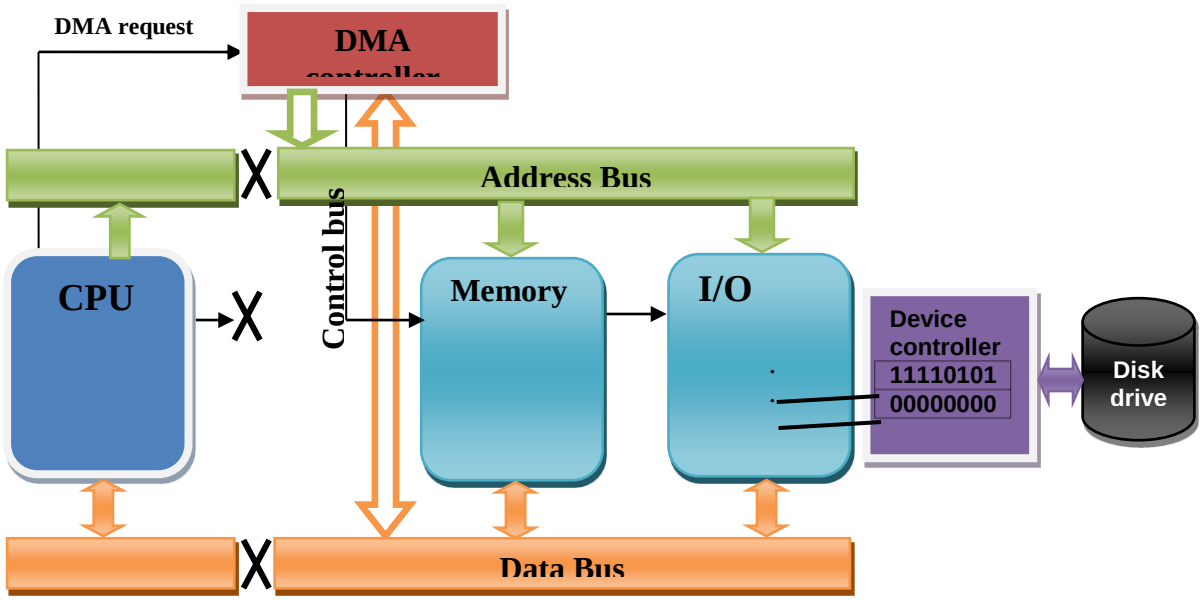

Figure 1: Operation of a DMA Controller [4]

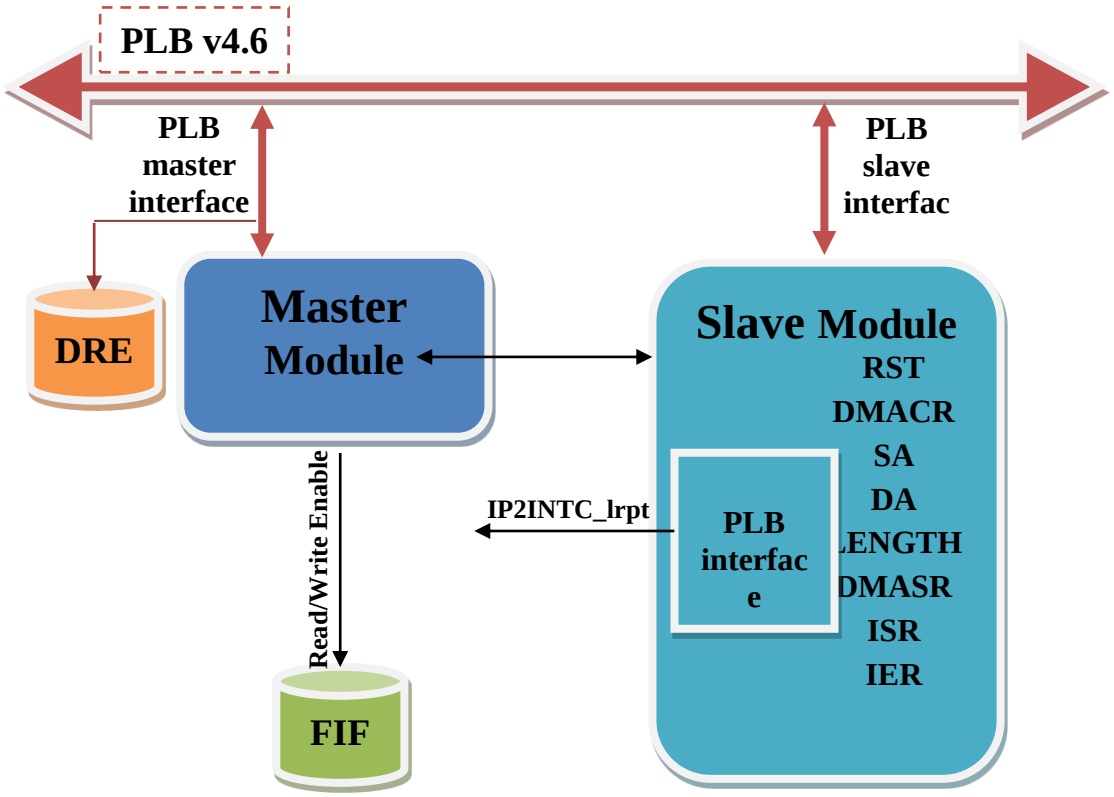

Figure (2): The Block Diagram of the DMA Controller Core

The core is composed of three modules; slave attachment module, master attachment module and memory buffer.

In the slave attachment module the DMA responds to PLB transactions to read and write the DMA registers to modify source address, destination address, length of data, DMA status and interrupt status when DMA operation proceeds. These modifications are performed

by using the Source Address register (SA), the Destination Address register (DA), the Length Register (LR), the DMA Status Register (DMASR), the Interrupt Status Register (ISR), the Interrupt Enable Register (IER) and DMA Control Register (DMACR).

In the master attachment module, the DMA performs read and write transactions as a PLB master to transfer the amount of data specified in the length register from source address to destination address with updating the source, destination, length and status registers during the DMA transfer. The memory buffer is 16*32 internal data buffer that is used to support PLB burst transfer to speed up the DMA operation [5].

The suggested procedure in this work starts by constructing the embedded processor system, introducing the DMA controller to the system and programming the resultant hardware using C-language to accommodate the system to operate in DMA mode. The system is tested to verify its functionality by transferring data between matlab media and the designed processor system; the results are displayed at Hyper Terminal media and real time chip scope window.

2. System Design

The system under consideration is designed using three stages. In the first stage the hardware part of the soft processor system is constructed. While in the second stage a DMA controller core is added to the system. Finally in the third stage the resultant system is programmed by C-language to operate in a DMA mode.

3. Soft Core Processor System Design

Using embedded design techniques [6], a soft core processor system as shown in Figure (3) is designed using the platform studio provided by Xilinx ISE (10.1) software. Figure (3-a) shows the block diagram of the hardware part , Figure (3-b) exhibits the assembly view and Figure (3-c) displays the address map of the system .

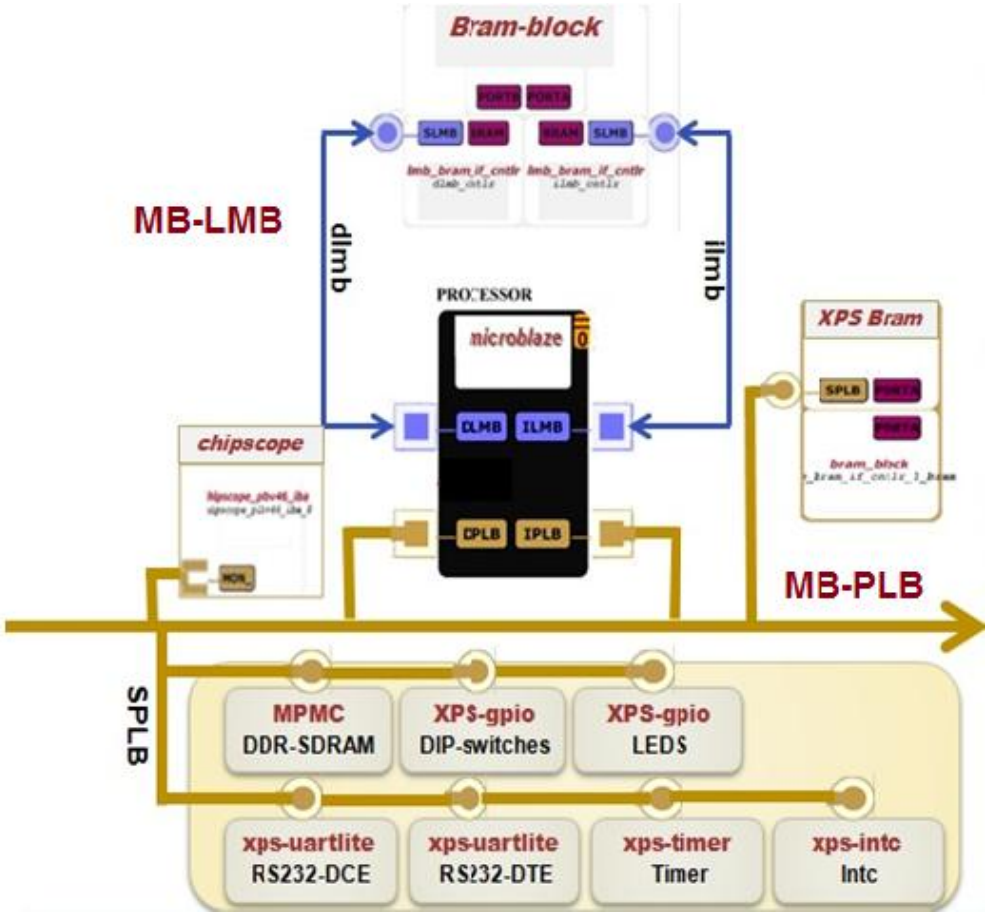
Bram-block
MB-LMB
dlmb
ilmb
PROCESSOR
microblaze
DLMB
ILMB
DPLB
IPLB
XPS Bram
chipscope
MB-PLB
SPLB
MPMC
DDR-SDRAM
XPS-gpio
DIP-switches
XPS-gpio
LEDS
xps-uartlite
RS232-DCE
xps-uartlite
RS232-DTE
xps-timer
Timer
xps-intc
Intc

a

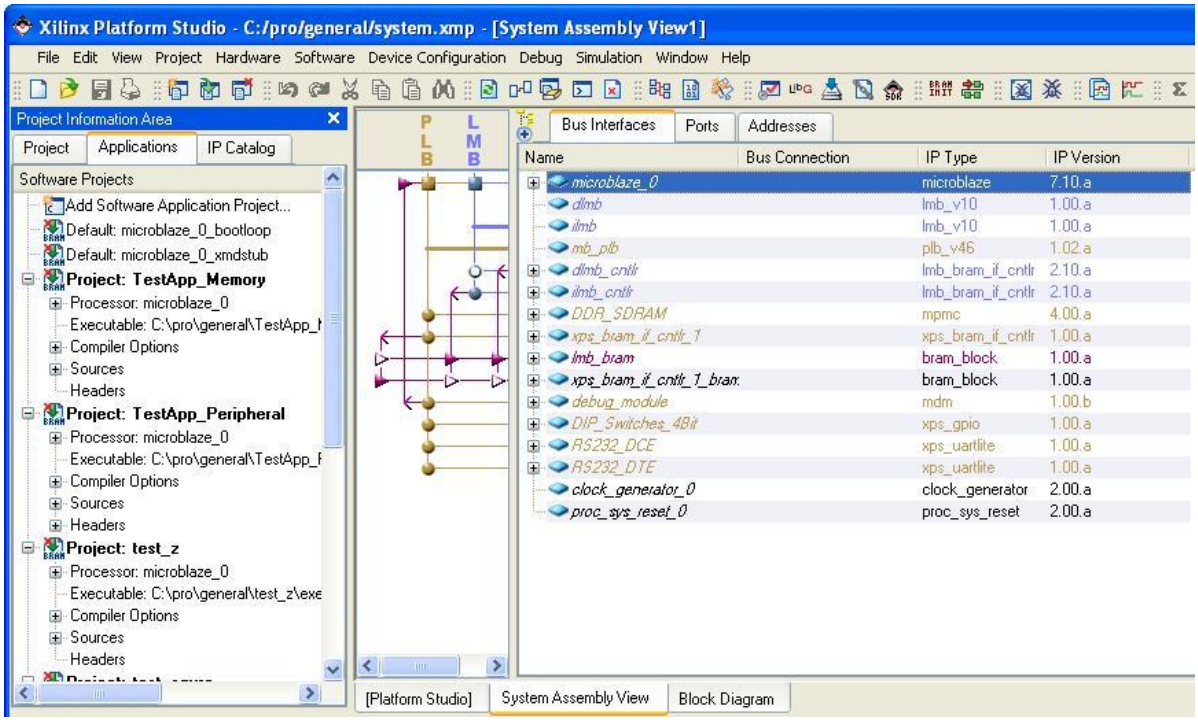
Xilinx Platform Studio - C:/pro/general/system.xmp - [System Assembly View1]
File Edit View Project Hardware Software Device Configuration Debug Simulation Window Help
Project Information Area
Project Applications IP Catalog
Software Projects
Add Software Application Project...
Default: microblaze_0_bootloop
Default: microblaze_0_xmdstub
Project: TestApp_Memory
Processor: microblaze_0
Compiler Options
Sources
Headers
Project: TestApp_Peripheral
Project: test_z
Bus Interfaces
Ports
Addresses
Name
Bus Connection
IP Type
IP Version
microblaze_0
dlmb
ilmb
mb_plb
dlmb_cntlr
ilmb_cntlr
DDR_SDRAM
xps_bram_if_cntlr_1
lmb_bram
debug_module
DIP_Switches_4Bit
RS232_DCE
RS232_DTE
clock_generator_0
proc_sys_reset_0
[Platform Studio]
System Assembly View
Block Diagram

b

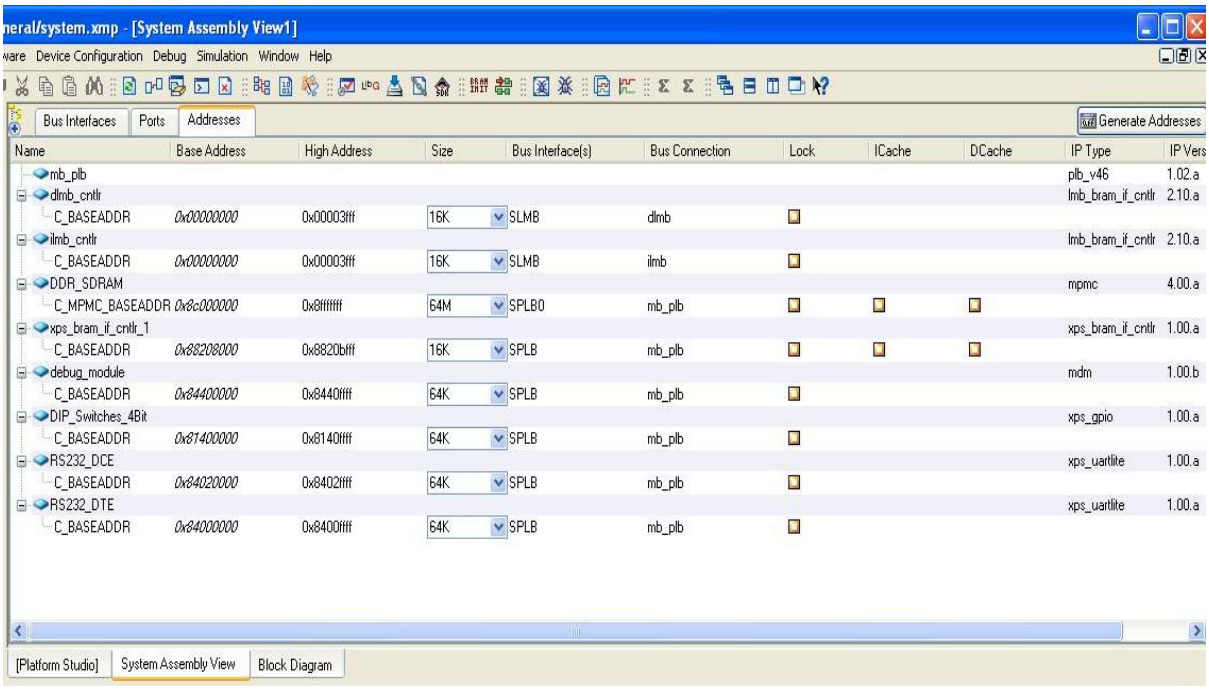

c

Figure (3): The Hardware Part of Designed Soft Core Processor System

a. **The block diagram of the system.**

b. **The assembly view of the system.**

c. **The address map of the system.**

4. Adding DMA Controller

The platform studio provides an environment in which an available IP cores can be accessed. The DMA controller core is available in the form IP module that can be dragged from the IP catalogue to the system assembly view. The following steps are adopted to perform successful DMA introduction to the system:

1. Using bus interface window the DMA core is connected to the PLB in the slave and master module and the core parameters are customized to adapt with the processor system.
2. Using the port window the interrupt port of the controller is connected to the interrupt port of the processor.
3. Using the address window, the address map of the system is reconfigured to take the DMA controller into consideration.

4. The resulting hardware part of the system is shown in Figure (4). Figure (4-a) shows the assembly view of the system with DMA core, Figure (4-b) shows the address map of the system with DMA core.

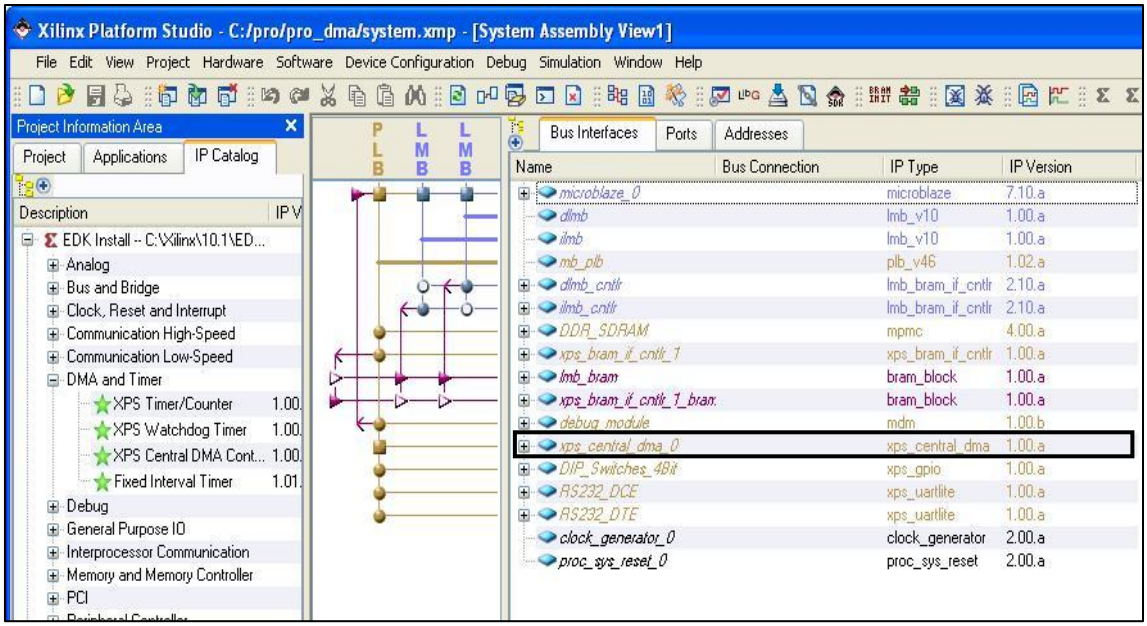

a

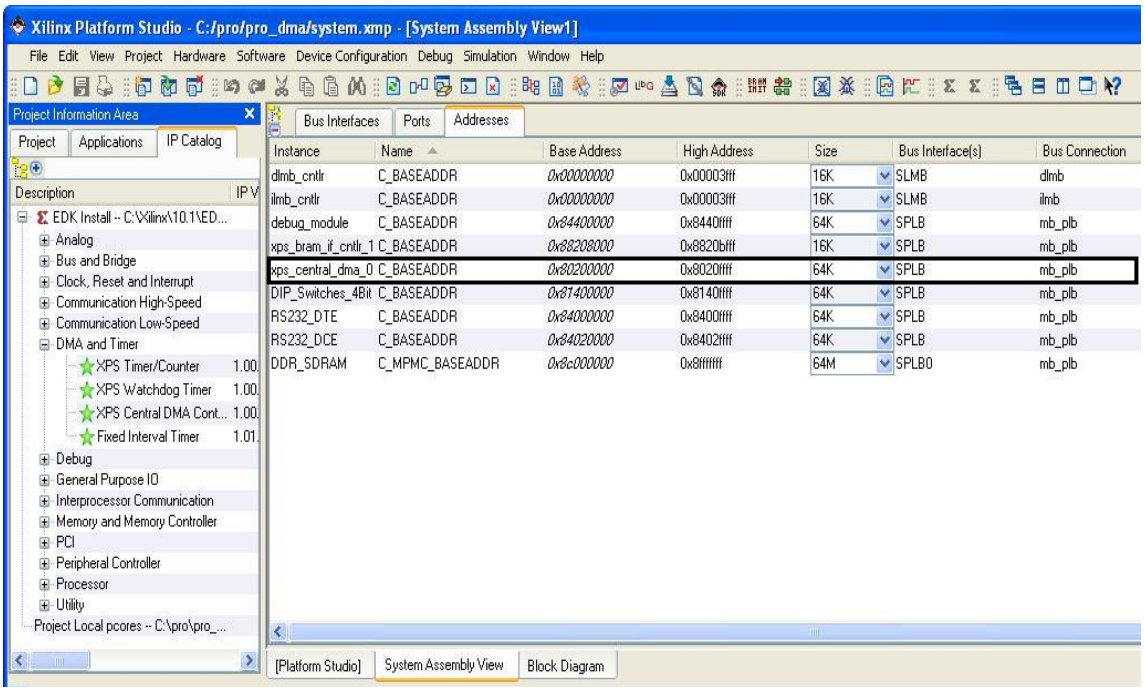

b

Figure (4): The hardware part of designed soft core when adding DMA core.

a. The assembly view of the system.

b. The address map of the system.

5. Programming the system

The C -language is used to program the resultant system hardware to operate in DMA mode, Figure (5) shows the flow chart of the prepared program. Application Peripheral Interfaces (API) are used to make the hardware peripheral be sensed by the C –language compiler. The APIs are software drivers constructed in the form of C -language functions. The following APIs are used in the prepared program.

#define XDmaCentral_mWriteReg(BaseAddress, RegOffset, Data)

Where:

Base address: represents the base address of the DMA controller.

Offset address: the offset address of each register in the controller. The offset address of each register is shown in Table [1].

Data: the data request to program the register.

Table (1): XPS Central DMA Controller Registers [4]

Register Name	Base Address+ Offset(hex)	Default Value(hex)	Access
Software Reset Register (RST)	C_BASEADDR + 0	NA	Write
DMA Control Register (DMACR)	C_BASEADDR + 4	80000004	R/W
Source Address (SA)	C_BASEADDR + 8	00000000	R/W
Destination Address (DA)	C_BASEADDR +C	00000000	R/W
Length (LENGTH)	C_BASEADDR + 10	00000000	R/W
DMA Status Register (DMASR)	C_BASEADDR + 14	00000000	Read
Interrupt Status Register (ISR)	C_BASEADDR + 2C	00000000	Read/TOW
Interrupt Enable Register (IER)	C_BASEADDR + 30	00000000	R/W

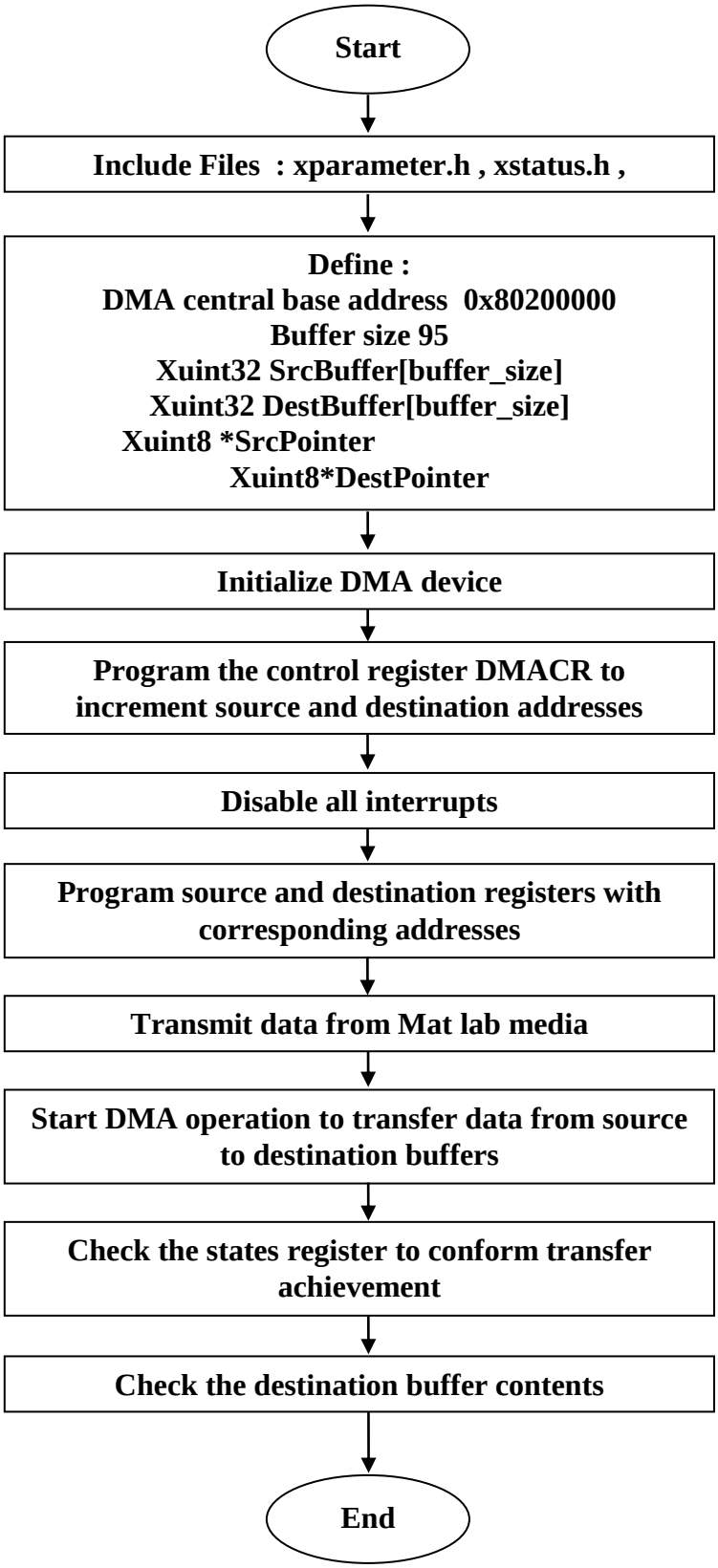

Figure (5): The flow chart of designed system programing

6. Results

Figure (6) shows the data read from destination buffer and the data transferred from the source buffer displayed in hyper terminal window.

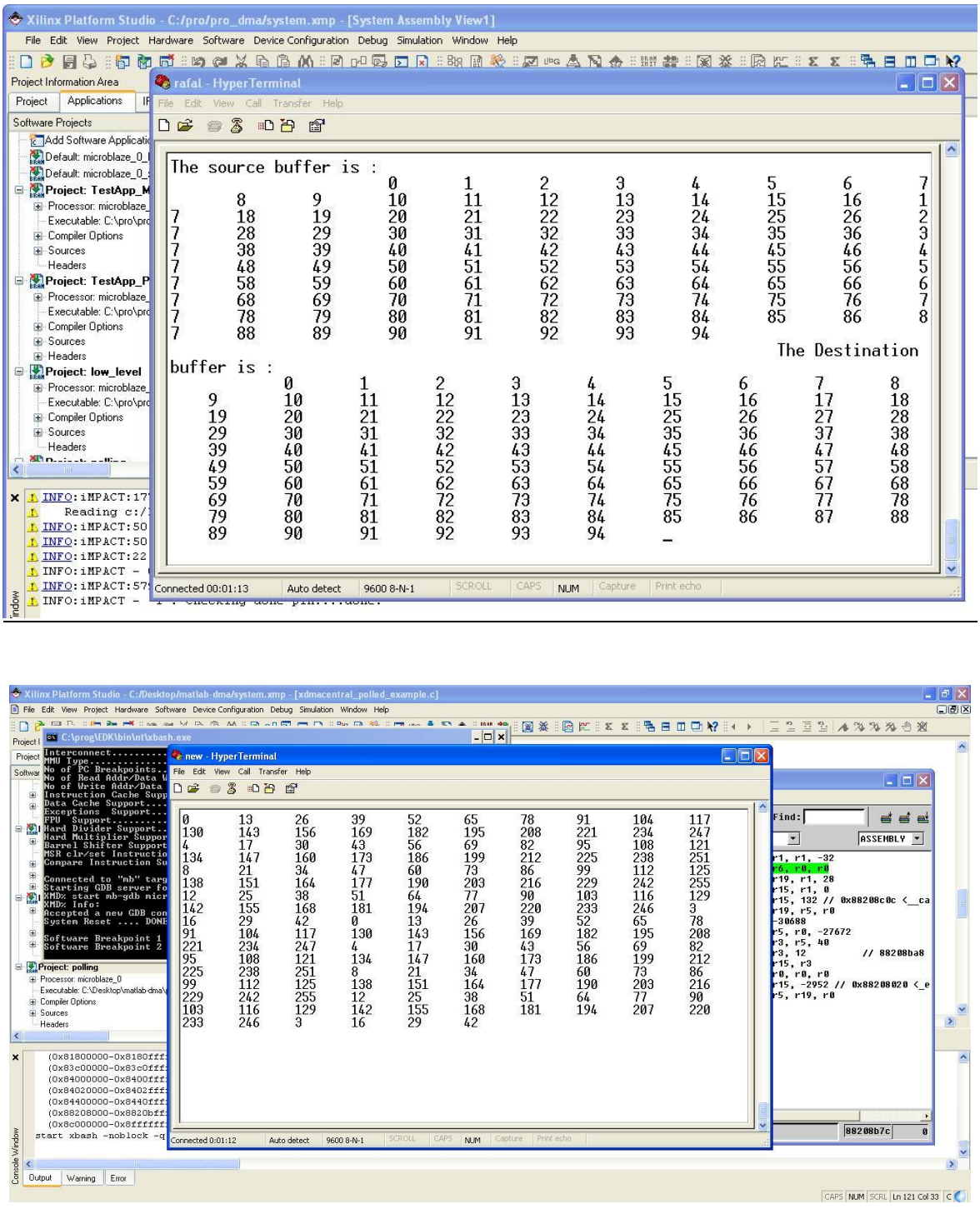

Figure (6): The Data Transfer from Source to Destination Buffer

Figure (7) shows the operation of data transfer displayed on chip scope window during write data bus cycle. Figure (7-a) presents the data flow with address during write bus cycle, Figure (7-b) presents the data flow with address during write bus cycle zoomed out.

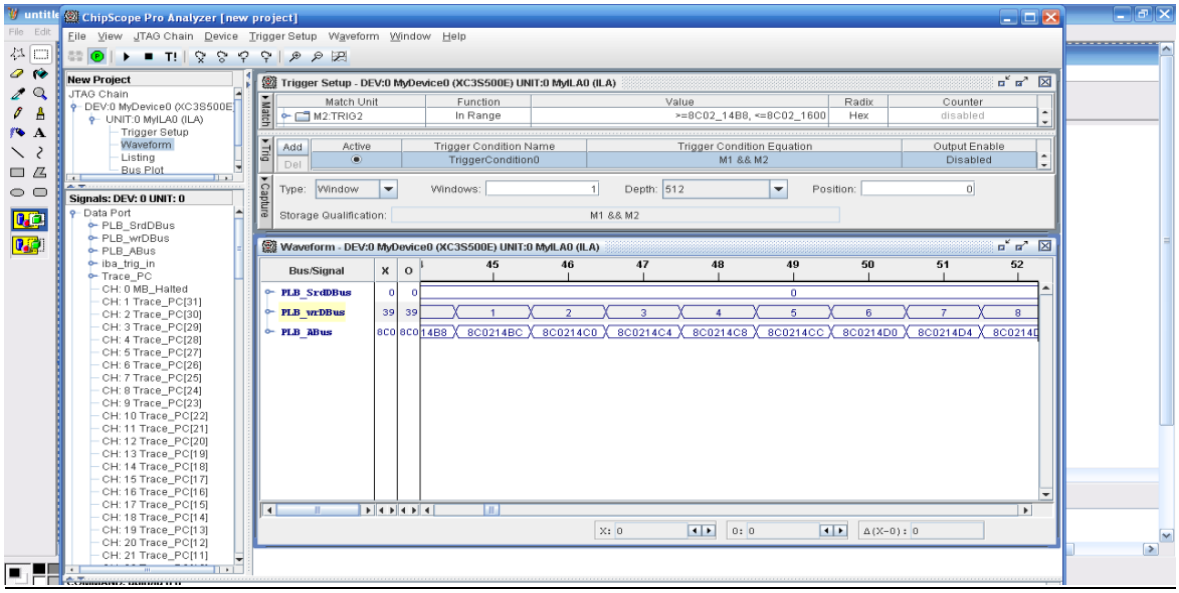

a

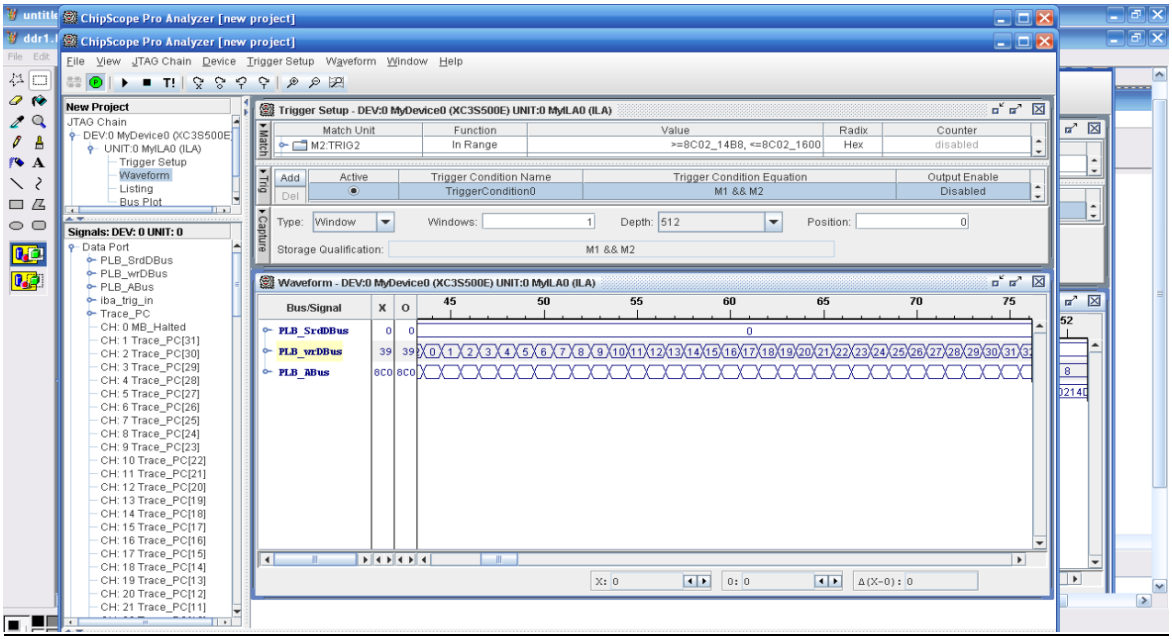

b

Figure (7): Data transfer based on DMA operation displayed on chip scope window

a- **data flow with address during write bus cycle**

b- **data flow during write bus cycle zoomed out**

7. Conclusions

A soft core processor system is designed using embedded design techniques and configured on FPGA slice. The system is accommodated to act in DMA mode to transfer data from a peripheral to external DDR-SDRAM memory by adding a DMA IP core to the system and programming the resultant hardware using C-language with suitable API. The transferred data width is 32-bit which is adaptable the PLB data width. The system can operate with (40K) internal Block RAM and external (64M byte) DDR-SDRAM. The designed system can be used efficiently with video graphic arrays (VGA) to display graphics on a screen since the speed of data transfer between memory and the VGA controller is sufficient to capture all the pixels of the image frame(640columns x 480 rows) in 60 screen/second display mode, this rate of data flow could not be attained with processor systems without DMA operation mode.

References:

1- Bakshi A. B., Burman A. B., & Chakraborty A. Ch. , 2014 , "Development of DMA Controller for Real Time Data Processing in FPGA Based Embedded Application", IOSR Journal of VLSI and Signal Processing (IOSR-JVSP) . E-ISSN: 2319-4200, P-ISSN No.: 2319-4197, www.iosrjournals.org, PP 01-08 .

2- Tumeo A. T., Monchiero M. M., Palermo G. P., Ferrandi F. F. & Sciuto D. S., 2008, "Lightweight DMA Management Mechanisms for Multiprocessors on FPGA", 1-4244-1998 IEEE .

3- Allam P. A., 2013, "Design And Implementation Of USART IP Soft Core Based On DMA Mode", International Journal of Computer Trends and Technology (IJCTT), ISSN:2231-2803, http://www.ijcttjournal.org, page no.:3580-3584.

4- http://www.talktoanit.com/A+/aplus-website/lessons-io-principles.html

5- XILINX, 2010, "LogiCORE IP XPS Central DMA Controller (v2.03a)" , Web Site: www.xilinx.com, DS579.

6- Schmidt A. G., 2010, "Embedded Systems Design with Platform FPGAs", TK7895.E42S27 2010, diacriTech, India, Web Site: www.elsevter.com/permissions.

Effect of Coolant Jet Holes Direction on Film Cooling Performance

. Assim H. Yousif,.Amer M. Al-Dabaghand Muwafag Sh. Alwan
University of Technology, Baghdad, Iraq

Abstract: The film cooling effectiveness and local heat transfer coefficient for coolant jet holes direction (orientation angle), have been investigated. Experimental investigations were done on a flat plate by using a single test transient IR thermograph technique. Evaluation of the cooling performance is obtained by estimated both film cooling effectiveness and heat flux ratios. Three models of coolant jet holes are investigated, each model consists of two rows of holes arranged in a staggered way with different orientation angles. Model (1) downstream row with acute angle and the upstream row with obtuse angle; model (2) both rows with obtuse angles, while model (3) both rows with acute angles. The holes diameter is 4mm, the longitudinal distance between the upstream and downstream rows (X/D) is 4D, and the span distance between two neighboring holes (S/D) is 3D**.** Three blowing ratios of (BR= 0.5, 1.0, and 1.5) were used in the investigation program. In order to predict the flow behavior numerically for the cases under investigation CFD code is introduced. The numerical investigation shows two large vortices, pair of counter rotating vortex and horseshoe vortices, both vortices have major effects on cooling performance. The experimental results showed that the film cooling effectiveness increases as blowing ratio increases for models (1 and 2), while decreases for model (3), and model (1) provide better performance than the others at high blowing ratios.

Keywords: Film cooling, Blowing ratio, Effectiveness, Jet holes direction.

تأثير أتجاه فتحات البثق البارد على الأداء الحراري لغشاء التبريد

تم دراسة تأثير أتجاه فتحات البثق البارد (زاوية الأتجاه والميل) على فعالية غشاء التبريد و معامل أنتقال الحراره الموقعي.حيث تم أجراء التجارب العملية بأستخدام تقنية الصوره الحراريه للاشعة تحت الحمراء (IR) على صفيحه مستويه بألية الفحص الأنتقالي الواحد. أن الحصول على تقييم أداء التبريد تم بأستخدام فعالية غشاء التبريد وتقنية نسبة الفيض الحراري. وقد تم أختبار ثلاث عينات ، كل عينة من هذه العينات تحتوي على صفين من الثقوب المرتبة بشكل متعرج بزوايا أتجاه مختلفة. العينة الاولى الصف الامامي بزاوية نفث حادة والصف الخلفي بزاوية نفث منفرجة, وفي العينة الثانية كان صفي النفث بزاويتين منفرجتين وفي العينة الثالثة كان صفي النفث بزاويتين حادتين. تم تثبيت قطر الثقوب بمقدار (D=4 mm)، المسافة الطولية بين الصفين (X/D=4)، والمسافة البينية (العرضية) بين فتحات الصف الواحد بمقدار (S/D=3).أجريت التجارب بأستعمال ثلاث نسب من النفخ هي (BR=0.5, 1.0,and1.5). لمعرفة سلوك الجريان تم أستخدام الحلول العددية. أعطت الأختبارات العددية المستخدمة تنبؤ جيد لسلوك النفث البارد المحقون مع الجريان الرئيسي الحار. أن الأختبارات النظرية التي تم أستخدامها في مجال الجريان وعند منطقة التداخل بين التيارين البارد والحارأظهرت وجود نوعين من الدوامات الكبيره، زوج من الدوامات المتعاكسة و دوامات حدوة الحصان. وقد أظهرت النتائج النظرية أن هذه الدومات تلعب دورا" رئيسيا" في التأثير على أداء التبريد. أظهرت النتائج العملية أن فعالية الغشاء تزداد بزيادة نسبة النفخ لنموذجين الاول والثاني بينما تقل للنموذج الثالث. كما أظهرت النتائج ان النموذج الاول يعطي أداء أفضل عند مقارنته مع النموذجين الاخرين عند نسب النفخ العالية.

1-Introduction

Turbine blades require better cooling technique to cope with the increase of the operating temperature with each new engine model. Film cooling is one of the most efficient cooling methods used to protect the gas turbine blades from the hot gases. Jet holes arrangement offers reliable technique help to improve the coolant effectiveness of the film cooling.

Film cooling primarily depends on the coolant-to-mainstream pressure ratio or can be related to the blowing ratio, temperature ratio (T_c/T_m), the film cooling hole location, configuration, and distribution on a turbine elements film cooling. In a typical gas turbine blade, the range of the blowing ratios is of about 0.5 to 2.0, while the (Tc/Tm) values vary between 0.5 and 0.85 **Han and Ekkad[1].**

Injecting behavior of two rows of film cooling holes with opposite lateral orientation angles have been investigated by **Ahn et al. [2]** in which four film cooling hole arrangements were considered including inline and staggered ones. Detailed adiabatic film cooling effectiveness distributions were measured using thermochromic Liquid Crystal to investigate how well the injecting covers the film cooled surface. They found that staggered opposite lateral arrangement shows best cooling performance.

Dhungel et al. [3] obtained simultaneously detailed heat transfer coefficient and film effectiveness measurements using a single test transient IR thermography technique for a row of cylindrical film cooling holes, shaped holes. A number of anti-vortex film cooling designs that incorporate side holes. They found that the presence of anti-vortex holes mitigates the effect of the pair of anti-vortices. Experimental and numerical investigations were done by **Lu et al. [4 and 5]** to measure and to predict the film cooling performance for a row of cylindrical holes. They used adiabatic film effectiveness and heat transfer coefficients were determined on a flat plate by using a single test transient thermograph technique at four blowing ratios of 0.5, 1.0, 1.5 and 2.0. Four test designs crescent and converging slot, trench and cratered hole exits, were tested. Results showed that both the crescent and slot exits reduce the jet momentum at exit and also provide significantly higher film effectiveness with some increases in heat transfer coefficients.

Dia and Lin [6] investigated numerically three film cooling configurations, (cylindrical hole, shaped hole, crescent hole). All holes were inclined at 35° on a flat plate. All simulations are conducted at blowing ratio of 0.6 and 1.25, length to diameter ratio of 4 and pitch-to-diameter ratio of 3. They use (RANS) equations, the energy equation, and two-layer $(k-\epsilon)$ turbulence models. For the numerical investigation the commercial CFD software FLUENT with standard $(k-\epsilon)$ turbulent models is applied. They found that the crescent hole exhibits the highest film cooling effectiveness among the three configurations both in spanwise and streamwise especially downstream of the interaction of the two holes.

Lee and Kim [7] evaluated the effect of geometric variables of a laidback fan-shaped hole on the film cooling effectiveness using a Reynolds-averaged Navier-stokes analysis. The shape of the laidback fan-shaped hole is defined by four geometric design variables: the injection angle of the hole, the lateral expansion angle of the diffuser, the forward expansion angle of the hole, and the ratio of the length to diameter of the hole. They concluded that the increase of the forward expansion angle makes a reduction of film cooling effectiveness, and the lateral expansion angle has the biggest impact among the four geometric variables on the spatially averaged film cooling effectiveness.

Numerical prediction of **Alwan. [8]** shows that the flow field structure of injected holes present vortices such as counter pair kidney vortex and horseshoe vortex have major effects on cooling performance, in which the strength of the kidney vortex decreases and the horseshow vortex was lifting up, leading to an improvement in the coolant performance. Therefore numerical model was suitable to design holes arrangement futures of film cooling system by introducing oriented holes row over single jet holes row.

Most literature focuses on the study of the effective parameters of film cooling for one row film holes in the forward direction with mainstream. There is no information available for the row of holes in the backward direction with mainstream flow, also lack information available for two rows of film cooling on forward direction. However, at the present work experimental and numerical investigations were done to evaluate the cooling performance (film cooling effectiveness and heat transfer coefficient) by using a single test transient IR thermograph technique for a different holes direction and at different blowing ratio.

2-Experimental Facilities

Low speed open duct test rig is used at the present investigation to supply uniform hot air to the test section as shown in figure 1. The settling chamber of the test rig contains a series of electrical heaters and row of screen to ensure adequate hot air of uniform temperature throughout the test rig. The hot air routed through a convergent- divergent contraction having a rectangular cross-section before flowing through the test section. In order to allow the air to reach the desired temperature, the air is initially routed out away from the test section by using a by-bass gate passage. The temperature of the air is continuously monitored at the exit of the gate and when the desired temperature is reached, the gate is gradually fully opened and the hot air is passes into a test section through a rectangular duct. The operating velocity in the test section is controlled to run from 20 to 40m/s. The test section has 50mm width and 100mm height. The bottom plate of the test section is made of (234x123) mm Plexiglas of 10mm thickness and used as the test model.

A centrifugal air blower was used to supply the coolant air to the plenum. The plenum was located below the test model. The coolant air enters a plenum then ejected through holes into the test section. The coolant air pressure is measured at the inlet of the test section. Digital thermometers were used to measure the mainstream and coolant air temperature. Pre-testing showed that all holes exists constant desired flow rate and temperature.

Two rows of staggered holes with opposite orientation angles are included in the present study. The orientation angles (γ) is defined as the hole orientation toward the cross-flow in the mainstream and the inclination angle (θ) is defined as the angle between the centerline of the hole and the surface of the test wall as shown in figure 2. Three models at different holes direction are shown in table (1). Each model consists of two rows of holes arranged in a staggered arrangement. For model 1, the inclination angle of the upstream and downstream rows are fixed at (θ =30°), and the orientation angle of (γ =0°) and (γ =180°) for the downstream and upstream row holes respectively. For model 2, the jet injected angles of upstream and downstream holes are fixed at (θ =30°) and (γ =0°). While for model 3, the jet injected angles of upstream and downstream holes are fixed at (θ =30°) and (γ =180°). Each of holes (upstream and downstream row) contains eight holes. The holes diameter is 4mm, the longitudinal distance between the upstream and downstream rows (X/D) is 4D, and the span distance between two neighboring holes (S/D) is 3D**.** Data collected only for three middle holes for each row to reduce the effects of the side wall as shown in figure (3).

2-1 Surface temperature measurement

The surface temperature of test model was measured using an infrared thermographs technique. IR thermograph infrared camera type Fluke Ti32 is used at the present investigation. This camera is able to precisely record temperature variations. The IR system is greatly affected by both background temperature and local emissivity. The test surface is sprayed with mat black color to increase the emissivity like a perfect black body. The temperature measurement taken is not accurately recorded unless the IR system is calibrated.

The system was calibrated by measuring the temperature of the test surface using thermocouple type K and the reading of IR camera. The test surface is heated by mainstream hot air. The measured of temperatures obtained by both ways are recorded and stored during the heating process until achieving a steady state condition. Due to the emissivity of the test surface the temperature obtained by IR camera is differ from the temperature obtained by the

thermocouple, therefore IR camera reading is adjusted until both temperatures reading are matched.

2-2 Film cooling effectiveness and heat transfer coefficient estimation

Consider the transient flow over a flat plate as shown in figure 4. In this case the test plate is initially at a uniform temperature T_i, and the convective boundary condition is suddenly applied on the plate at time t > 0. Now, heat assumed to be conducted only in the x-direction and perform an energy balance on the plate, therefore the one-dimensional transient conduction equation is

$$\frac{\partial^2 T}{\partial x^2} = \frac{1}{\alpha}\frac{\partial T}{\partial t} \quad (1)$$

The main approximation often applied to analyze transient conduction shown in Figure 4 is the semi-infinite approximation. The semi-infinite solid assumptions are valid for present investigation for two reasons. The test duration is small, usually less than 60 seconds. Secondly, the hot air flowing over the test surface made from Plexiglas of, low thermal conductivity, low thermal diffusivity, and low lateral conduction. Therefore the solution of equation (1) as given by **Holman and Bhattacharyya [9]** is as follows:

$$\frac{T_w - T_i}{T_m - T_i} = 1 - \exp\left[\frac{h^2 \alpha t}{k^2}\right] erfc\left[\frac{h\sqrt{\alpha t}}{k}\right] \quad (2)$$

Where T_w measured by using IR camera, all the other variables in the equation (2) are either known variable or measured variable except the heat transfer coefficient (h).

In film cooling case, the film should be treated as a mixture of air mainstream and the coolant air, as shown in figure 5, the mainstream temperature (T_m) in equation(2) has to be replaced by the film temperature (T_f), therefore equation (2) become as:

$$\frac{T_w - T_i}{T_f - T_i} = 1 - exp\left[\frac{h^2 \alpha t}{k^2}\right] erfc\left[\frac{h\sqrt{\alpha t}}{k}\right] \quad (3)$$

A non-dimensional temperature term is known as the film cooling effectiveness (η), and is defined as:

$$\eta = \frac{T_f - T_m}{T_c - T_m} \quad (4)$$

Equation (3) has two unknowns (h and T_f), to solve this equation, two sets of data points required to obtain the unknowns like:

$$\frac{T_{w1} - T_i}{T_f - T_i} = 1 - exp\left[\frac{h^2 \alpha t_1}{k^2}\right] erfc\left[\frac{h\sqrt{\alpha t_1}}{k}\right] \quad (5)$$

$$\frac{T_{w2} - T_i}{T_f - T_i} = 1 - exp\left[\frac{h^2 \alpha t_2}{k^2}\right] erfc\left[\frac{h\sqrt{\alpha t_2}}{k}\right] \quad (6)$$

In this case, a transient infrared thermograph technique will be used to obtain both h η from a single test as described by **Ekkad et al. [10]**. Thus, two images with surface temperature distributions are captured at two different times during the transient test.

A net heat flux ratio is the ratio of heat flux to the surface with film cooling to the heat flux without film cooling. This term is used to measure the combined effect of film effectiveness and heat transfer coefficient **Ekkad and Zapata** [**11]**:

$$\frac{q''}{q_o''} = \frac{h}{h_o}\left(1 - \frac{\eta}{\emptyset}\right) \quad (7)$$

The value for the overall cooling effectiveness (ø) ranges between 0.5 and 0.7.A typical value is Ø = 0.6 according to **Albert et al. [12]**, and this in general assumed in the present experimental analysis.

The IR images for models surface at each investigated test was captured and stored by thermal camera. These images are transferred to PC. Smart View Software program supplied with Camera can be used to limit the selected area to avoid the effect of the test section walls. The IR images converted to corresponding temperature digital values and then saved as data in Excel sheet.

MATLAB programs Software are prepared using a semi-infinite solid assumption to introduce the film cooling effectiveness and heat transfer coefficient contours. Equations, (4), (5), (6), and (7) may be solved using MATLAB Software, Smart View Software, and Excel Software. The data were collected from the selected area denoted by (A_o); this area included only six staggered jet holes as shown in Figure (3).

The measurement uncertainty was determined by using the methodology given by **Kline and McClintock [13]**.Error estimates for each variable are as follows: wall temperature$\Delta T_w = \pm 2$ ℃, initial temperature$\Delta T_i = \pm 2$ ℃, mainstream temperature$\Delta T_m = \pm 0.2$ ℃, and coolant temperature $\Delta T_c = \pm 0.2$ ℃. The camera frame rate is 60 Hz resulting in a time error $\Delta t = \pm 0.125\ sec$ and the test surface properties (α and k) uncertainty are taken from tabulated values, as a custom, 3% relative uncertainty is assumed for both variables. The resulting average uncertainty for heat transfer coefficient and film effectiveness is ±8.2% and ±11.0%, respectively.

3- Numerical procedure

In the present study, air is taken as the working fluid and the flow characteristics are assumed to be steady flow, Newtonian fluid, incompressible fluid (Mach number=0.11), turbulent flow, three dimensional. The numerical computation area was matched to the experimental domain instead of computing only two holes with symmetry boundary conditions. FLUENT version (12.1), GAMBIT software and Auto CAD 2011will be used to create, grid for the system geometry and then simulate the film cooling for the three geometry model and three blowing ratio. The solution of the Reynolds Averaged Navier-Stokes and energy equations is obtained by using the FLUENT software. Fluent is based on an unstructured solver using a finite volume approach for the solution of the RANS equations. The system geometry shown in figure 6 consists of the box with dimensions (128x12x50) mm for the hot mainstream, box with dimensions (35x12x20) mm for coolant jet and the different model geometry of two rows of holes as shown in table 1. The system geometry is drawn by using (Auto CAD 2011 code). The diameter of cooling hole is 4mm.The coolant conditions were maintained the same in all cases and the mainstream flow rate was altered to change the blowing ratios. The Mainstream temperature was set at 322 K and the coolant temperature was set at 302 K. At the exit plane, pressure level was specified along with zero streamwise gradients for all other dependent variables.

The current study used the standard $(k-\varepsilon)$model for the simulating the turbulent flows in film cooling. The standard $(k-\varepsilon)$model is economical with reasonable accuracy for a wide range of turbulent flows and it is widely used in heat transfer simulation **Versteeg and Malalasekera [14]**.There are some general guidelines to create a good mesh. These guidelines are shortly called rules of QRST standing for (Quality, Resolution, Smoothness, and Total cell count) **Ozturk [15]**.The importance of quality parameter is the face alignment; it is the parameter that calculates skewness of cells. Elements with high skewness should be avoided. The way of checking whether the solution is grid independent or not is to create a grid with more cells to compare the solutions of the two models. Grid refinement tests for average static temperature on hot surface indicated that a grad size of approximately (2.5 million cell) provide sufficient accuracy and resolution to be adopted as the standard for film

cooling system. The nodes near the test plate surface were adjusted so that average y+ value was about 20 near the test plate surface which is within the range of **Jones and Clarke [16]**.The most significant factor to be monitored for the present model is the average static temperature on hot surface. When the average static temperature on hot surface value monitor converged it is unnecessary to go further on with the iterations and wait even if the residuals do not fall below the defined convergence criteria.

4- Results and Discussion

Figure 7 shows the contours of film cooling effectiveness for three models. The film cooling effectiveness increases with increasing the blowing ratios for model 1 and model 2, while for model 3 the effectiveness values decreases with increasing the blowing ratio. Near the hole exit and downstream, model 2 exhibit more uniformity of η values as the blowing ratios increased more than the other models for all blowing ratios. For model 3 the η contours exhibit high values of η at a hole downstream area at a low BR (BR=0.5) and η decreases with an increase in BR. This behavior only exists at model 3. Model 1 provides better performance when compared with other models at high blowing ratios (BR=1 and 1.5), because different jet holes arrangement gave different flow behavior. The behavior of flow in three dimensional domains is a complicated flow regime. To simplify the case and to make the flow recognizable and readable, the flow will be presented in two dimensions in a plane perpendicular and parallel to the cross flow at different plane location. When the coolant jet flow with the direction of hot mainstream (γ =0°), multiple vortex structures are produce where two large vortex structures have been detected, counter rotating vortex pair (CVP), and horseshoe vortices. CVP plays an important role in the contribution of jet lifting off, this can be seen clearly in the case of low momentum jet (BR=0.5) and the case of high momentum jet (BR=1.5), in which the horseshoe vortex is strongly influenced by high jet momentum **Dia and Lin [6]**. While when coolant jet flow opposite to the direction of hot mainstream (γ =180°), the main stream creates a local variation of pressure at the hole exit. The pressure of the injected air on the upstream side of the hole is elevated, thus locally reducing the jet velocity; and pushing up the hot stream depending on the blowing ratio. On the downstream side of the hole, the pressure falls and locally increases the exit velocity. As the cooled air penetrate into the hot stream, its momentum decreases up to the momentum of the main stream then bend back toward the surface causing lee vortex.

The pressure variation at the hole exit create a reverse flow where part of the cooled air exits in the direction tangent and normal to rims hole reducing the jetting effect at hole rims, which was responsible for creating kidney vortex as in the forward injection. This reverse flow creates pair of vortex similar to the kidney vortex downstream but in a plane parallel to the main stream$(CVP)_p$, this vortex is sweeping near the surface and pushing away the horseshoe vortex where moderate and wider protection area are obtained at low and high BR around the hole area. For model 1, two types of vortices are created, one $(CVP)_p$, while the second is (CVP) as shown in figure 8. For model 2 two pairs of vortices $(CVP)_p$ are appeared in a plane parallel to hot mainstream flow 1mm above the surface as shown in figure 9. In model 3 four vortices exist in the vertical plane in the hole downstream as shown in figure 10.

As a matter of fact, the enhancement of the blade surface protection is done by keeping the local heat transfer coefficient (h) as low as possible. The local heat transfer coefficients are calculated from the data of two IR images taken in successive times. Figures 11 represents the effect of blowing ratio on local heat transfer coefficients for models (1, 2 and 3), (h) increases with increasing BR models (1 and 2), while it decreases with increasing BR for model 3. At low blowing ratios (BR=0.5), model 3 provides high heat transfer

coefficient values than models 1 and 2. As the blowing ratio increases to 1 and 1.5, model 1 gave higher heat transfer coefficient than models 2 and 3.

Figure (12a, b and c) shows (η_{sa}) variation with (X/D) for the same three models. (η_{sa}) is calculated as the average values taken from the local reading of 46 pixels in spanwise direction in twenty streamlines location downstream from the hole exist. The streamwise distance between each two successive spanwise location is (D).Model 2 shows different behavior than that of the other models as shown in figure (12 .a, b, and c), in which (η_{sa}) decreases gradually with increase in (X/D) for all BR, while in models 1 and 3, (η_{sa}) decreases and then increases. From these figures, it can be seen that any model from these models has an advantage and disadvantage. So are can notice that model 2 gave better values of film cooling effectiveness than that of the other models near the hole exit for all BR. In the downstream region at (BR=0.5), model 3 gave higher value of (η_{sa}) than that of the other models, but for cases (BR=1 and 1.5), model 1 gave better performance for approximately ($X/D \geq 7$).

The overall average film cooling effectiveness for the entire selected area A_o (η_{av}) was calculated from the values of local film cooling effectiveness (η) for the entire pixels values included by the area (A_o). Figure 13 shows the effect of the blowing ratio on the averaged film cooling effectiveness (η_{av}) for the same cases. This Figure shows that model (1) gave higher value of (η_{av}) than other models, especially at high blowing ratio. It appears that the averaged film cooling effectiveness increases slightly with increasing BR, in models 1 and 2, while it decreases with increasing (BR) in model 3.

The average of the local heat transfer coefficient ratios (h / h_o), in which (h and h_o) represent the heat transfer coefficient on the plate surface with and without film cooling respectively are presented in Figure 14.This figure shows that model 1 gaves high (h/ho) with respect to the other two models at high blowing ratio.

In the practical application, turbine designers are concerned with the reduction of heat load to the film protected surface. The heat load can be presented by combining film cooling effectiveness (η) and the heat transfer coefficient ratio (h/h_o), according to equation (7), therefore the ratio (q/q_o) can be calculated. (q/q_o) represent the reduction in heat flux at the tested surface with the presence of coolant air. If the values of these ratios are less than 1, then the film coolant is beneficial according to **Lu et al. [5]**, while if the values are greater than 1, therefore effect of the film coolant is poor. Figure 15 represents the effect of blowing ratio on the overall heat flux ratios (q/q_o). It appears that the BR effect dominates the holes direction effects.

5- Conclusions

The present work has reached to the following conclusions:

1- For low blowing ratio, the film cooling effectiveness is constructed at the holes exit region, while at high blowing ratio, the coolant jets developed downstream give better film cooling effectiveness. On the other hand, model 3 arrangement (staggered rows, both inclination angles in the stream line direction) show an odd behavior.
2- Numerical prediction of the flow field structure for holes arrangement shows that the vortices (counter pair kidney vortex and horseshoe vortex) both have major effects on cooling performance.
3- The reverse flow from backward injection hole creates pair of vortex similar to the kidney vortex created from forward injection hole, but in a plane parallel to the main stream.
4- Near the exit holes area, model 2 (opposite direction rows hole) shows uniform heat protection from the hot gas streams.

Nomenclatures

A_o selected area (m^2).
BR blowing ratio
CFD Computational Fluid Dynamic
CVP Counter rotating vortex pair
$(CVP)_P$ Counter rotating vortex pair in parallel plan to main stream
D film hole diameter (m).
h heat transfer coefficient with coolant injection (W/m^2·K).
h_o heat transfer coefficient without coolant injection (W/m^2·K).
K thermal conductivity of test surface (W/m^2·K).
S Span wise hole spacing (m).
T time when the IR image was captured ($^\circ$C).
T_c coolant air temperature ($^\circ$C).
T_f film temperature ($^\circ$C).
T_i initial temperature ($^\circ$C).
T_m mainstream temperature ($^\circ$C).
T_w wall temperature ($^\circ$C).
U_c coolant air velocity (m/s).
U_m mainstream air velocity (m/s).
X Stream wise distance along the test surface (hole pitch) (m).
η film effectiveness.
η_{sa} spanwise average film cooling effectiveness.
η_{av} average film cooling effectiveness.
$\emptyset$ overall cooling effectiveness.
α thermal diffusivity.
γ orientation angle (Degree).
θ inclination angle (Degree).

References

[1]Han, J.C. andEkkad, S.V., " Recent Development in Turbine Blade Film Cooling", International Journal of Rotating Machinery, Malaysia, Vol. 7, No. 1, 2001, pp. 21-40.
[2] Ahn, J., Jung, I.S., and Lee, J.S., "Film cooling from two rows of holes with opposite behavior and adiabatic film cooling effectiveness", International Journal of Heat and Fluid Flow, Vol. 24, 2003, pp. 91-99.
[3] Dhungel, A., Phillips, A., Ekkad, S.V., and Heidmann, J.D., 2007, "Experimental Investigation of a Novel Anti-Vortex Film Cooling Hole Design", ASME IGTI Turbo Expo, Montreal, Paper GT 2007-27419.
[4] Lu, Y.,Dhungel, A.,Ekkad, S.V., and Bunker, R.S., 2007, "Effect of Trench Width and Depth on Film Cooling from Cylindrical Holes Embedded in Trenches", ASME Paper GT 2007-27388.
[5] Lu, Y., Dhungel, A., Ekkad, S.V., and Bunker, R.S., 2007, "Film Cooling Measurements for Cratered Cylindrical Inclined Holes", ASME Paper GT 2007-27386.
[6] Dia, P. and Lin, F., 2011,"Numerical study on film cooling effectiveness from shaped and crescent holes", Heat Mass Transfer, Vol. 47, PP. 147-154.
[7] Lee, K.D. and Kim, K.Y., 2011,"Surrogate based optimization of a laidback fan-shaped hole for film-cooling", International Journal of Heat and Mass Transfer, Republic of Korea, Vol. 32, PP. 226-238.
[8] Alwan, M. Sh., 2012," Experimental and Numerical Investigation of Film Cooling Thermal Performance for Staggered Rows of Circular Jet" PhD thesis, Mechanical Engineering Department , University of Technology.

[9] Holman, J.P. and Bhattacharyya, S., "Heat Transfer", Ninth Edition, New Delhi, McGraw-Hill, 2008.
[10] Ekkad, S.V., Ou, S., and Rivir, R.V., "A Transient Infrared Thermography Method for Simultaneous Film Cooling Effectiveness and Heat Transfer Coefficient Measurements from a single test", GT 2004-54236, Proceedings of ASME Turbo Expo 2004, Vienna, Austria.
[11] Ekkad, S.V., and Zapata, D., "Heat transfer coefficients Over a Flat Surface with Air and CO2 Injection Through Compound Angle Holes Using a Transient Liquid Crystal Image Method", ASME Journal of Turbomachinery Vol. 119, No. 3, 1997, pp. 580-586.
[12] Albert, J.E., Cunha, F. and Bogard, D.G., 2004, "Adiabatic and Overall Effectiveness for a Film Cooling Blade", ASME Paper GT2004-53998.
[13] Kline, S.J. and McClintock, F.A., 1953, "Describing uncertainties in single sample experimental", Mechanical Engineering, Vol. 75, pp. 3-8.
[14] Versteeg, H.K. and Malalasekera, W., 1996, "An introduction to computational fluid dynamics the finite volume method", Longman Group, London.
[15] Ozturk E., 2004, "CFD analysis of heat sinks for CPU cooling with FLUENT", MSc thesis, graduate school of natural and applied sciences, Middle East Technical University.
[16] Jones, D.A. and Clarke, D.B., 2005, "Simulation of a wind-body junction experiment using the fluent code", DSTD-TR-1731, Australia.

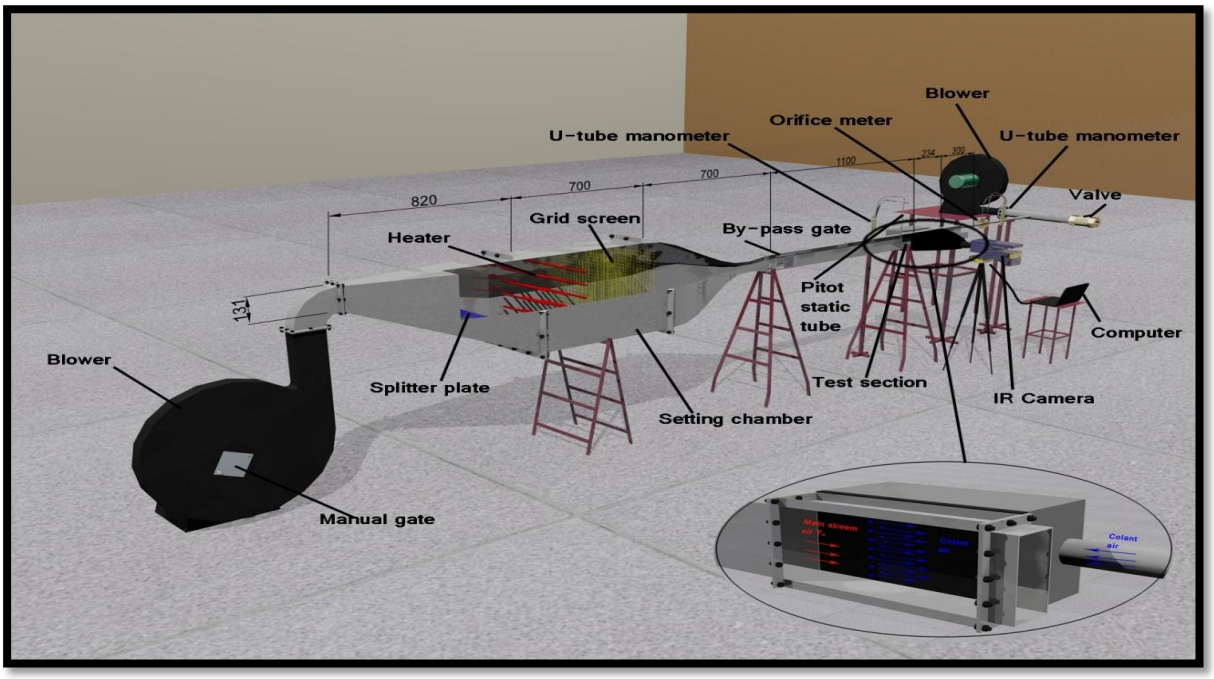

Figure 1 Schematic of the test rig

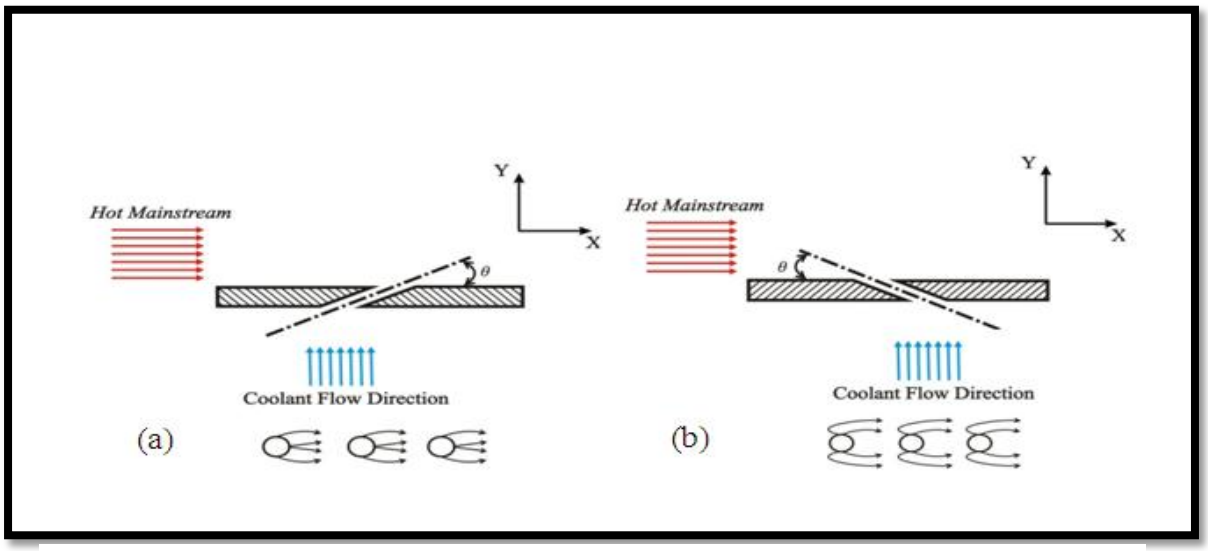

Figure (2) Illustrate diagram of the inclination and orientation angle : (a) $\theta = 30^{\circ}$ and $\gamma = o^{\circ}$, (b) $\theta = 30^{\circ}$ and $\gamma = 180^{\circ}$

Table (1) illustrated geometry for the three models.

Model Number	Upstream Row		Downstream Row		Shape
	$\boldsymbol{\theta}$	$\boldsymbol{\gamma}$	$\boldsymbol{\theta}$	$\boldsymbol{\gamma}$	
Model 1 Stagger	30° Acute jet angle	180°	30° Acute jet angle	0°	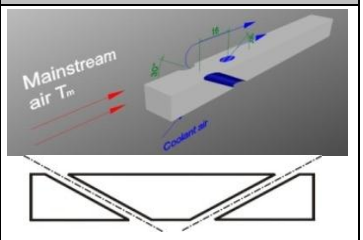
Model 2 Stagger	30° Acute jet angle	180°	150° Obtuse jet angle	180°	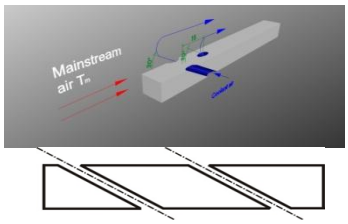
Model3 Stagger	150° Obtuse jet angle	0°	30° Acute jet angle	0°	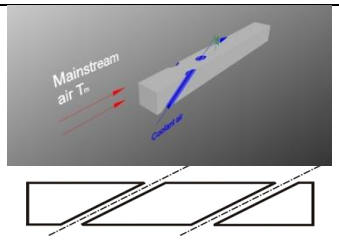

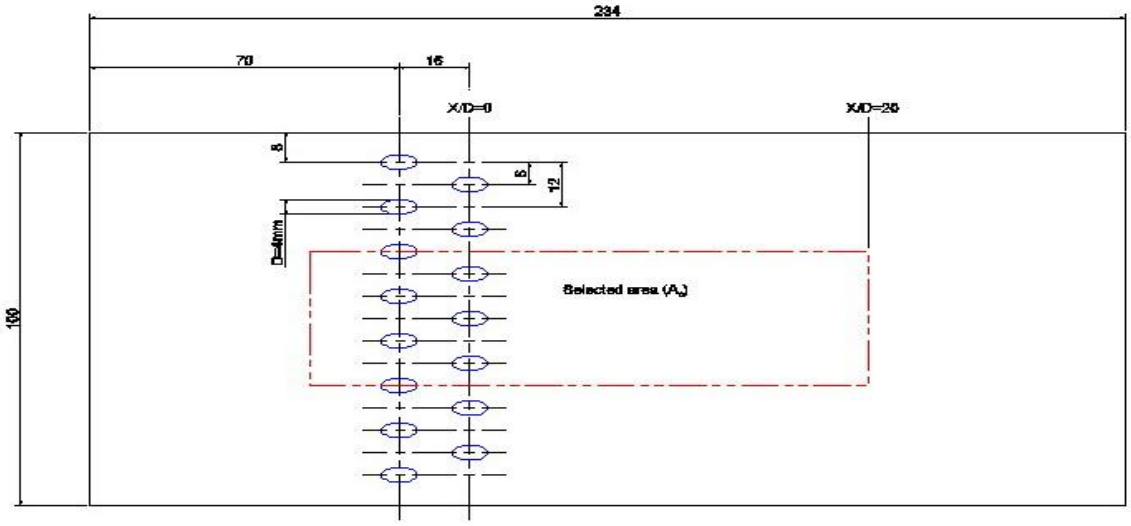

Figure 3 the middle selected area of the test section (A_o)

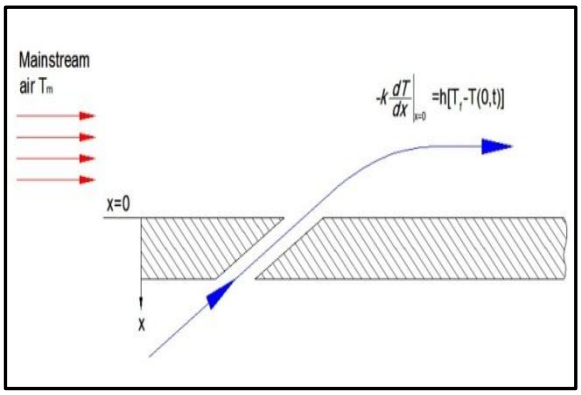

Figure 4 Flow over a flat plate

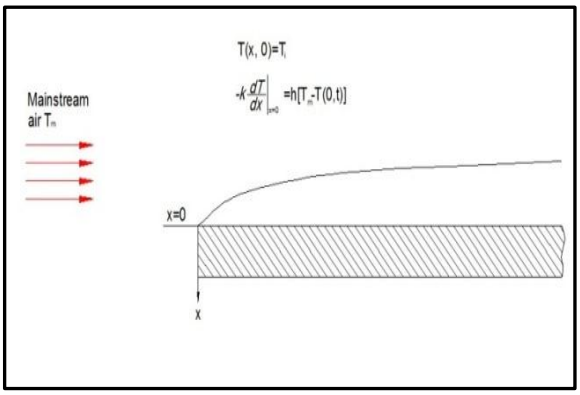

Figure 5 Film cooling over a flat plate

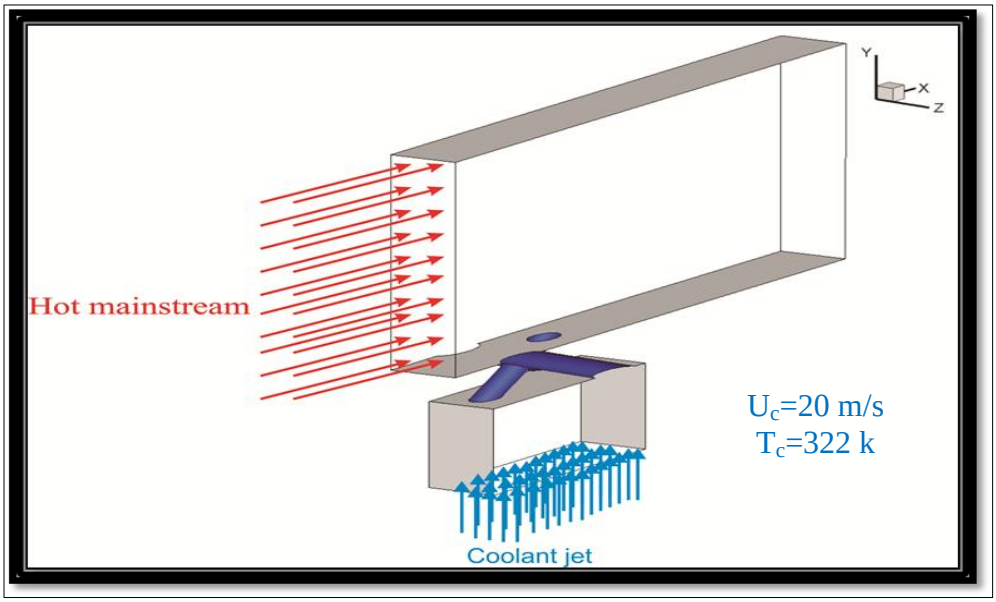

Figure 6 Schematic of geometry shape

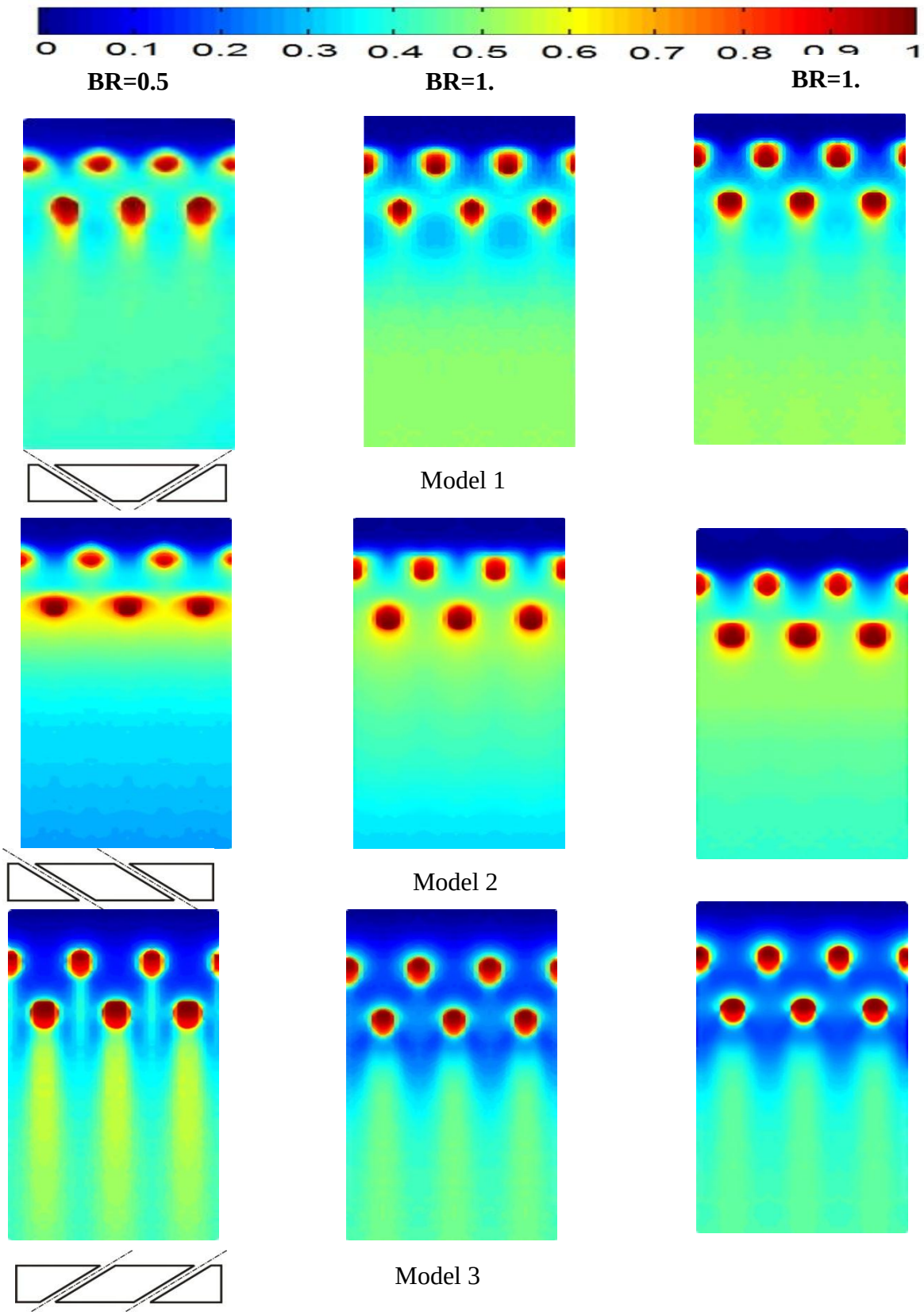

Figure 7 Contours of film cooling effectiveness for models (1, 2 and 3) at different blowing. (Exp.)

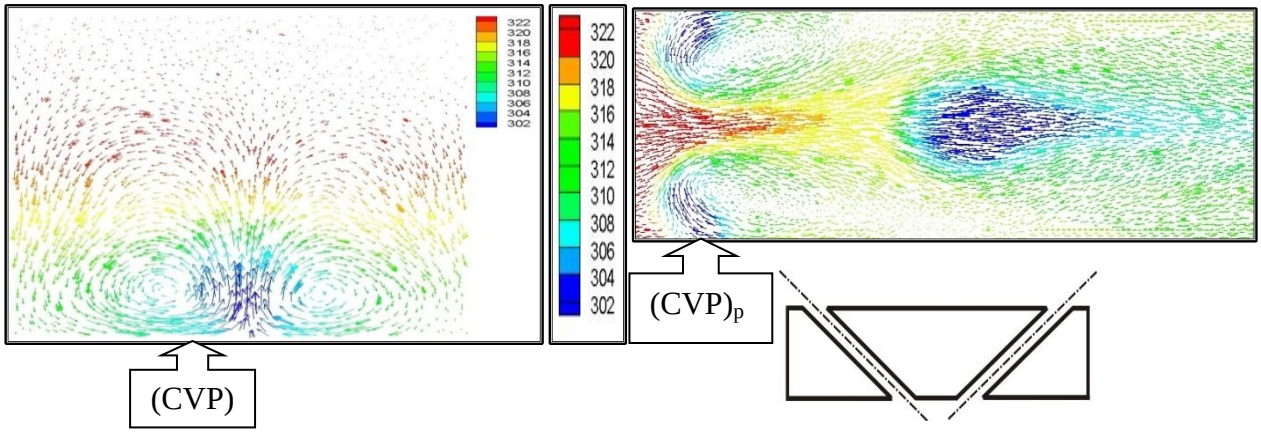

Figure 8 (a) Flow vectors colored by temperature at plane (X/D=4) for model 1at BR=١.5 (CFD)
(b) Flow vectors colored by temperature at plane parallel to test surface (Y=1mm) for model 1 at BR=1.5. (CFD)

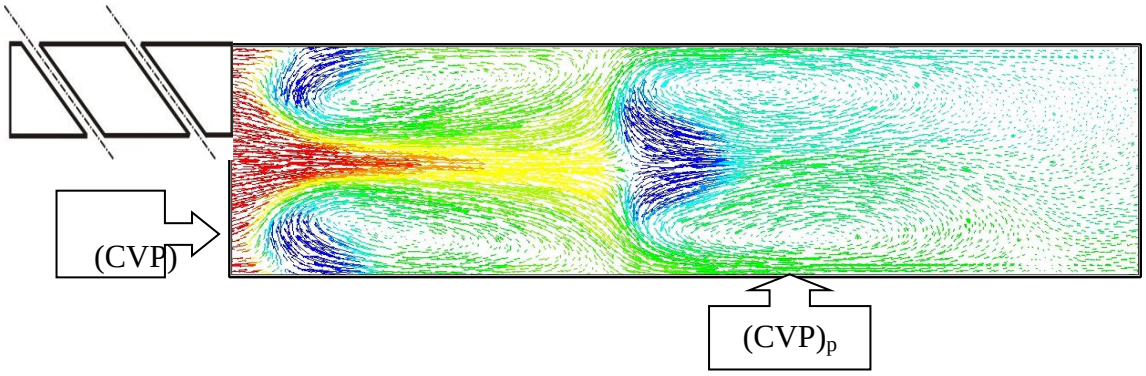

Figure 9 Flow vectors colored by temperature at plane parallel to test surface for model 2 at BR=1.5. (CFD)

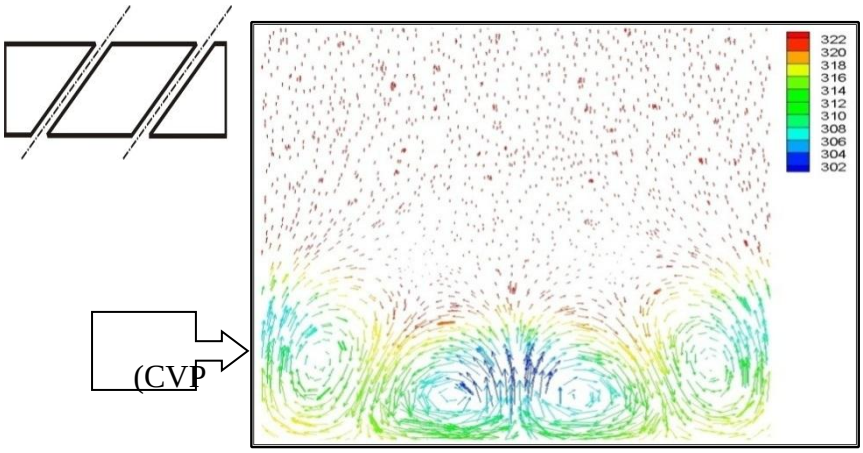

Figure 10 Flow vectors colored by temperature at plane (X/D=4) for model 3at BR=1.5 (CFD)

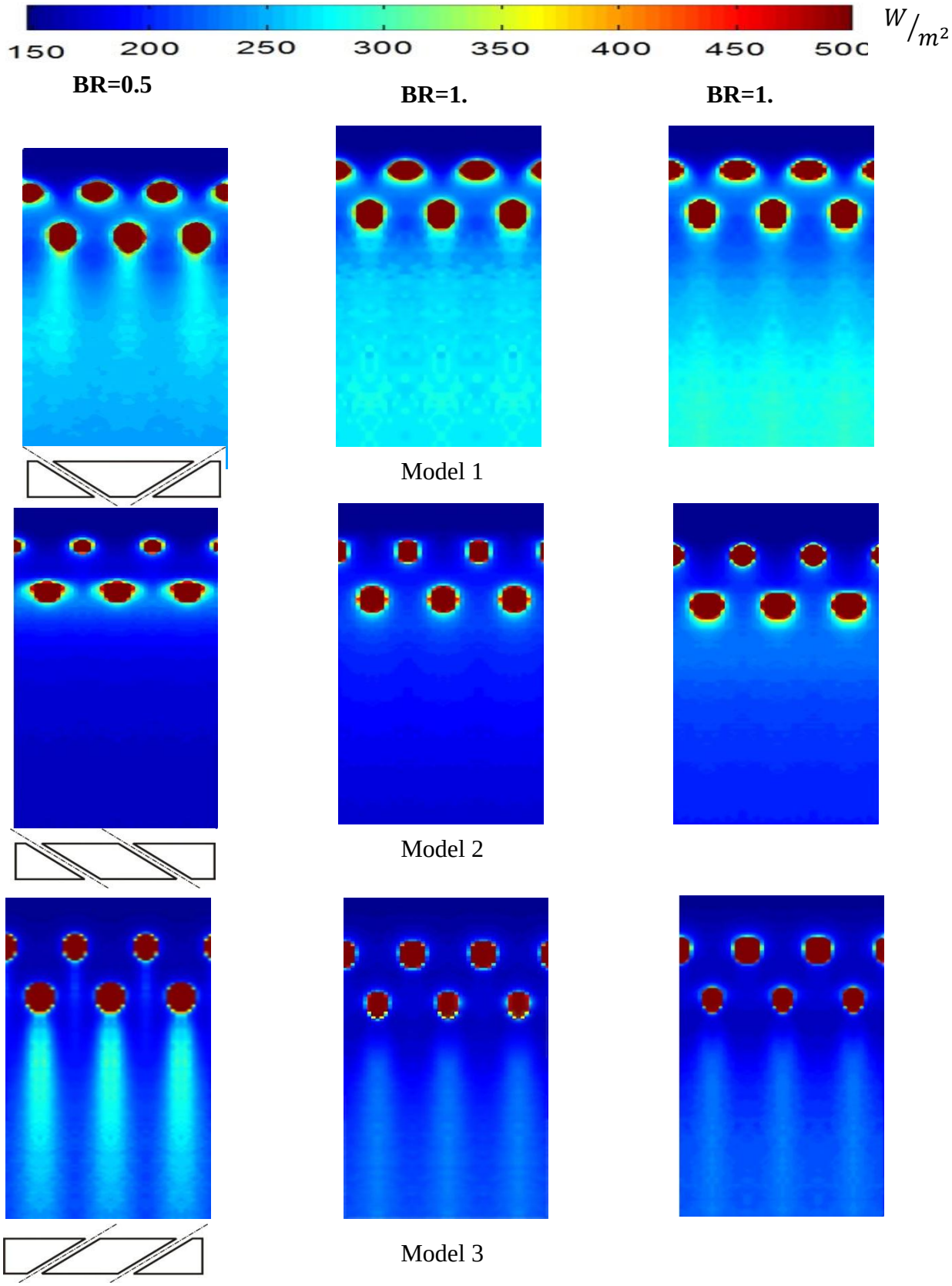

Figure 11 Contours of heat transfer coefficients ($W/m^2.K$) for models (1, 2 and 3) at different blowing TYYGB KLOratio. (Exp.)

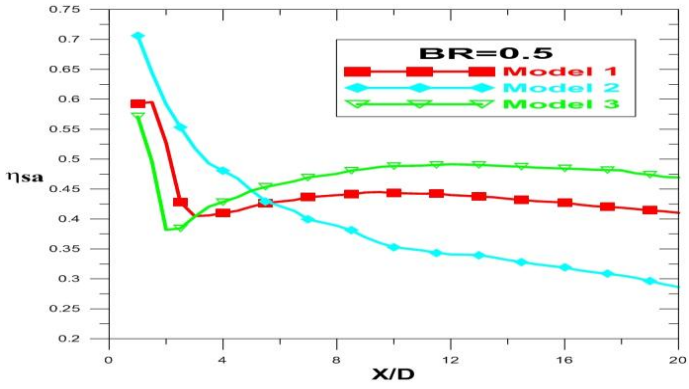

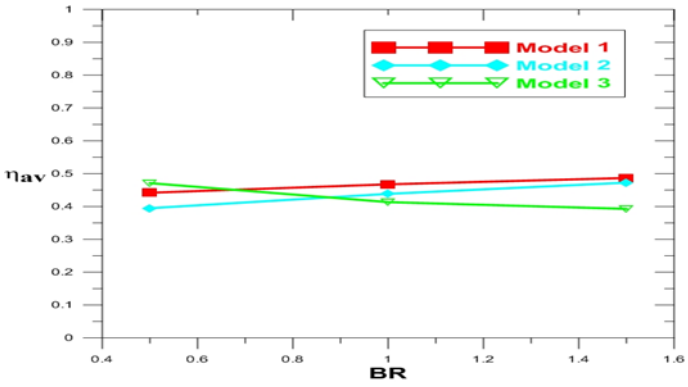

Figure 13 Effect of blowing ratios on averaged film cooling effectiveness for models (1, 2 and 3). (Exp.)

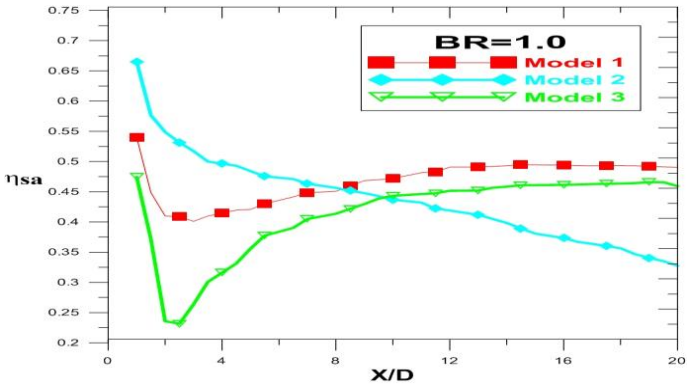

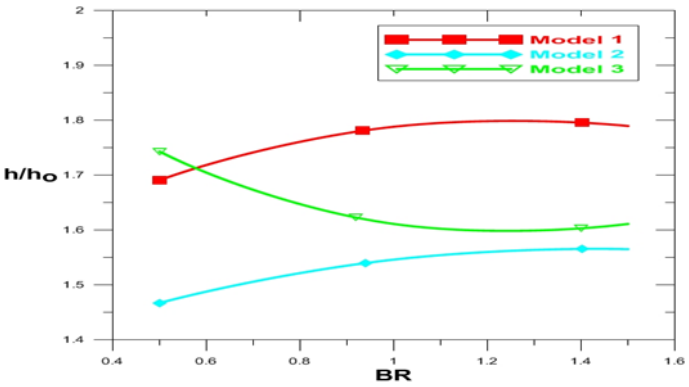

Figure 14 Effect of blowing ratios on averaged heat transfer coefficient ratios for models (1, 2 and 3). (Exp.)

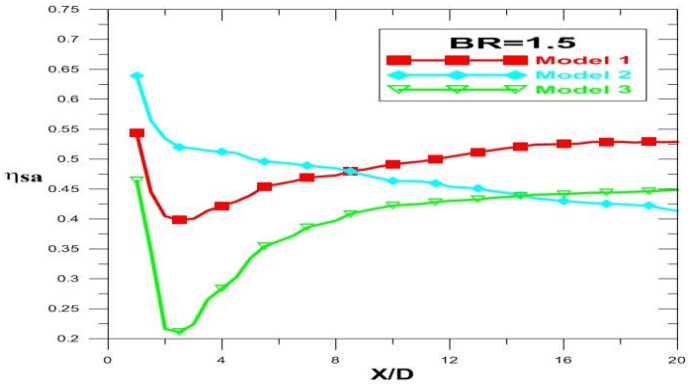

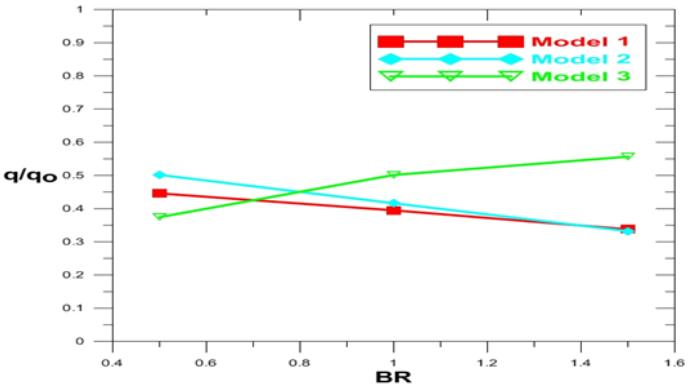

Figure 12 Effect of hole arrangement on span wise averaged film cooling effectiveness for models (1, 2 and 3) at:(a) BR=0.5, (b) BR=1.0, (c) BR=1.5. (Exp.)

Figure 15 Effect of blowing ratios on overall averaged heat flux ratios for models (1, 2 and 3). (Exp.)

SIMULATION OF LAMINAR FORCED CONVECTION HEAT TRANSFER AND FLUID FLOW OVER A BACKWARD FACING STEP WITH OBSTACLE USING (SIO_2) NANOPARTICLES

Mohammed Saad Kamel **Ahmed Khafeef Obaid Albdoor**

Southern Technical University/ Al-Nassiriyah Technical Institute Department of Mechanical Techniques

Mr.mohd1986@yahoo.com **Ahmedalbadry82@yahoo.com**

***Abstract*:** Simulation of Heat transfer and laminar Sio_2/water and Sio_2/oil-engine flow over backward facing step with and without obstacle numerically studied in this paper. The finite volume method adopted to solve continuity, momentum and energy equations in two dimensions. The aspect ratio of triangular obstacle *w/e* = 0.5 presented. The step height and expansion ratio of channel were 4.8_{mm} and 2 respectively, the range of Reynolds number varied from 100 to 250, constant heat flux subjected on downstream of wall was $2000W/m^2$.Two types of base fluid used in this simulation the water and oil-engine with constant properties at T = 300K°, The Sio_2 nanoparticles used with nanoparticles diameter 30*nm* and volume friction 4%. The average nusselt number noticed increase with increase Reynolds number with obstacle for two basefluid and also noticed that the nanofluid of Sio_2-oil engine has higher nusselt number compared with other nonofluid. The result shows increase of local nusselt number for backward facing step with obstacle in compared to those without obstacle. The maximum enhancement of heat transfer observed at obstacle due to increase recirculation flow after the obstacle. Streamline showing the increase of recirculation region with used obstacle in compared without obstacle and highest recirculation region observed at obstacle.

Keywords: laminar flow, backward facing step, Sio_2 nanoparticles, forced convection.

المستخلص : محاكاة انتقال الحرارة و الجريان الطباقي للماء مع Sio2 و زيت المحرك مع SiO_2 فوق عتبة موجهة للخلف مع و بدون عائق تم دراستها عددياً في هذه الدراسة . تم اعتماد طريقة الحجوم المحددة لحل معادلات الاستمرارية ، الزخم و الطاقة في بعدين . اعتمدت نسبة العرض الى الارتفاع للعائق المثلث (w/e = 0.5) . وكان ارتفاع العتبة و نسبة توسع القناة mm 4.8 و 2 على التوالي . مدى اعداد رينولدز اختلف من 250 الى 100 . فيض حراري ثابت عرض له الجريان بعد الجدار وكانت قيمته $2000W/m^2$ في هذه . نوعين من الموائع الأساسية استخدمت المحاكاة الماء و زيت المحرك بخصائص ثابتة عند درجة حرارة K ° T = 300 . جزيئات Sio2 استخدمت بقطر جزيئات نانوية nm 30% . عدد نسلت المعدل لوحظ انه يزداد مع زيادة عدد رينولدز بوجود العائق 4 و حجم احتكاك مع زيت المحرك يمتلك اعلى قيم لأعداد نسلت SiO_2 للمائعين الأساسيين الأثنين و يلاحظ أيضاً ان المائع النانوي بالمقارنة مع المائع النانوي الاخر . النتائج بينت زيادة في قيم اعداد نسلت الموقعية للعتبة الموجهة للخلف بوجود العائق بالمقارنة معها بدون عائق . اقصى تحسين في انتقال الحرارة لوحظ في العقبة بسبب زيادة إعادة تدوير الجريان بعد العائق . خطوط الانسياب بينت زيادة في منطقة اعادة التدوير باستخدام العائق بالمقارنة مع بدون العائق وان اكبر منطقة اعادة تدوير لوحظت في العائق .

1- Introduction:

Flow over a backward facing step generates recirculation zone and forms vortices due to the separation flow obtained from the adverse pressure gradients in fluid flow. Improve thermal performance in different engineering application become main goal in recent presented researches as the fluid flow over backward facing step is common geometry used in cooling and heating systems such as heat exchangers, chemical process, power plants, and nuclear

reactor due to generate separation and reattachment region. In addition, used obstacle in flow passage leads to increase of static pressure and then enhance of heat transfer [1]. Many researcher have been studied an experimental and numerical for analysis heat transfer and fluid flow over backward facing step. Armaly et al. [2] have experimental and numerical studied of laminar, transition, and turbulent air flow over backward-facing step. They found that the separation length increase with increase of the Reynolds number for Re< 1200 while reduction at Re between 1200 to 5550. De Zilwa et al. [3] developed new calculation method for study laminar and turbulent flows through plane sudden expansions. The calculations of laminar range found that increase thickness of the separating up to reach bigger separation region and used k- ε models for turbulent range as obtained good agreement compared to experimental results. Effect of step height on non-Newtonian liquids flow through sudden expansion investigated by Pak et al. [4] where found that decrease of length reattachment at non-Newtonian liquid compared to water for same boundary condition of flow. Khanafer et al. [5] performed numerical study of heat transfer to laminar mixed convection of pulsatile flow over a backward-facing step by using finite element method. They showed that improve of the heat transfer rate with increased of Reynolds number but the thickness of the thermal boundary layer reduced. two-phase flow over backward-facing step with low and high Reynolds number numerically studied by Yu et al. [6] in 2D and 3D dimension. LES was applied and found good agreement between 2D-3D numerical result with experimental result in profile of velocity and temperature distribution. Heat transfer to laminar fluid flow between parallel plates through baffles was numerically studied by Kelkar and Patankar [7]. The study described flow by strong deformations and large recirculation regions and found increase of Nusselt number and friction coefficient with increased Reynolds number.

More recently, the majority of studies have been utilizing nanofluid because of its higher thermal conductivity compared to normal fluid [8]. Abu Nada [9] is a pioneer in research on laminar nanofluid flow over a backward-facing step with Cu, Ag, Al_2O_3, CuO, and TiO_2 nanofluid, volume fractions between 0.05 and 0.2 and Reynolds numbers ranging from 200 to 600. An investigation of findings signifies that the Nusselt number increased with the volume fraction and Reynolds number. Later, Kherbeet et al. [10] presented a numerical investigation of heat transfer and laminar nanofluid flow over a micro-scale backward-facing step. The Reynolds numbers ranged from 0.01 to 0.5, nanoparticle types comprised Al2O3, CuO, SiO_2, and ZnO, and the expansion ratio was 2. An increasing Reynolds number and volume fraction seemed to lead to an increasing Nusselt number; the highest Nusselt number value was obtained with SiO2. Additional last investigations concern nanofluid flow over a backward-facing step for the laminar range [11–12], but such work with respect to the turbulent regime, in particular, is still not entirely understood. Due to the Cu has higher thermal conductivity and many experimental investigations done with good improvement in thermal performance then used in this simulation.

The aim of the present work is to investigate the heat transfer and laminar fluid flow over backward facing step with and without obstacle by using two types of basefluid with Sio2 nanoparticles. The numerical data for used obstacle in flow passage with backward facing step will be more helpful to design thermal channel with higher performance. In this investigation, Finite Volume Method in commercial program FLUENT 6.3.26 is employed.

2- Numerical model

2.1 Description of geometry

In this simulation, the geometry and flow domain is shown in Fig. 1 where the dimension of geometry was according to Al-Aswadi et al. [12]. Backward-facing step of duct with and without triangular obstacle are adopted. The height of obstacle is 4mm and 2mm width fixed at 200mm from the step with expansion ratio 2 at Reynolds numbers of 100, 175, and 250.

The total length of duct is 1050mm consist of 50mm upstream length and 1000mm downstream length and inlet height of duct is 4.8mm and exit height is 9.6mm. Constant heat flux (2000 W/m^2) is subjected on downward of duct while insulated other parts of duct. Two working fluids used as a basefluid pure water and oil-engine and then added Sio_2 nanoparticles for them at constant volume friction and constant diameter of nanoparticles (4% and 30nm respectively) to study the enhancement of heat transfer with and without obstacle.

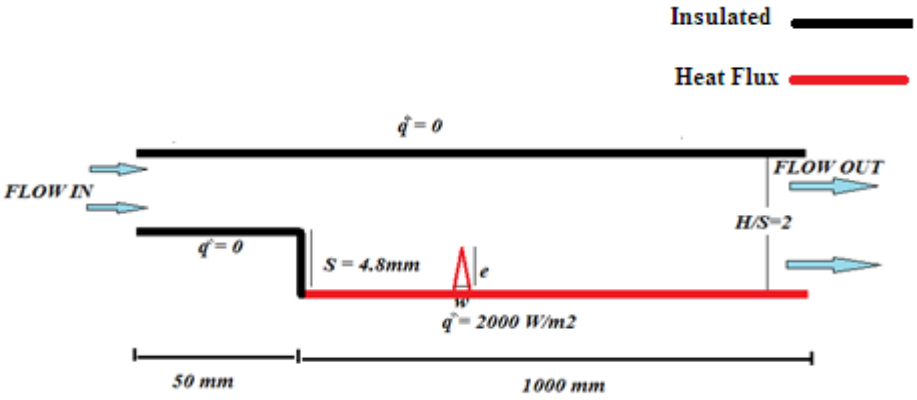

Figure 1. Geometry domain and boundary condition

2.2 Governing Equations:

Continuity, momentum (X, Y) and energy equations with assumption laminar, steady state, incompressible, and two dimensional are employed in this simulation and can be written as (1)-(4).

$$\frac{\partial u}{\partial x}+\frac{\partial v}{\partial y}=0 \qquad \text{.....(1)}$$

$$u\frac{\partial u}{\partial x}+v\frac{\partial u}{\partial y}=-\frac{1}{\rho}\frac{\partial p}{\partial x}+\nu\left(\frac{\partial^2 u}{\partial x^2}+\frac{\partial^2 u}{\partial y^2}\right) \qquad \text{.....(2)}$$

$$u\frac{\partial v}{\partial x}+v\frac{\partial v}{\partial y}=-\frac{1}{\rho}\frac{\partial p}{\partial y}+\nu\left(\frac{\partial^2 v}{\partial x^2}+\frac{\partial^2 v}{\partial y^2}\right) \qquad \text{.....(3)}$$

$$u\frac{\partial T}{\partial x}+v\frac{\partial T}{\partial y}=-\frac{1}{\rho}\frac{\partial p}{\partial y}+\alpha\left(\frac{\partial^2 T}{\partial x^2}+\frac{\partial^2 T}{\partial y^2}\right) \qquad \text{.....(4)}$$

Where u and v represent velocities in x, y direction respectively, ρ and α define density and thermal expansion, respectively.

The Reynolds number is computed based on inlet channel height (H).

$$Re=\frac{\rho u H}{\mu} \qquad \text{.....(5)}$$

$$Nu_{av}=\frac{1}{L}\int_0^L Nu_L\ dL \qquad \text{.....(6)}$$

Where (L) is the length of the heated downstream wall.

2.3 Boundary conditions

The boundary conditions for this simulation are:

- At the inlet Chanel the fluid is assumed to enter with a uniform horizontal velocity U∞ and temperature (T∞) U=U∞, T=T∞=300K, V=0;
- At the outlet Chanel: P=0,
- Insulated top wall of the of duct. The mathematical form of this condition: $\frac{\partial U}{\partial y}$ =0, V=0, $q^{"}$= 0
- For the downward of duct Constant heat flux $q^{"}$ (2000 W/m^2) is subjected while insulated other parts of duct

2.4 Numerical procedure and Data Validation

FLUENT 6.3.26 software with computational fluid dynamics (CFD) were conducted in numerical simulations. The procedure for generate geometry and meshing process was performed with Gambit 2.3.16 software. Viscous laminar flow model with energy dialog box was selected to solve continuity and X,Y momentum equations as well as energy equation. In computational fluid dynamics (CFD), SIMPLE algorithm is a commonly used in numerical procedure to solve the Navier-Stokes equations therefore employed to link the velocity and pressure fields. The residual of solution was smaller than (10^{-4}) for continuity equation, (10^{-5}) for momentum equations and (10^{-6}) for energy equation. In order to increase accuracy of solution, the density of mesh at backward and obstacle was more highly than other parts. The computational conditions and thermo-physical properties used in the numerical simulation are shown in Table 1. Five size of grid was adopted at Re =175 and airflow as a working fluid. Where the grid densities was (19558, 40864, 70752, 116506 and 228700) triangular cells. The grid independent selected (116506) cells among the others due to the difference in nusselt number was less than 3% compared to the grids as shown in Figure. 2. For purpose of validations used boundary conditions as reported by Al-Aswadi et al. [12] and then obtained results with acceptable agreement as shown in Figure. 3.

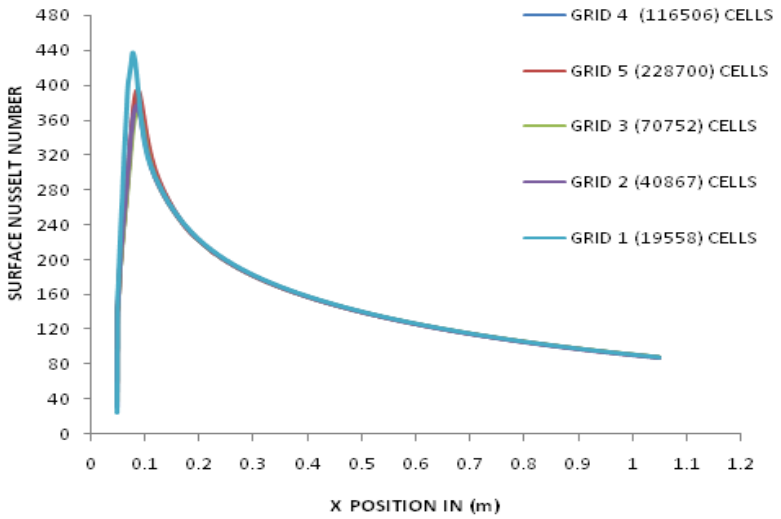

Figure 2. Grid independence test results for the Nusselt number

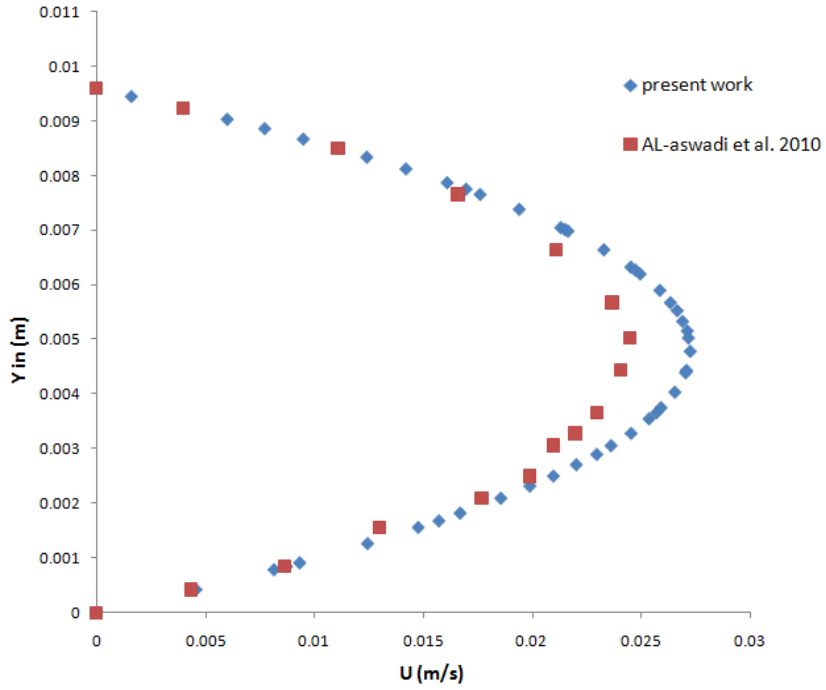

Figure 3. Comparison velocity profile with Al-Aswadi et al. [12].

Table 1. The computational conditions and thermo-physical properties

COMPUTATIONAL CONDITIONS		***[13]**	***[14]**
Fluid	Water (basefluid)	Oil-engine (basefluid)	Sio_2 nanoparticles
Pressure velocity coupling scheme	SIMPLE	SIMPLE	SIMPLE
Density	998.2 kg/m^3	884.1 kg/m^3 *	2220 kg/m^3 *
Viscosity	0.001 (N.s/m^3)	0.486 (N.s/m^3) *	-
Thermal conductivity	0.6 (W/m.K)	0.145 (W/m.K) *	1.4 (W/m.K) *
Heat capacity	4182 (J/Kg.K)	1909 (J/Kg.K) *	745 (J/Kg.K) *
Viscous model	Laminar model	Laminar model	Laminar model
Reynolds number	100, 175 and 250	100, 175 and 250	100, 175 and 250
Thermal heat flux	2000 W/m^2	2000 W/m^2	2000 W/m^2

3- Thermo-physical properties of nanofluids:

The effective properties of nanofluid are defined as follow:

Density:

$$\rho_{nf} = \varphi\rho_p + (1-\varphi)\rho_{bf} \quad \text{.....(7)}$$

Heat capacity:

$$cp_{nf} = \frac{\varphi\rho_p cp_p + (1-\varphi)\rho_{bf} cp_{bf}}{\rho_{nf}} \quad \text{.....(8)}$$

The Eqs. (6) and (7) were introduced by [15].

The thermal conductivity:

$$\frac{K_{nf}}{K_{bf}} = \frac{K_p + (n-1)K_{bf} - (n-1)\varphi(K_{bf} - K_p)}{K_p + (n-1)K_{bf} + \varphi(K_{bf} - K_p)} \quad \text{.....(9)}$$

This was introduced by [16].

Where (n) is a shape factor and equal to (3) for spherical nanoparticles.
The viscosity:

The effective viscosity can be obtained by using the following mean empirical correlation [17].

$$\mu_{nf} = \mu_{bf} \frac{1}{(1-34.87(d_p/d_{bf})^{-0.3}\,\varphi^{1.03})} \quad \text{.....(10)}$$

Where: $d_{bf} = \left[\frac{6M}{N\pi\rho_{bf}}\right]^{1/3}$ .....(11)

Where: M is the molecular weight of basefluid, N is the Avogadro number = $6.022*10^{23}$ mol^{-1}, ρ_{bf} is the mass density of the basefluid calculated at temperature T_0=300 K. the table 1. Show the thermo-physical properties of nanoparticles and working fluids.

4- Results and discussion:

4.1 The effect of different base fluids

The effect of two types of base fluids on the Nusselt number versus the Reynolds number is presented in Fig.5. It can clearly be seen that Sio_2–oil engine has the highest value of Nusselt number while Sio_2–water has the lowest value of Nusselt number. This is because oil engine has the highest dynamic viscosity in nature compared to other base fluids and Sio_2 particles

are mixed properly in oil engine which contributes to increase the thermal transport capacity of the mixture which in turn increases the Nusselt number.

4.2 The effect of the Reynolds number

The effects of the Reynolds number on the local nusselt number for the laminar ranges with and without obstacle are presented in Figures. 4(A),(B) respectively. With the increase of Reynolds number, the nusselt number increased in the laminar ranges. Effect of Reynolds number on surface nusselt number with axial distance at case with and without obstacle is illustrated. Generally, increase of surface nusselt number found with increase Reynolds number for all cases which denote to enhancement of thermal performance.

4.3 Average Nusselt number

In Figure. 5 the variation of average Nusselt number with the Reynolds number at different nanofluid with and without obstacle can be seen. For all cases, the average Nusselt number augmented as the Reynolds number increased. The highest Nusselt number was obtained at 250 Reynolds number. The maximum ratio of enhancement heat transfer to nanofluid was about ٣٤% for Sio_2-oil engine with obstacle compared with Sio_2-water with obstacle due to increase of intensity convection of enhanced conductivity nanofluid.

4.4 Streamline of Velocity

Streamline of velocity for backward facing step with and without obstacle for both nanofluids at Reynolds number 250 are illustrated in Figure. 6. It can be seen that the recirculation region is clearly appeared at the inlet region of backward and after obstacle due to pressure gradient. Increase size of recirculation region found with increase Reynolds number as shown in Figure. 7. Where the largest region noticed at Reynolds number 250 with obstacle and Sio_2-oil engine compared with other cases.

4.5 pressure drop

The pressure drop variation with axial distance for different Reynolds numbers and Sio_2-water nanofluids is presented in Figures. 6 and 7. According to the results, the pressure drop intensified as the Reynolds number increased and nanofluid volume fraction. Generally, the highest pressure drop occurred at the downstream inlet region with obstacle due to recirculation flow which caused the improvement of heat transfer.

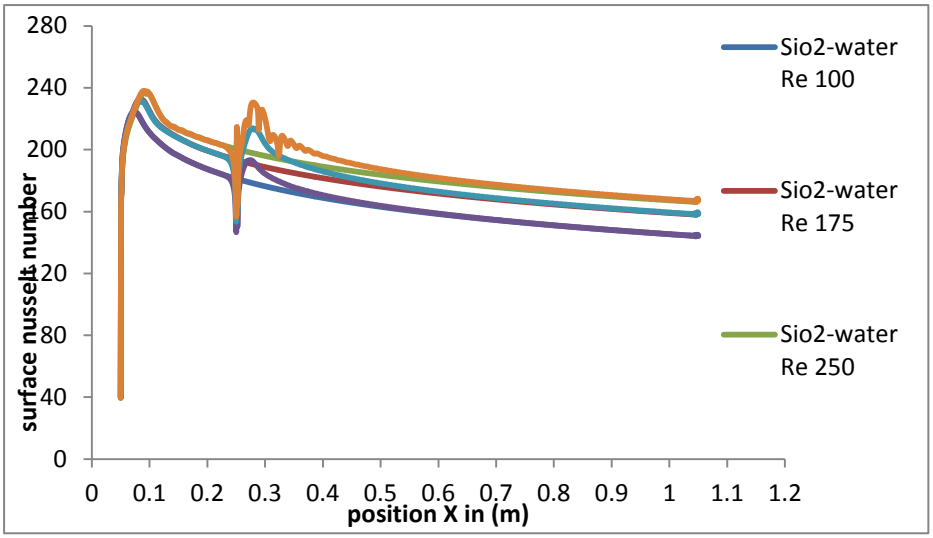

(A)

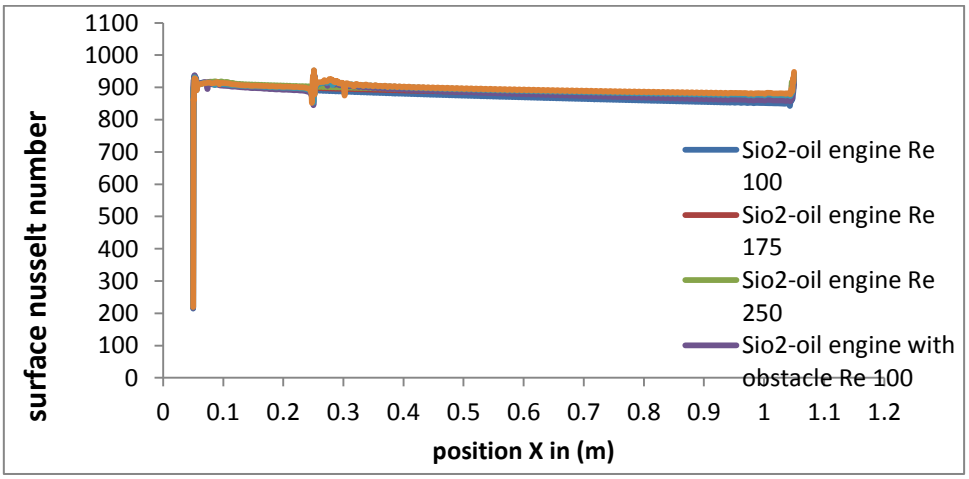

(B)

Figure 4. Surface nusselt number with x position at different Reynolds number (A) for Sio2-water with and without obstacle (B) for Sio2-oil engine with and without obstacle

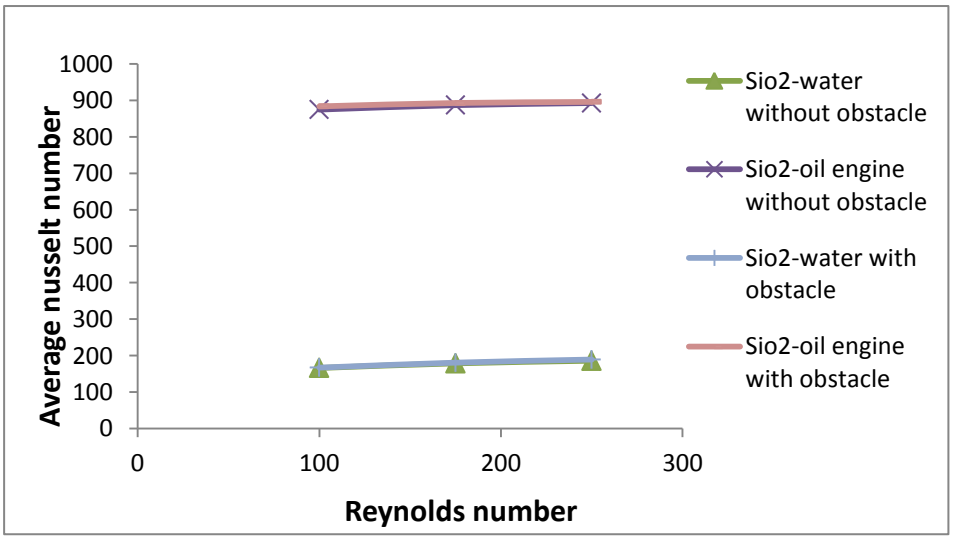

Figure 5. Average Nussult with Reynolds number

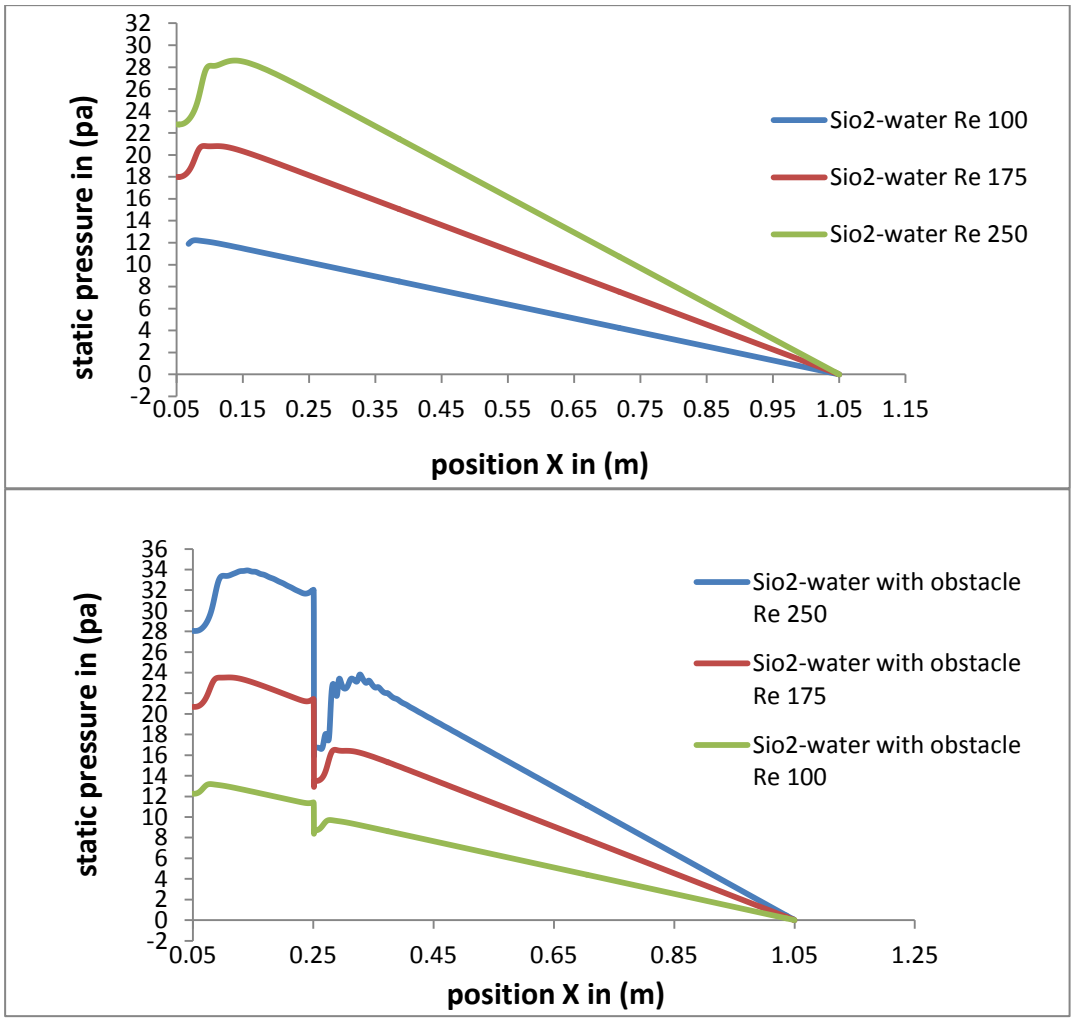

Figure 6. Statics pressure with different Reynolds number for Sio2-water with and without obstacle

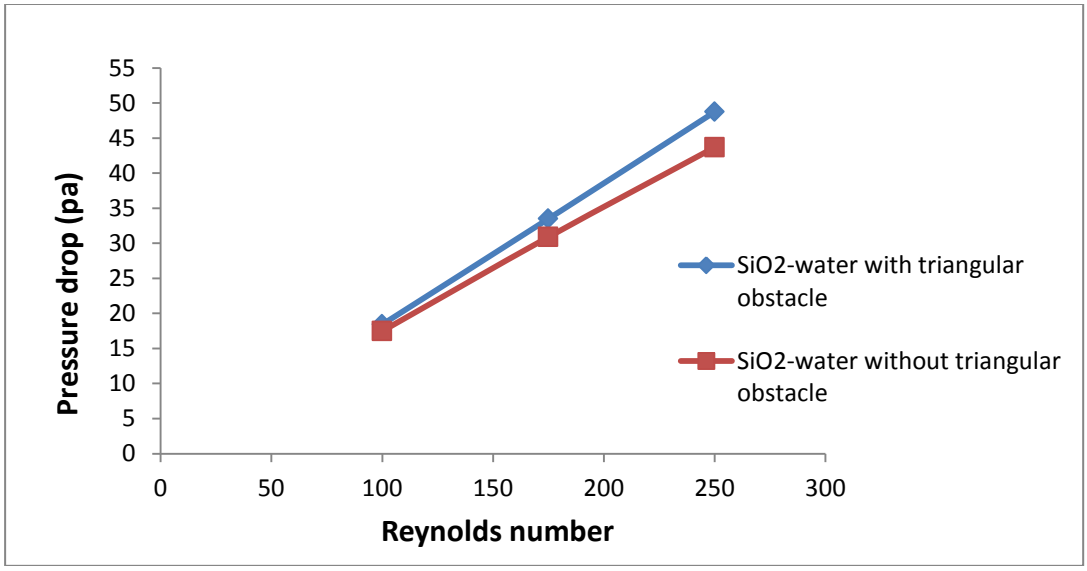

Figure 7. Pressure drop with different Reynolds number for Sio2-water with and without

obstacle

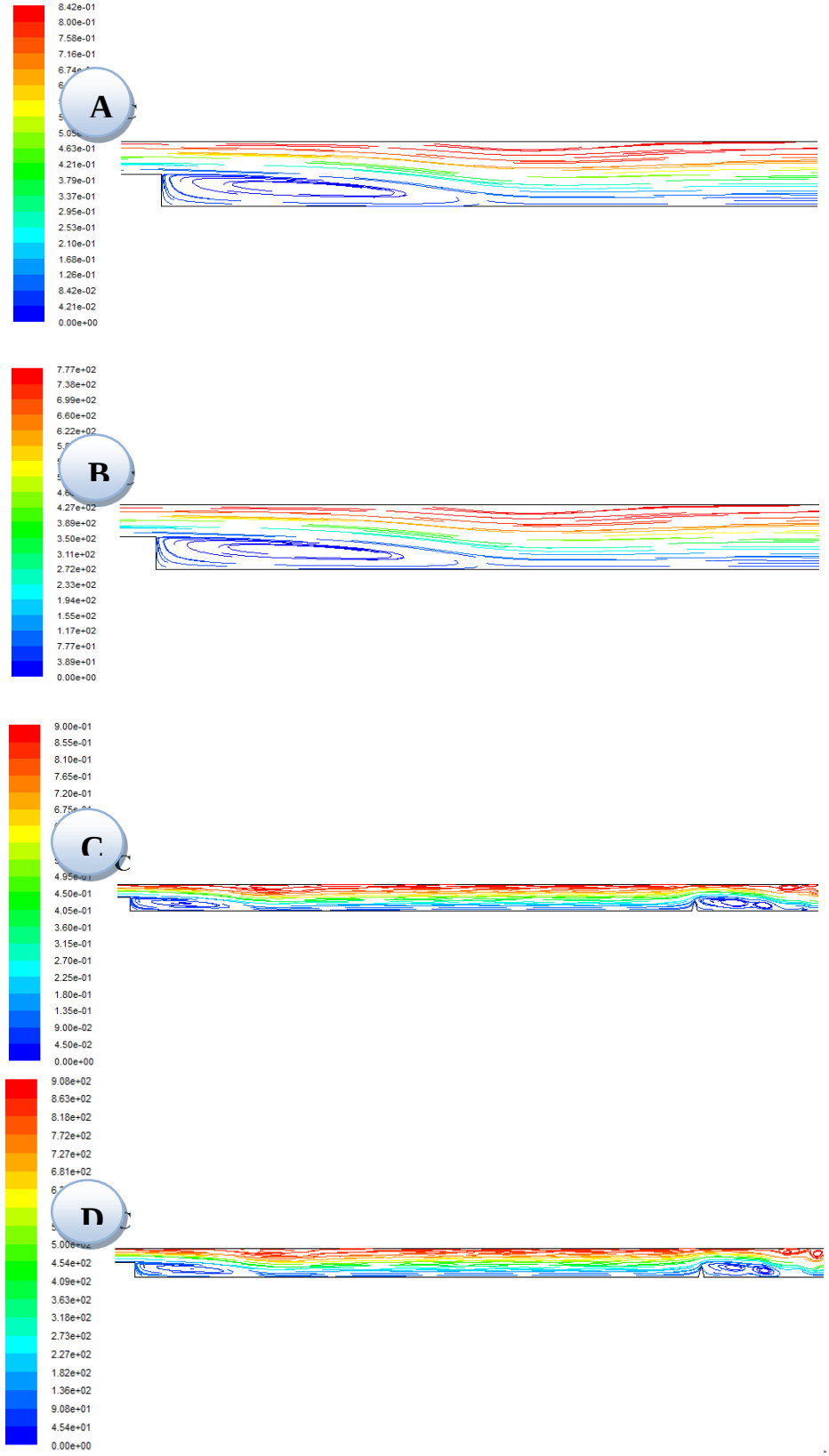

Figure 6. Velocity streamline at expansion ratio 2 without obstacle for (A) Sio2-water flow, (B) Sio2-oil engine flow (C) Sio2-water with obstacle , (D) Sio2-oil engine with obstacle at Re 250.

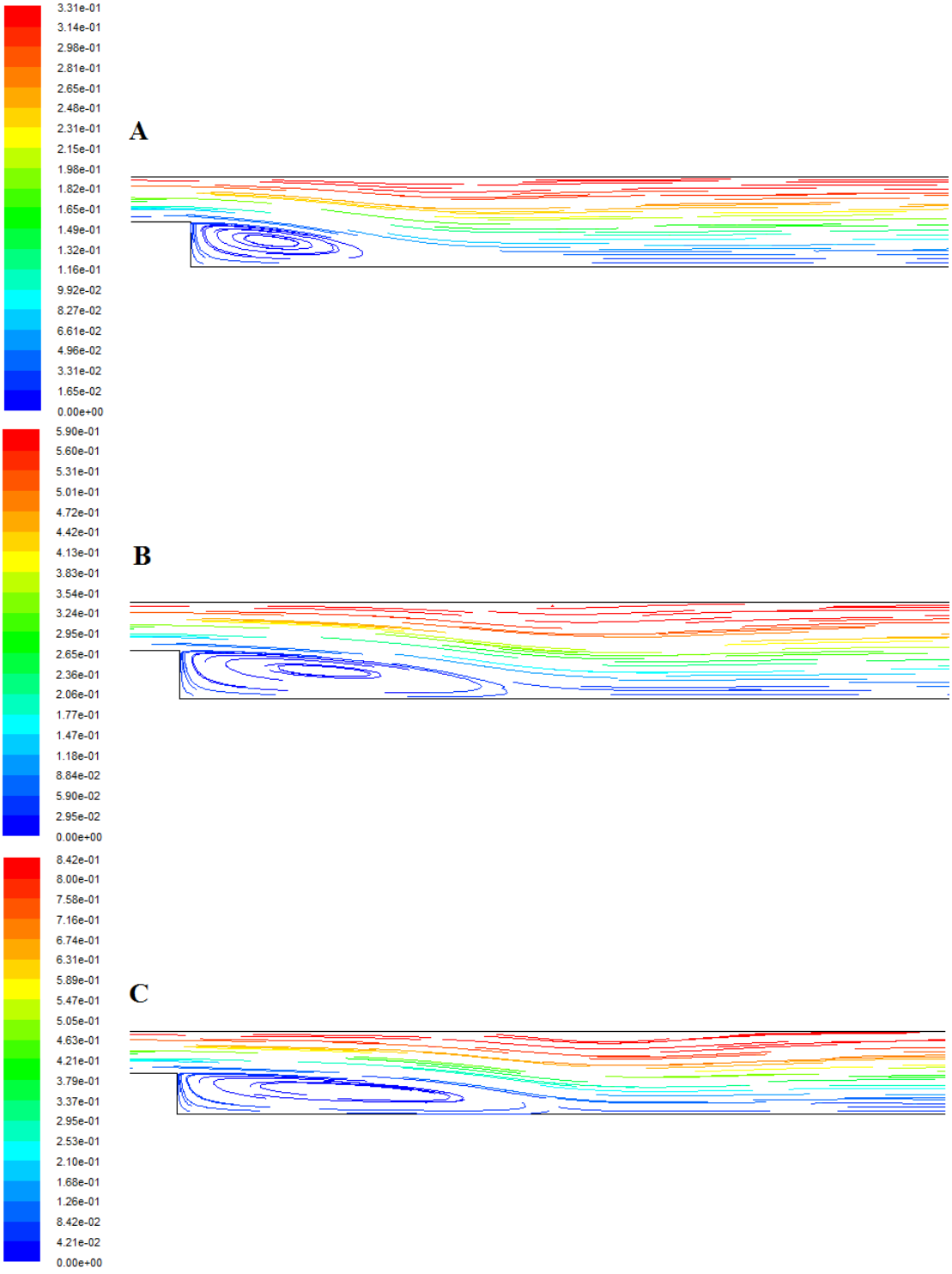

Figure 7. Velocity streamline at expansion ratio 2 without obstacle for Sio2-water
At Re A. 100 B. 175 C. 250

Nomenclature:

Cp	specific heat capacity (J kg^{-1} K^{-1})
Nu_L	surface Nusselt number
Nu_{av}	average Nusselt number
P	Pressure (Pa)
Pr	Prandtl number
q	heat flux (W m^{-2})
Re	Reynolds number
T	temperature (K)
u	velocity component (m s^{-1})
x, y	spatial coordination (m)
L	Length of the heated downstream wall (m)
S	Step height
H	Height of outlet channel (m)
h	Height of inlet channel (m)
e	Height of obstacle (m)
w	Width of obstacle (m)
M	molecular weight of basefluid
d_p	Particles diameter (nm)
d_{bf}	Basefluid diameter (nm)
N	Avogadro number

Greek symbols

K	thermal conductivity (W m^{-1} K^{-1})
μ	dynamic viscosity (Pa s)
ρ	density (kg m^{-3})
α	Thermal expansion
ρ_{bf}	Density of basefluid (kg m^{-3})
φ	Volume friction (%)

Subscripts

nf	nanofluid
p	Nano particles
bf	basefluid

References:

[1] Hussein Togun, Tuqa Abdulrazzaq, S. N. Kazi, A. Badarudin, M. K. A. Ariffin, M. N. M. Zubir "Numerical Study of Heat Transfer and Laminar Flow over a Backward Facing Step with and without Obstacle " "International Journal of Mechanical, Aerospace, Industrial and Mechatronics Engineering" Vol:8 No:2, 2014. **[2]** B.F. Armaly, F. Durst, J.C.F. Pereira, B. Schonung, "Experimental and theoretical investigation of backward-facing step flow," Journal of Fluid Mechanics, vol.127, pp. 473-496, 1983.

[3] De Zilwa, S .R N., Khezzar, L. K. and Whitelaw, J. H., "Flows through plane sudden-expansions", International Journal for Numerical Methods in Fluids, vol. 32, pp. 313-329, 2000.
[4] B. Pak, Y.I. Cho, S.U.S. Choi, "Separation and reattachment of nonnewtonian fluid flows in a sudden expansion pipe, "Journal of Non- Newtonian Fluid Mechanics, vol. 37, pp. 175-199, 1990.
[5] K. Khanafer, B. Al-Azmi, A. Al-Shammari, I. Pop, "Mixed convection analysis of laminar pulsating flow and heat transfer over a backward facing step, International Journal of Heat and Mass Transfer, vol. 51, pp. 5785-5793, 2008.
[6] K. F. Yu, Eric W. M. Lee, Jason K.K. Yuen, "High and low Reynolds number two-phase flows over a backward-facing step by 2D and 3D large eddy simulation," International Journal of Nonlinear Sciences and Numerical Simulation. Vol.10, no. 9, pp. 1135-1158, 2011.
[7] K. M. Kelkar, S. V. Patankar, "Numerical prediction of flow and heat transfer in a parallel plate channel with staggered fins", Journal of Heat Transfer, vol. 109, pp.25-30, 1987.
[8] M. Hassan, R. Sadri, G. Ahmadi, M. Dahari, S. Kazi, M.R. Safaei, E. Sadeghinezhad, Numerical study of entropy generation in a flowing nanofluid used in micro- and minichannels, Entropy 15 (2013) 144–155.
[9] E. Abu-Nada, Application of nanofluids for heat transfer enhancement of separated flows encountered in a backward facing step, Int. J. Heat Fluid Flow 29 (2008) 242–249.
[10] A.S. Kherbeet, H.A. Mohammed, B.H. Salman, The effect of nanofluids flow on mixed convection heat transfer over microscale backward-facing step, Int. J. Heat Mass Transfer 55 (2012) 5870–5881.
[11] H.A. Mohammed, A.A. Al-Aswadi, H.I. Abu-Mulaweh, A.K. Hussein, P.R. Kanna, Mixed convection over a backward-facing step in a vertical duct using Nanofluids-buoyancy opposing case, J. Comput. Theor. Nanosci. 11 (2014) 860–872.
[12] A.A. Al-aswadi, H.A. Mohammed, N.H. Shuaib, A. Campo, "Laminar forced convection flow over a backward facing step using nanofluids" International Communications in Heat and Mass Transfer, vol. 37, no.8, pp. 950-957, 2010.
[13] F.P Incropera, D.P Dewitt, T.L. Bergma, A.S. Lavine, fundamentals of heat and mass transfer, 6th edition Wiley, 2007.
[14] I.V. Lienhard, V. Lienhard, A heat transfer Textbook, third edition phlogiston press, 2006.
[15] Buongiorno J (2006) Convective transport in nanofluids. ASME J. Heat Transfer. 128, 240‑250.
[16] Hamilton RL and Crosser OK (1962) Thermal conductivity of heterogeneous two component systems. I&EC Fundamen. 1,187‑191.
[17] M. Corcione, heat transfer features of buoyancy-driven nanofluids inside rectangular enclosures differentially heated at the sidewalls, international journal of thermal sciences 49 (2010) 1536-1546.

NUMERICAL ANALYSIS OF PLATE LOADING TEST BASED ON FIELD WORKS

. Mohammed Salih Abd-Ali

Abstract

In this work, the bearing capacity of soil is evaluated for a substation of residential compound in Amarah city by plate loading test. The study consists of two parts, the first part is the field work which includes soil tests in the field for the locations of two rectangular foundations of transformers with dimensions (for each foundation) of (3.5 m x 2.5 m), called (Point 1 and Point 2). Results showed that the settlements in the locations of points 1 and 2 are within the permitted settlement, and the allowable bearing capacity of soil in these locations is (9.1) T/m^2.

In the second part of the study, the tested soils by plate loading test are analyzed using nonlinear three dimensional finite element models. ANSYS (11.0) program is used to analyze the three dimensional model. The adopted finite element models are found to give results in an excellent agreement with the field results. For the same applied load, it is found that the ratio of theoretical to field values of settlement is 0.99 for the both points (1) and (2).

The effect of size of plate of loading has been carried out to investigate its effect on the predicted finite element results. It is found that the settlement is increased with increasing the size of the loading surface.

التحليل العددي لفحص تحميل الصفيحة بالاعتماد على الاعمال الميدانية

د. محمد صالح عبد علي

الخلاصة

في هذا العمل، قيّمت سعة تحمل التربة لمحطة كهرباء ثانوية في مجمع سكني في مدينة العمارة بواسطة فحص تحميل الصفيحة. تتكون الدراسة من جزأين، الجزء الاول هو العمل الميداني والذي يتضمن فحوصات التربة موقعيا لاثنين من اساسات المحولات المستطيلة، أبعاد كل اساس (٣,٥ م * ٢,٥ م) سميت (نقطة ١ و نقطة ٢). أظهرت النتائج بأن الهبوط في مواقع النقطتين ١ و ٢ هو ضمن المسموح به، و 1 حمل المسموحة لهذه المواقع هو ٩.١ طن/م^2. وفي الجزء الثاني من الدراسة، تم تحليل الترب المفحوصة بواسطة فحص تحميل الصفيحة بالاعتماد على طريقة العناصر لتحليل النموذج الثلاثي البعد. وجد بأن التمثيل (ANSYS11.0)المحددة ثلاثية الابعاد اللاخطية. وتم اعتماد برنامج المستخدم للاساسات بطريقة العناصر المحددة يعطي قيم ذات اتفاق جيد مع النتائج الميدانية. وقد وجد إن نسب الهبوط للدراسة النظرية إلى قيم النتائج الميدانية هو ٩٩% لكلا النقطتين ١ و ٢. تم دراسة تأثير حجم صفيحة التحميل بأستخدام طريقة العناصر المحددة لمعرفة تأثيرها. وقد وُجد ان الهبوط يزداد بزيادة حجم سطح التحميل.

Introduction

Bearing capacity is the ability of soil to safely carry the pressure from any engineered structure without undergoing, a shear failure nor large settlements. Applying a bearing pressure which is safe with respect to failure does not ensure that settlement of the foundation will be within acceptable limits. Therefore, settlement analysis should generally be performed since most structures are sensitive to excessive settlement.

One of the methods for calculating the bearing capacity is the plate bearing test. This test method is a semi-direct method to estimate the bearing capacity of a soil in the field [1]. The test allows the determination of the relationship between the applied pressure and the displacements (pressure-displacement curve) [2]. The test has been used to avoid comprehensive geotechnical investigations which take more time and cost in small jobs with light load structures, and also to give quick results and data concerning bearing capacity of soil. The technique adopted in this study for carrying out the plate loading test has been described by ASTM D1194-94 [3] and BS 1377 part 9 [4].

According to the test procedure, a hydraulic device transfers pressure in stepwise through a circular rigid plate onto the surface of foundation, until the displacement or pressure criterion is satisfied.

Soil settlements are difficult to estimate. Settlement is stress induced, but is a statistical, time dependent accumulation of particle rolling and slipping which results in a permanent soil skeleton change. Elastic deformation (which is recoverable on removal of stress) is only a very small contribution to the total settlement of a foundation. It is a computational convenience to use elastic theory to predict soil settlement; however, reasonable estimates can be made if "elastic" parameters which describe the stress model over the range of actual stresses from the foundation can be obtained [1].

The scope of the research is to evaluate the allowable bearing capacity of soil for a substation of residential compound in Amarah city by plate loading test in the field, and then the plate loading tests will be analyzed using three

dimensional finite element models to check the validity of the adopted finite element models in predicting the overall behavior of the field plate bearing test, and to get more information about the size effect of plate loading test on the soil. The zones which should be tested were rectangular foundations of transformers with dimensions (for each foundation) of (3.5 m x 2.5 m) called (Point 1 and Point 2).

Load-Settlement Criteria

The load is applied to the plate in increments of the design load. The increments are applied until shear failure, the loading is 2 to 3 times the design load [5], or until a total settlement of 25 mm is obtained [1]. After the load is released, the elastic rebound of the soil should be recorded for a period of time at least equal to the duration of a load increment.

Field Plate Loading Test

The plate was placed on the soil to be tested. The load was applied to the plate in successive increments and a settlement was measured. Load increments are applied until the load intensity on the plate reach to (274 kPa) for all zones in the Amarah site as shown in the plates (1) to (2).

The load was applied to the plate via a factory calibrated hydraulic load cell and a hydraulic jack. Large plate with a diameter of 0.61m and thickness of 30mm was used.

Settlement is measured using dial gauges. In order to measure any tilt that may occur, two gauges on the perimeter of the plate were used. These gauges supported on rigid uprights fixed firmly into the ground at a distance of more than twice the plate width from the plate center. At each pressure increment, a

note was made of the load on the plate and dial gauge readings were made on a (0.25, 0.5, 1, 3.5, 7.5, 10, 15) minutes after load application. This would ensure sufficient readings in the early stages of each load application when movement occurs most rapidly.

After completion of observations for the last load increment, release this applied load in three decrements. Continue recording rebound deflections until the deformation ceases.

The results of these measurements were plotted in two forms: a time-settlement curve and a load-settlement curve as shown in Figs. (1) to (4).

Field Results

The field results of plate bearing test for the soil at the location of Point (1) and Point (2) are shown in Table (1). The recorded settlement, plastic settlement and elastic settlement for zones (Point 1 and Point 2) are given. Table (2) shows the settlement corresponding to maximum applied stress and allowable bearing pressures for the same zones.

Table (1): Recorded settlement, plastic settlement and elastic settlements for all tested zones [4]

Zone	Recorded Settlement (mm)	Plastic Settlement (mm)	Elastic Settlement (mm)
Point 1	7.48	4.35	3.13
Point 2	6.72	3.85	2.87

Table (2): Recorded settlement of the plate due to maximum applied stress

Zone	Recorded Settlement (mm)	Maximum Applied Stress (kPa)	Ultimate Bearing Pressure (kPa)*	Allowable Bearing Capacity (kPa)
Point 1	7.48	273.96	274	91
Point 2	6.72	273.96	274	91

*: Ultimate bearing pressure corresponding to recorded settlement of the plate.

Finite Element Model

The finite-element method is one of the mathematical methods in which continuous media is divided into finite elements with different geometries. It provides the advantage of idealizing the material behavior of the soil, which is non-linear with plastic deformations and is stress-path dependent, in a more rational manner. The finite-element method can also be particularly useful for identifying the patterns of deformations

and stress distribution during deformation and at the ultimate state. Because of these capabilities of the finite element method, it is possible to model the construction method and investigate the behavior of shallow footings and the surrounding soil throughout the construction process, not just at the limit equilibrium conditions [6].

In the present section, the plate loading tests have been analyzed using three dimensional finite element models. The main objectives of the analysis are to check the validity of the adopted finite element models in predicting the overall behavior of the field plate bearing test, and to get more information about stresses and strains developed in the soil.

The analysis is made by using **ANSYS 11.0** computer program. The three dimensional 8-noded brick element (SOLID45) is selected to represent the soil

and the loading plate. The contact between loading plate and soil is represented by TARGE 170 and CONTA 173 elements.

Stresses in a Soil Mass due to Footing Pressure

Results from elastic theory indicate that the increase in vertical stress in the soil below the center of a strip footing of width B is approximately 20% of the foundation pressure at a depth 2.5B. In the case of a square footing the corresponding depth is 1.2B. For practical purposes these depths can normally be accepted as the limits of the zone of influence of the respective foundations and are called ***the significant depth***. It is essential that the soil conditions are known within the significant depth of any foundation [7].

To study the behavior of the plate loading test on soil using finite element analysis, it is necessary to simulate the conditions as close as possible to those occur in the field. As mentioned above, the stresses applied on the soil decrease with the depth inside the soil. Sing [8] mentioned that these stresses vanish at a depth equal to width of footing. Therefore the the depth should be equal or greater than (610mm to 1.2 B, whichever is greater), to ensure the stress be within the depth of the model. In this research was taken equal to 1.5 m. The plan dimensions of soil were decided depending on the Boussinesq and Westergaard theories. The Boussinesq and Westergaard theories are more mathematically oriented methods for estimating soil pressures at various points in a soil stratum. Both these are based on elastic methods. Figures (5) and (6) show the pressure bulb for square footing. It can be seen that the stresses expand horizontally up-to a maximum distance of 1.25 B approximately from centerline of footing. So, the width and length in this research are taken equal to 1.5 m.

In order to prevent any rigid motions of the whole problem domain, it is assumed that both the displacements in the horizontal and vertical directions are

zero for all nodes along the bottom boundary of the mesh. On the vertical side boundaries, the horizontal displacements have been assumed to be zero too [9].

The load, in the present study, is distributed on the nodes under the loading plate in such a manner that each node takes a load equal to the uniform applied pressure times the related area to the node, and for the circular loading plate, an equivalent square loading area is assumed to calculate the loads on nodes [10].

The yield criteria depend on the behavior of the soil. The Drucker - Prager ***(DP)*** criterion is used for soil as yield criteria which is applicable to granular (frictional) material such as soil, and uses the cone approximation to the Mohr-Coulomb law.

The soil behavior is described by the Mohr-Coulomb model, having Young's modulus, E_s= 140 MPa, Poisson's ratio, ν= 0.3, c = 1 kPa and angle of shearing resistance, $\phi = 30^o$.

Load-Settlement Relationship

Figures (7) to (10) illustrate the pressure-settlement relationships and the contours for vertical displacement of the tested soils in the points (1 and 2). These figures show that the predicted behavior concerning the load-settlement curve is almost similar to the field results. The relationships start linear to fourth of the ultimate load and then become nonlinear. Good agreement between the field and theoretical results is achieved. The ratio of theoretical to field value of settlement is 0.99 for the both points (1) and (2).

The Size Effect in Plate Loading Test on Soil

To investigate the effect of size of plate loading test on the nonlinear finite element analysis of soil, Point (1) has been chosen to carry out this study. In each numerical test, plate diameter has been considered to vary while the other parameters being held constants in order to isolate the effect of the size. In order to study the effect of size of plate loading test on the soil (D), different values of (D) have been considered. The selected values for this parameter are

0.2, 0.4, 0.6, 0.8 and 1.0 m. Figure (11) show the settlement versus plate diameter relationship obtained from the finite element model for the selected values of (D). It can be seen, the settlement increases proportional with the size of the loading surface.

Conclusions

In this study, the main concluding remarks that have been achieved from the test results may be summarized as follows:-

1- The settlement faster increased in the first few seconds after each new load increment and contributed to obtain a plastic settlement.
2- The average elastic settlement for points 1 and 2 forms 42.27 % of total settlement, this represent high percentage and is contrasted with that mentioned by reference (1).
3- Nonlinear finite element solution by ANSYS package program using three dimensional elements for modeling the plate loading test on soil gives excellent agreement with the field results for the load-settlement relationships.
4- The finite element analysis shows the increase in the size of plate loading test of the soil (D) causes an increase in the settlement.

References

1- Bowels, J. E., **"Foundation Analysis and Design"**, McGraw-Hill Book Company, New York, Fourth Edition, 1988.
2- Pantelidis, L., **"Determing of the Soil Strength Characteristics Through the Plate Bearing Test"**, Foundations of Civil and Enviromental Engineering, No. 11, 2008.
3- ASTM D1194-94, **"Test Method for Bearing Capacity of Soil for Static Load and Spread Footing"**, Annual Book of ASTM Standards: Volume 04.08, October 2003.
4- British Standards Institution, **"BS 1377, Part 9"**, British Standards Institution, London, 1990.

5- British Standards Institution, **"BS 5930: 1981"**, British Standards Institution, London, 1981.

6- Ornek, M., Demia, A., Laman, M. and Yildiz, A., **"Numerical Analysis of Circular Footings on Natural Clay Stabilized with a Granular Fill"**, Acta Geotechnica Slovenica, 2012.

7- Craig, R. F., **"Soil Mechanics"**, Van Nostrand Reinhold (UK) Co. Ltd, Fourth Edition, 1987.

8- Sing, B., **"Soil Mechanics and Foundation Engineering"**, Al- Mousl University, Arabic Edition.

9- Teodoru, I. and Toma, I., **"Numerical Analysis of Plate Loading Test"**, Gheorghe Asachi University, 2009.

10- Abd-Ali, M., S., **"Experimental and Numerical Investigation of Concrerete Slabs on Grade"**, Ph.D.Thesis, University of Basrah, 2010.

Plate (1): Plate Bearing Test for Location of Point (1)

Plate (2): Plate Bearing Test for Location of Point (2)

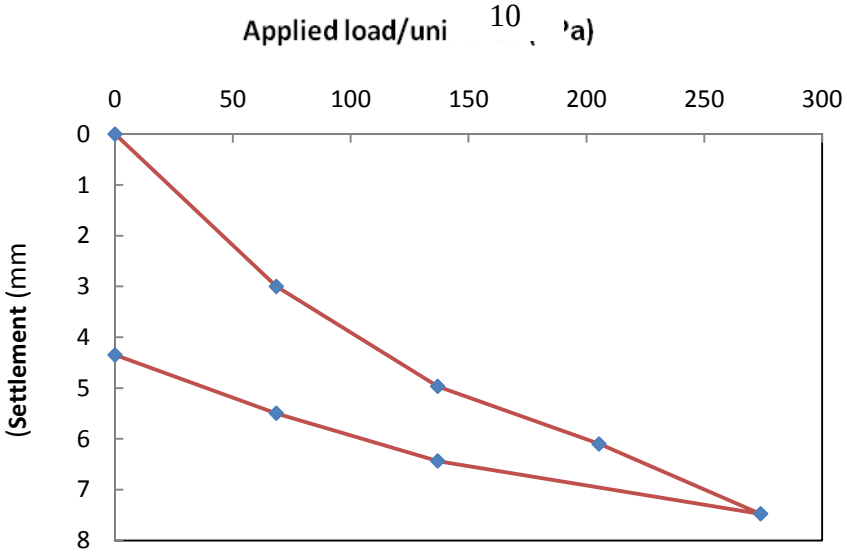

Figure (1): Load-Settlement Curve for Point (1)

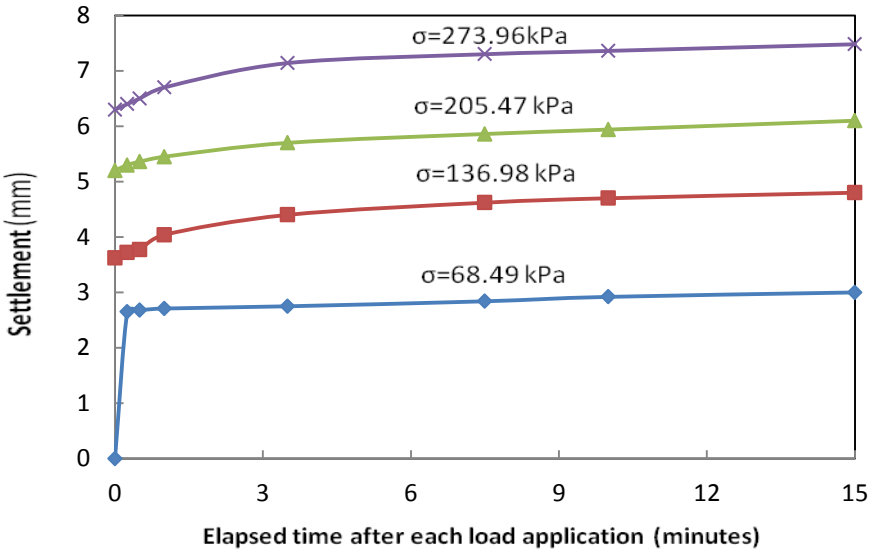

Figure (2): Time-Settlement Curves for Point (1)

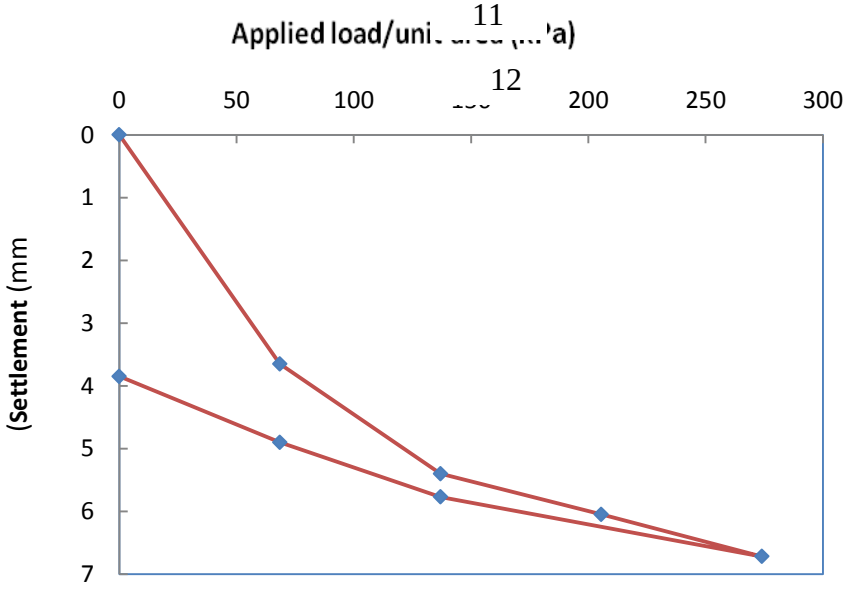

Figure (3): Load-Settlement Curve for Point (2)

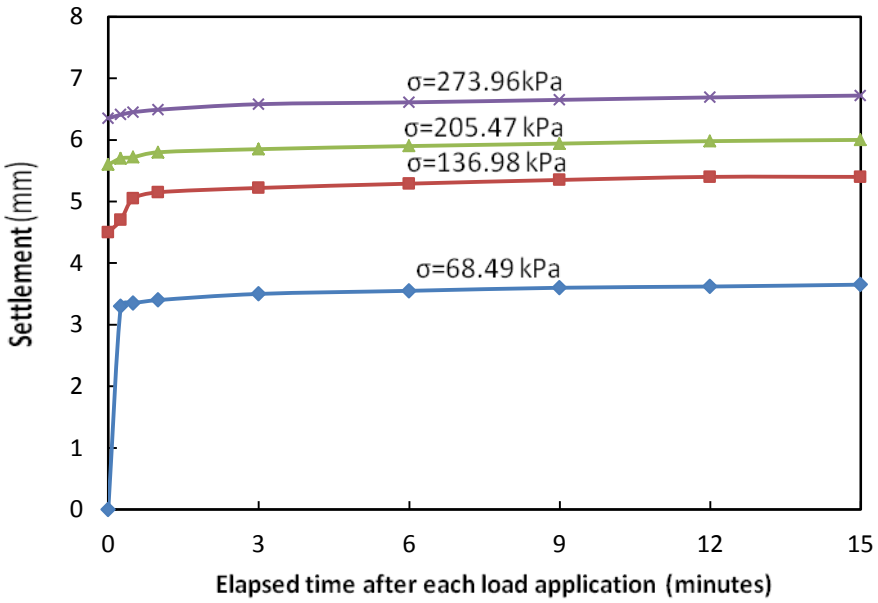

Figure (4): Time-Settlement Curves for Point (2)

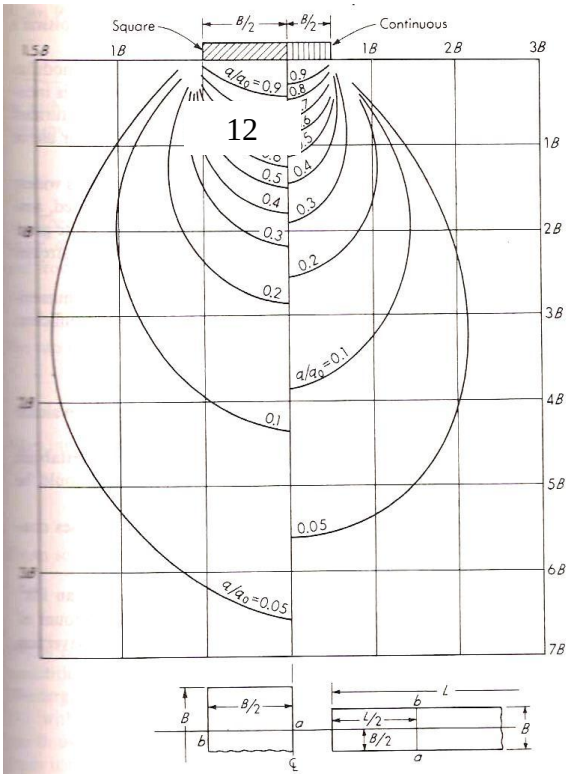

Figure (5): Pressure Isobars Based on the Boussinesq Equation for Square and Continuous Footings. Applicable Only Along Line *ab* (Ref.1)

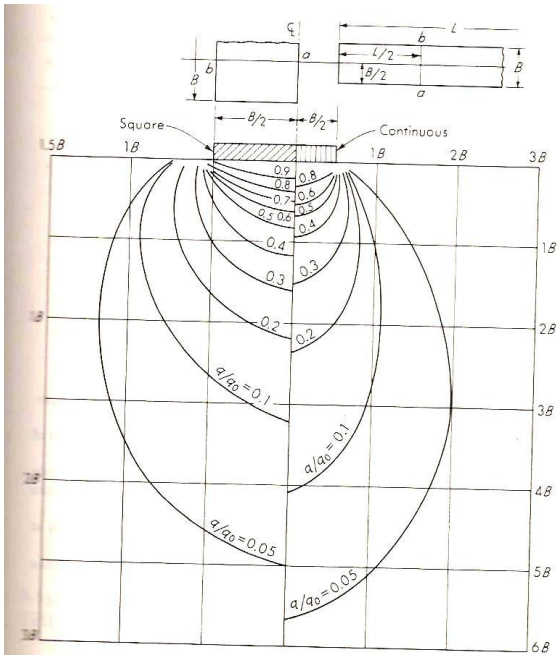

Figure (6): Pressure Isobars Based on the Westergaard Equation for Square and Continuous Footings. Values for the Continuous Footings are at the Point *L/2* from the End (Ref.1).

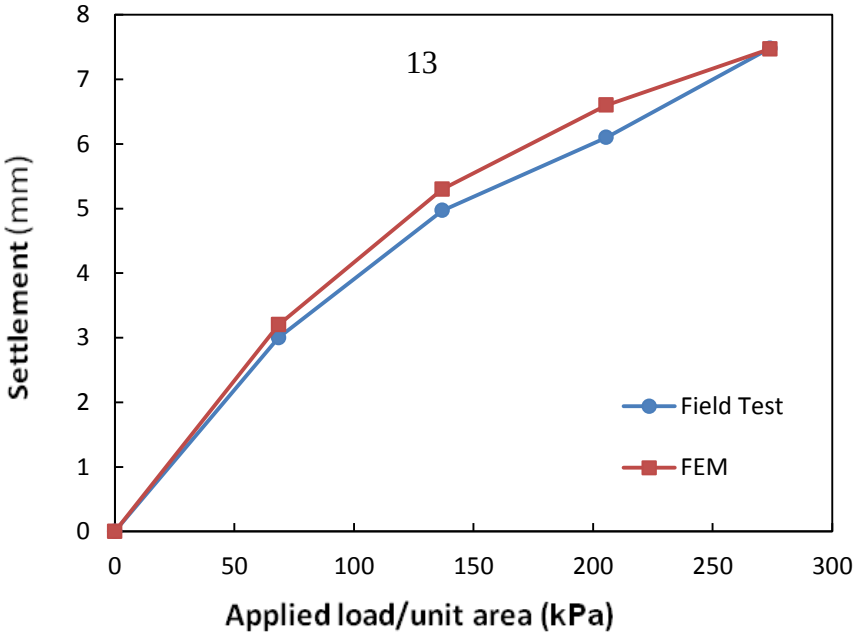

Figure (7) Variation of Settlement with Load for Point (1)

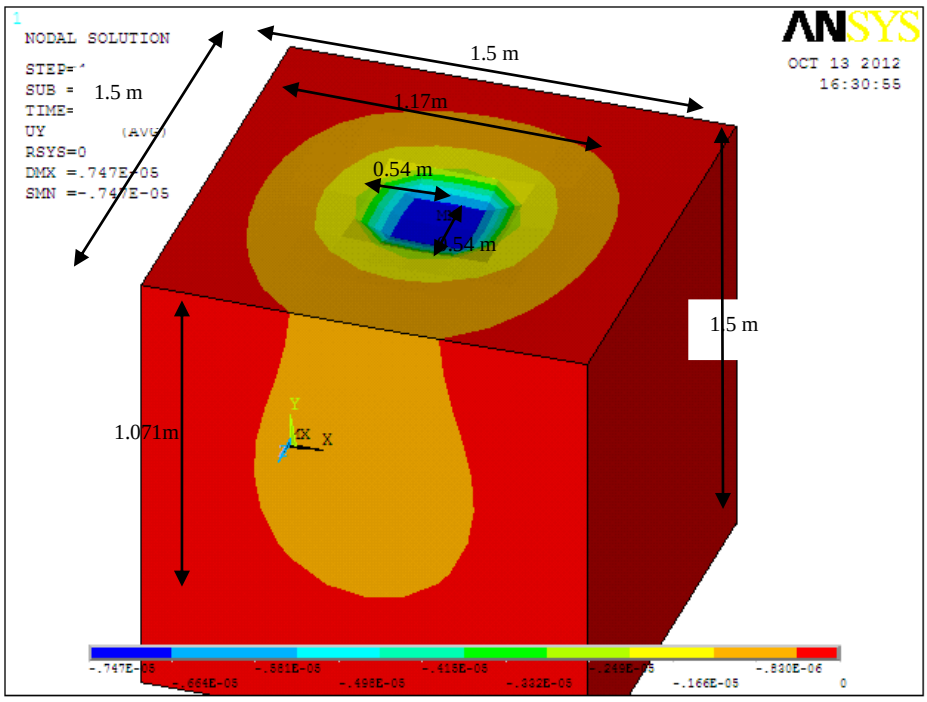

Figure (8) Contour Plot for Vertical Displacement (y) for Point (1)

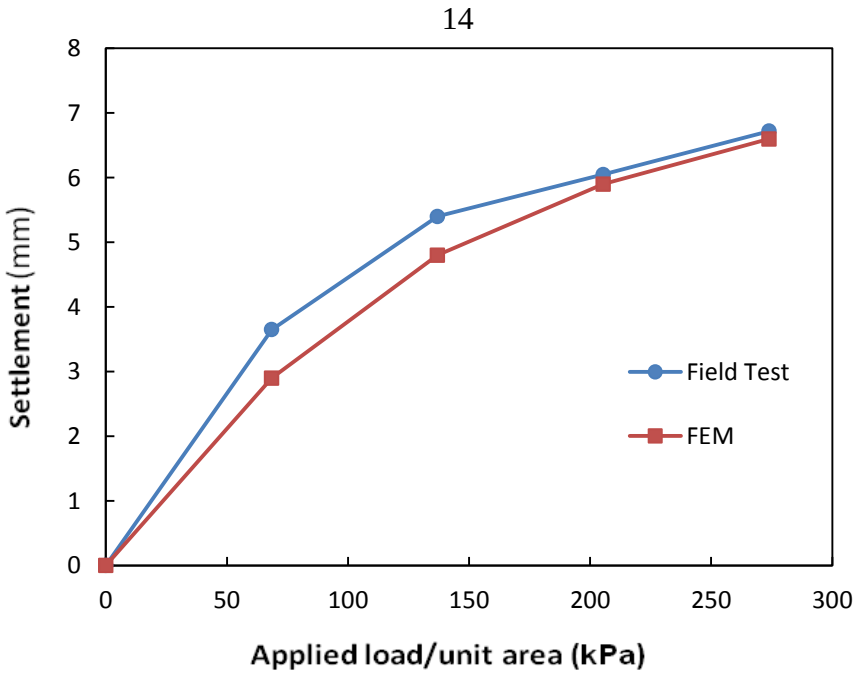

Figure (9) Variation of Settlement with Load for Point (2)

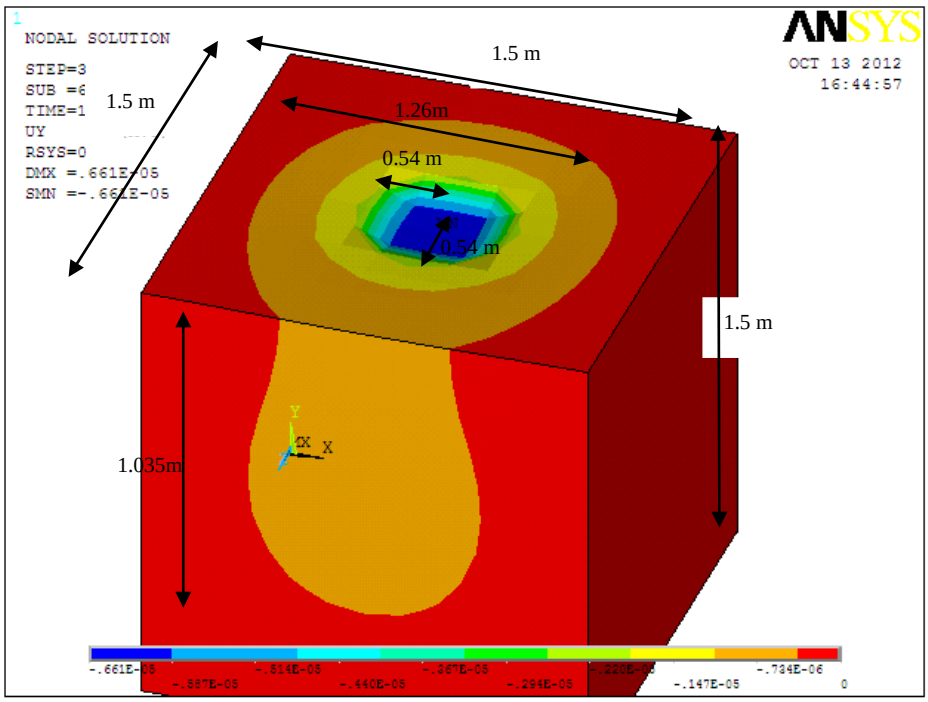

Figure (10) Contour Plot for Vertical Displacement (y) for Point (2)

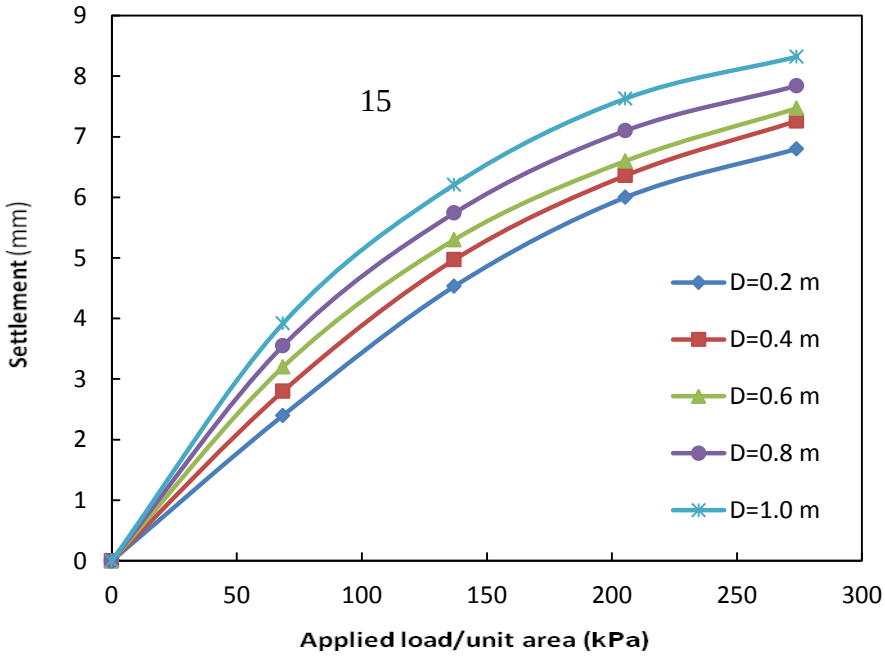

Figure (11) Numerical load vs. settlement curves

STRESS INTENSITY FACTOR FOR DOUBLE EDGE CRACKED FINITE PLATE SUBJECTED TO TENSILE STRESS

Lattif Shekher Jabur Najah Rustum Mohsin
Iraq, Southern Technical University, Technical Institute-Nasiriya, Mechanical Technics Department.
Lsh58@yahoo.com Najahr2000@yahoo.com

ABSTRACT

A finite rectangular plate with double edge crack under uniaxial tension depends on the assumptions of Linear Elastic Fracture Mechanics LEFM and plane strain problem are studied in the present paper. The effect of crack position, crack oblique and the kinked crack orientation are investigated to predict if a crack starts to grow. These problems are solved by calculating the Stress Intensity Factor SIF for mode I (KI) and II (KII) near the crack tip theoretically using mathematical equations and numerically using finite element software ANSYS R15. A good agreement is observed between the theoretical and numerical solutions. The results show that the KI increases with increasing the relative crack length and tensile stress and these values are increased when the crack position draws near the plate edge while in case of parallel cracks the mutual shielding effect reduces KI in each crack. In mixed mode, it is shown that the maximum values of KI and KII occur at crack angle $\beta=0^o$ and 45^o, respectively and the orientation of the kinked crack have significant effects on the KI and KII.

Key Words: Double edge crack, SIF, crack oblique, ANSYS R15, kinked.

معامل شدة الإجهاد لصفيحة محددة ذات شق طرفي مزدوج معرضة لأجهاد شد

د. لطيف شخير جبر نجاح رستم محسن
العراق - الجامعة التقنية الجنوبية - المعهد التقني في الناصرية - قسم التقنيات الميكانيكية

الملخص:

في هذا البحث تم دراسة صفيحة محددة مستطيلة الشكل ذات شق طرفي مزدوج معرضة لأجهاد شد بأتجاه واحد أعتماداً على فرضيتي ميكانيكية الكسر المرن الخطية وأنفعال المستوي. تمت دراسة تأثير موقع الشق وزاوية الشق وزاوية الشق المتفرع للتنبوء بأمكانية نمو الشق. هذه المشاكل تم حلها بحساب معامل شدة الإجهاد للطور الأول و الثاني قرب قمة الشق نظرياً بأستخدام المعادلات الرياضية وعددياً بأستخدام برنامج العناصر المحددة ANSYS 15. لوحظ ان هنالك تطابق جيد بين الحل النظري والعددي. بينت النتائج ان الطور الأول لشدة الأجهاد يزداد بزيادة الطول النسبي للشق وأجهاد الشد وهذه القيمة تزداد عندما يقترب موقع الشق من حافة الصفيحة بينما في حالة الشقوق المتوازية فأن تأثير الدرع الواقي المشترك يقلل من قيمة الطور الأول لكل شق. في الطور المختلط، لاحظنا ان القيمة القصوى للطور الأول والثاني تحدث عندما تكون زاوية الشق تساوي 0^o و 45^o على التوالي والميلان للشق المتفرع له تأثير واضح على قيمة الطور الأول والثاني لمعامل شدة الإجهاد.

1. INTRODUCTION

Recent development in engineering structures shows that small cracks in the body of structures can cause a failure despite of the authenticity of elasticity theory and strength of materials. As a result, fracture mechanics filed which is concerned with the propagation of cracks in materials has developed to study more about this subject, Ali et al. [1]. The crack may grow to cause structure failure due to low stress, which acts on a structure. Stress Intensity Factor (SIF) is a most important single parameter in fracture mechanics, which can be used to examine if a crack, would propagate in a cracked structure under particular loading condition, i.e. it controls the stability of the crack, Saleh [2] .

No structure is entirely free of defects and even on a microscopic scale these defects act as stress raisers which initiate the growth of cracks. The theory of fracture mechanics therefore assumes the pre-existence of cracks and develops criteria for the catastrophic growth of these cracks. In a stressed body, a crack can propagate in a combination of the three opening modes that shown in Figure 1. Mode I represents opening in a purely tensile field while modes II and III are in-plane and anti-plane shear modes respectively. The most commonly found failures are due to cracks propagating predominantly in mode I, and for this reason materials are generally characterized by their resistance to fracture in that mode, Arencón and Velasco [3].

The double – edge cracked plate is a common specimen in research and practice for fracture mechanics. It has been studied by Bowie [4], who gave solutions for a circular hole with a single edge crack and a pair of symmetrical edge cracks in a plate under tension by using a conformal mapping technique, while Newman [5], using the boundary collocation method, and Murakami [6], used the body force method to analyze the tension problem for an elliptical hole with symmetrical edge cracks. Isida and Nakamura [7], made an analysis for a slant crack emanating from an elliptical hole under uniaxial tension and shear at infinitity by using the force body method.

Yavuz et al. [8] analyzed multiple interacting cracks in an infinite plate to determine the overall stress field as well as SIF for crack tips and singular wedges at crack kinks. A perturbation approach for the elasticT-stress at the tip of a slightly curved or kinked crack based on used by Li et al. [9], while Saleh [2] analyzed and determined the KII of several crack configurations in plates under uniaxial compression using a two-dimensional Finite Element Method (FEM). Various cases including diagonal crack and central kinked crack are investigated with different crack's length, orientation and location. Antunes et al. [10] studied numerically the effect of crack propagation on crack tip fields. Spagnoli et al. [11] described the influence of the degree of crack deflection on the fatigue behavior and Ali et al. [1] utilized the SIF to determine the stress intensity near the tip of a crack using FEM.

Recentllty, Mohsin [12] studied the KI for center, single edge and double edge cracked finite plate subjected to tension stress to investigate the differences between the theoretical and numerical solutions.

Fracture mechanics is used to evaluate the strength of a structure or component in the presence of a crack or flaw, Fatemi [13]. In 1938 Westergaard solved the stress field for an infinitely sharp crack in an infinite plate (Figure 3). The elastic stresses were given by the equations, Rae [14]

$$\sigma_{xx} = \frac{KI}{\sqrt{2\pi r}}\cos\left(\frac{\theta}{2}\right)\left[1-\sin\left(\frac{\theta}{2}\right)\sin\left(\frac{3\theta}{2}\right)\right] \quad \text{.....(1)}$$

$$\sigma_{yy} = \frac{KI}{\sqrt{2\pi r}}\cos\left(\frac{\theta}{2}\right)\left[1+\sin\left(\frac{\theta}{2}\right)\sin\left(\frac{3\theta}{2}\right)\right] \quad \text{.....(2)}$$

$$\tau_{xy} = \frac{KI}{\sqrt{2\pi r}}\cos\left(\frac{\theta}{2}\right)\sin\left(\frac{\theta}{2}\right)\cos\left(\frac{3\theta}{2}\right) \quad \text{.....(3)}$$

i.e $\sigma_{ij} = \left(\frac{KI}{\sqrt{2\pi r}}\right) f_{ij}(\theta),$ .....(4)

where σ_{ij} is stress tensor, r is the distance from the crack tip, θ is the angle with respect to the plane of the crack, and f_{ij} are functions that are independent of the crack geometry and loading conditions.

From Saouma [15]

$$\sigma_{xx} = \sigma\sqrt{\frac{a}{2r}}\cos\frac{\theta}{2}\left(1+\sin\frac{\theta}{2}\sin\frac{3\theta}{2}\right)+\cdots \quad \text{.....(5)}$$

$$\sigma_{yy} = \sigma\sqrt{\frac{a}{2r}}\cos\frac{\theta}{2}\left(1-\sin\frac{\theta}{2}\sin\frac{3\theta}{2}\right)+\cdots \quad \text{.....(6)}$$

$$\tau_{xy} = \sigma\sqrt{\frac{a}{2r}}\sin\frac{\theta}{2}\cos\frac{\theta}{2}\cos\frac{3\theta}{2}+\cdots \quad \text{.....(7)}$$

When θ = 0, we have from (1) to (7)

$$\sigma_{ij} = \left(\frac{KI}{\sqrt{2\pi r}}\right) \quad \text{.....(8)}$$

$$\sigma_{xx} = \sigma_{yy} = \sigma\sqrt{\frac{a}{2r}} \quad \text{.....(9)}$$

$$\tau_{xy} = 0, \quad \text{.....(10)}$$

then

$$\sigma_{xx} = \sigma_{yy} = \left(\frac{KI}{\sqrt{2\pi r}}\right) = \sigma\sqrt{\frac{a}{2r}} \quad \text{.....(11)}$$

Then, the KI of a finite plate under tension load is

$$KI = \sigma\sqrt{\frac{a}{2r}}\sqrt{2r\pi} = \sigma\sqrt{\pi a}, \quad \text{.....(12)}$$

Stress intensity solutions are given in a variety of forms, K can always be related to the through crack through the appropriate correction factor, Anderson [16]

$$K(I, II, III) = Y\sigma\sqrt{\pi a}\,, \quad \ldots\ldots\ldots\ldots\ldots\ldots(13)$$

where a: characteristic crack dimension and Y: dimensionless constant that depends on the geometry and the mode of loading.

When a body subjected to tension loading, the stress intensity factors for mode I and mode II to any planar crack oriented $90° - \beta$ (Figure 4) from the applied normal stress (KI_β and KII_β) can be obtained depend on Sih et al. [17] as follow

$$KI_\beta = KI.\cos^2\beta \ldots\ldots\ldots\ldots\ldots\ldots(14)$$

$$KII_\beta = KI.\cos\beta.\sin\beta\,, \ldots\ldots\ldots\ldots..(15)$$

where KI is the mode I stress intensity when $\beta = 0$.

Supposing that the crack in question forms an infinitesimal kink at an angle α from the plane of the crack, as Figure 5 illustrates. The local SIF at the tip of this kink differs from the nominal K values of the main crack. If we define a local x-y coordinate system at the tip of the kink , the local mode I and mode II stress intensity factors at the tip are obtained by summing the normal and shear stresses, respectively, at α, Anderson [16]:

$$KI_\alpha = \sigma_{yy}\sqrt{2\pi r} = \left[\frac{3}{4}\cos\left(\frac{\alpha}{2}\right) + \frac{1}{4}\cos\left(\frac{3\alpha}{2}\right)\right]KI_\beta + \left[\frac{-3}{4}\left[\sin\left(\frac{\alpha}{2}\right) + \sin\left(\frac{3\alpha}{2}\right)\right]\right]KII_\beta \quad \ldots\ldots$$

(16)

$$KII_\alpha = \tau_{xy}\sqrt{2\pi r} = \left[\frac{1}{4}\left[\sin\left(\frac{\alpha}{2}\right) + \sin\left(\frac{3\alpha}{2}\right)\right]\right]KI_\beta + \left[\frac{1}{4}\cos\left(\frac{\alpha}{2}\right) + \frac{3}{4}\cos\left(\frac{3\alpha}{2}\right)\right]KII_\beta\,, \quad \ldots\ldots$$

(17)

where KI_α and KII_α are the local SIF at the tip of the kink.

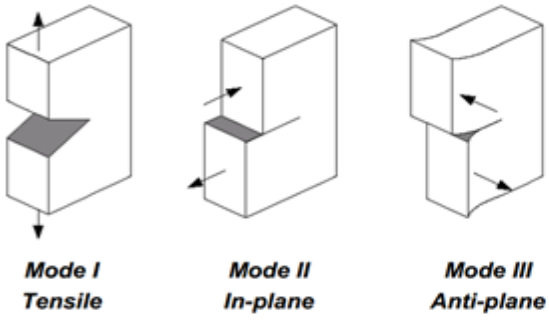

Figure 1: Fracture modes [3].

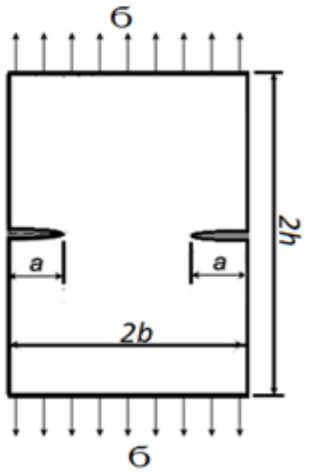

Figure 2 Double edge crack plate

specimen with dimensions.

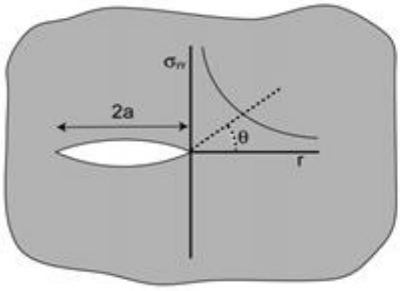

Figure 3: Crack with sharp edge [14]

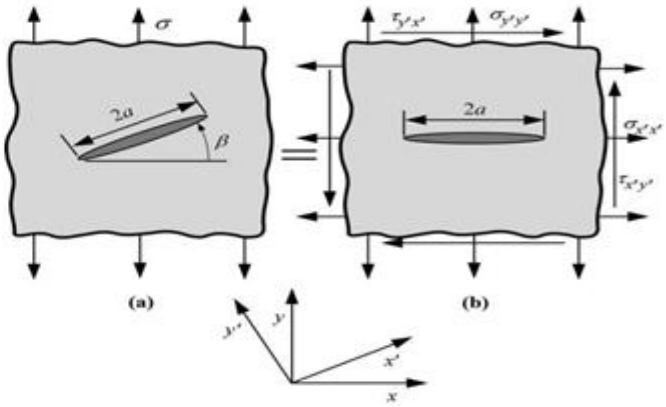

Figure 4: Through crack in an infinite plate for the general case where the principal stress is not perpendicular to the crack plane[16].

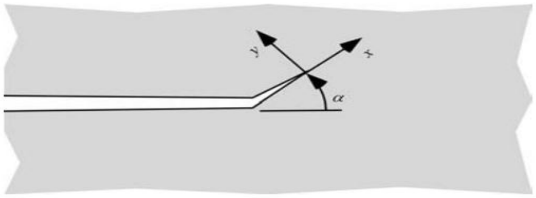

Figure 5: Infinitesimal kink at the tip of a macroscopic crack [16]

2. MATERIALS AND METHODS

Based on the assumptions of Linear Elastic Fracture Mechanics LEFM and plane strain problem, Double Edge Notch Tension (DENT) finite plate specimen as shown in Figure 2 is studied using theoretical and numerical solutions.

2.1. SPECIMENS MATERIAL

The material of plate specimens is a Carbon Steel with modulus of elasticity =202 E-3 MN/m^2, poison's ratio = 0.292 and density = 7820 Kg/m^3, Kulkarni [18].

2.2. SPECIMENS MODEL

To calculate the SIF in numerical and theoretical solutions, five models have been selected as follows

I. Double Edge Notch (DEN) is in the middle of the plate's length (Figure 6a and b).
II. DEN is in the various positions along Y-axis (Figure 6d).
III. Two parallel DEN are in the various positions along Y-axis (Figure 6e).
IV. DEN with crack orientation is in the middle of the plate's length (Figure 6f).

V. DEN with crack orientation and kinked is in the middle of the plate's length (Figure 6g).

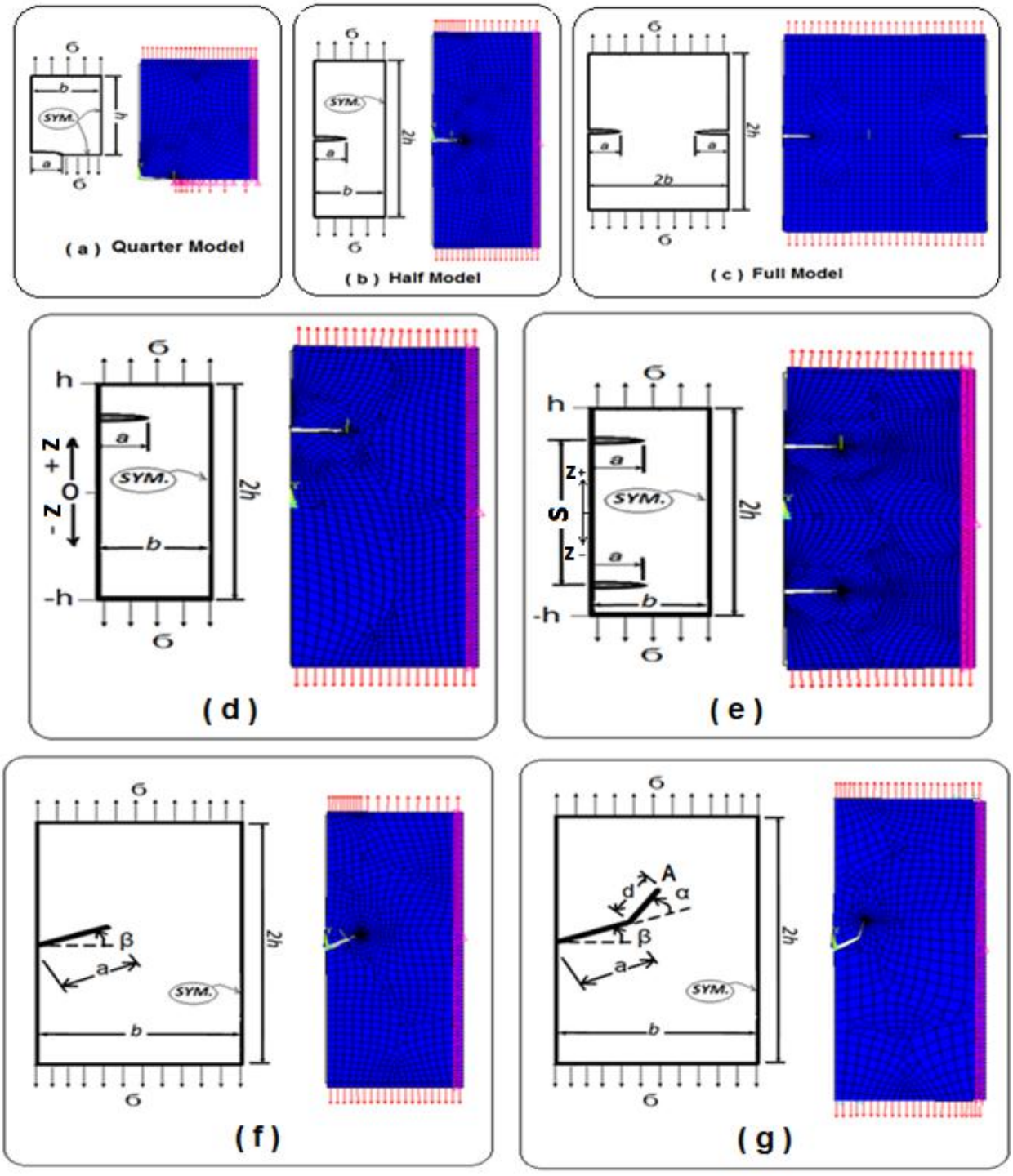

Figure 6: ANSYS models with mesh and dimensions.

2.3. THEORETICAL SOLUTION

For theoretical calculation, many researchers reported different equations for many cases to evaluate the SIF for double edge cracks. In this paper, the SIFs are theoretically calculated as follow : -

- KI values for model I, II and III (i.e. DENT without orientation (β = 0)) are calculated based on (13), where

a) From Nassar [19]

$$Y = \left(\frac{\left(1.122 - 0.561\left(\frac{a}{b}\right) - 0.205\left(\frac{a}{b}\right)^2 + 0.471\left(\frac{a}{b}\right)^3 - 0.190\left(\frac{a}{b}\right)^4\right)}{\sqrt{1-\left(\frac{a}{b}\right)}} \right) \quad \text{..... (18)}$$

b) From Tada et al. [20]

$$Y = \left(1 + 0.122cos^4\left(\frac{\pi a}{2b}\right)\right)\sqrt{\frac{2b}{\pi a}tan\left(\frac{\pi a}{2b}\right)} \quad \text{..... (19)}$$

- Values of KI_β and KII_β for model IV (i.e. DENT with crack orientation) are calculated using equations (14)

and (15), respectively.

- Values of KI_α and KII_α for model V (i.e. DENT with crack kinked) are calculated using equations (16) and

(17), respectively.

2.4. NUMERICAL SOLUTION

Numerically, all the five models (as mensioned above) are solved to calculate the SIFs using finite element software ANSYS R15 with PLANE183 element as a discretization element.

2.5. PLANE183 ELEMENT DESCRPTION

PLANE183 is an ANSYS element with quadrilateral and triangle shape, plane strain behavior and pure displacement formulation. It is defined by 8 nodes (I, J, K, L, M, N, O, P) for quadrilateral element or 6 nodes (I, J, K, L, M, N) for triangle element, two degrees of freedom (Ux , Uy) at each node (translations in the X and Y directions) [21]. The geometry, coordinate system and node locations for this element are shown in Figure 7.

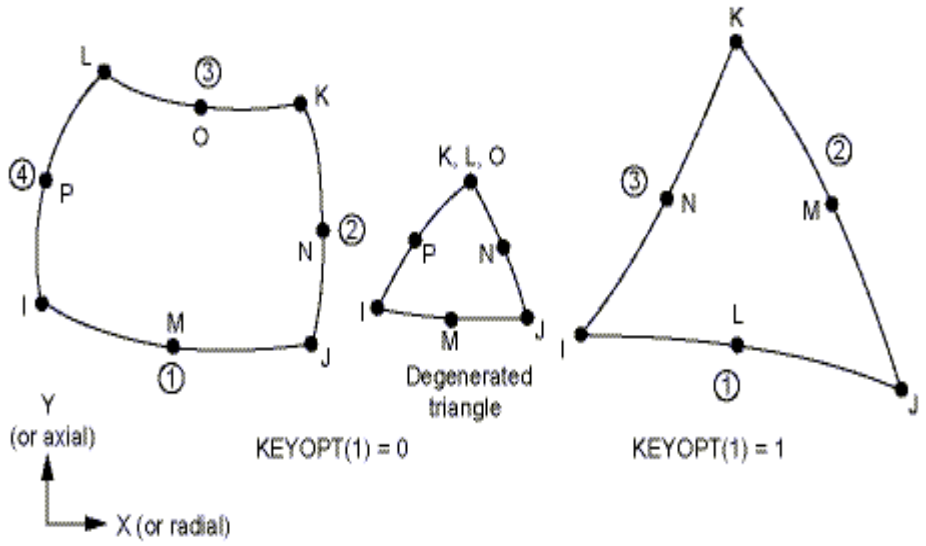

Figure 7: PLANE183 element geometry, coordinate system and node locations [21].

2.6. Applications

To explain the effect of the five cases that mention above on the SIFs, many cases are studied theoretically and numerically as reported in Table 1.

Table 1: The cases studied with the parameters, solution types and number of figures.

No. of Studied Cases	Changed Parameter in this case study		Other Parameters	Type of Solutions	Figure No.
	Name	Values			
I	a/b	0.1 to 0.6 with step 0.05	σ_t =200 Mpa b = 50mm h = 62.5mm	Theoretical and Numerical	8
	σ	50 to 250Mpa with step 50Mpa	b = 50mm h = 62.5mm a=15mm	Theoretical and Numerical	9
II	z	-50 to 50mm with step 5mm	σ_t =200 Mpa b = 50mm h=62.5mm a=15mm	Numerical	10
III	s	20mm to 100mm with step 10mm	σ_t =200 Mpa b = 50mm h=62.5mm a=15mm	Numerical	11
II and III	z	-50 to 50mm with step 5mm	σ_t =200 Mpa b = 50mm h=62.5mm a=15mm	Numerical	12
IV	β	-75° to 75° with step 5°	σ_t =200 Mpa b = 50mm h=62.5mm a=15mm	Theoretical and Numerical	13 and 14
V	(α+ β)	0°, 15°, 30° 45°, 60° 65°, 70° 75°, 80° 85°, 90°	σ_t =200 Mpa b = 50mm h=62.5mm a=10mm d=5mm β = 15°	Theoretical and Numerical	15 and 16
V	(α+ β)	0°, 15°, 30° 45°, 60° 65°, 70° 75°, 80° 85°, 90°	σ_t =200 Mpa b = 50mm h=62.5mm a=10mm d=5mm β = (15° , 45°, 75°)	Numerical	17 and 18

3. RESULTS AND DISCUSSIONS

3.1. Effect of relative crack length and tensile stress on the KI

Figures 8 and 9 explain the theoretical and numerical variation of KI for model I with different values of relative crack length (a/b) and tensile stresses (σ_t), respectively. It can be seen that increasing the ratio of a/b and σ_t leads to increasing the value of K_I in a high level. From these figures, it is clear that there is no significant difference between the Theoretical (Eq.18 and Eq.19) and numerical (Quarter and half model) results with a maximum discrepancy of 0.79%.

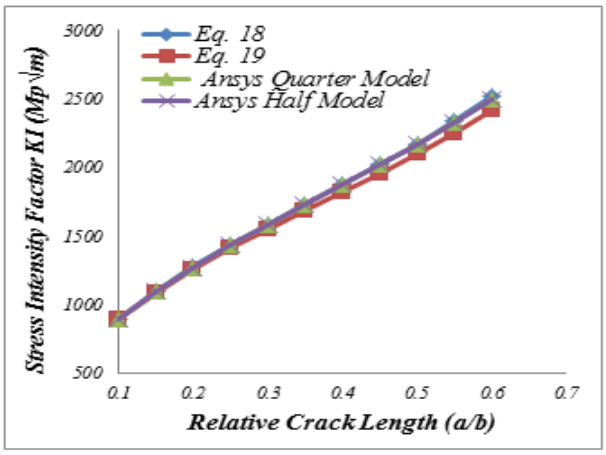

Figure 8: Theoretical and numerical Variation of KI with (a/b) ratio.

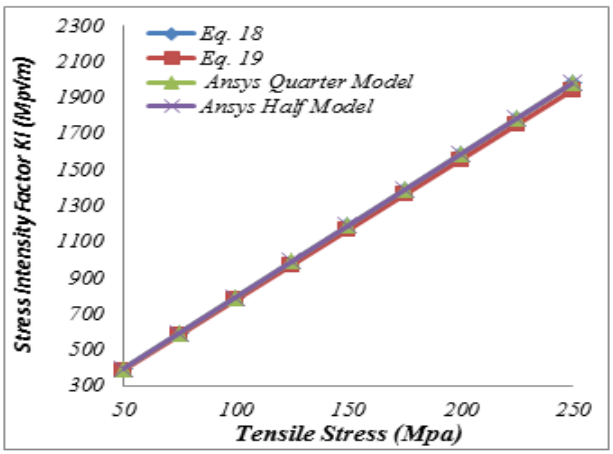

Figure 9: Theoretical and numerical Variation of KI with σ_t.

3.2. Effect of DENT position on the KI

The variation of KI for model II with different edge crack positions along Y-axis (z) are shown in Figure 10. It can be seen that the KI values increases slightly from z = 0 to z = ±30mm, after that, KI values rises in a high level. Generally, maximum KI values appear at when the crack near the plate edge while the minimum values occur when its position at the middle of plate (i.e. z = 0).

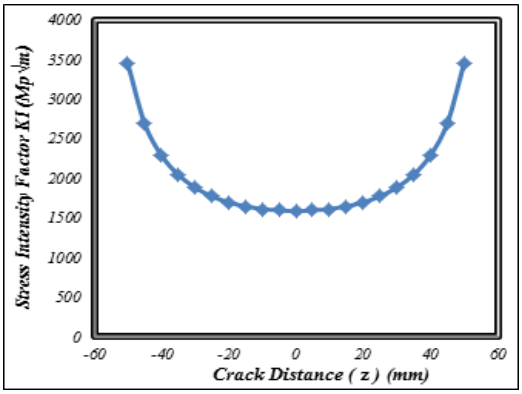

Figure 10: Variation of KI with crack distance (z).

3.3. Effect of two parallel DENT position on the KI

Figure 11 illustrates the variation of KI for model III with various two parallel edge crack positions along Y-axis (s). From this figure, it can be seen that the KI values are increased with increasing the distance between the two parallel cracks (s).

In the other hand, Figure 12 explains a comparison between the effect of one and two edge crack positions along Y-axis on the KI from z = -50mm to z = +50mm. It is clear that the KI values for model II are greater than of model III at z = 0, after that, the difference decreases slightly from z=0 to z= ±40mm and vanished when z>±40mm. Generally, In case of parallel cracks, the crack tends to shield one another and this mutual shielding effect reduces KI in each crack. The mutual shielding effect increase with decrease the distance between the two parallel cracks.

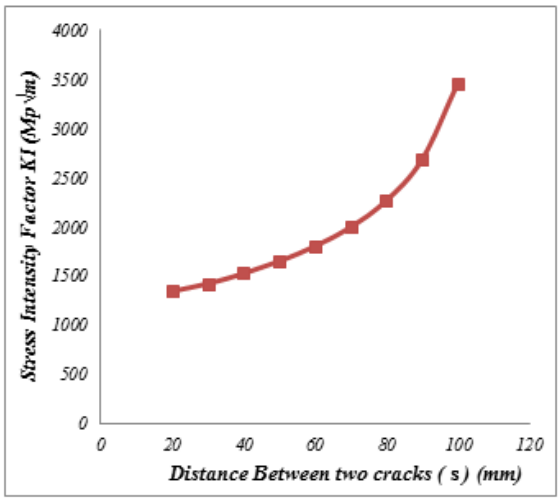

Figure 11: Variation of KI with the distance between two parallel cracks (s).

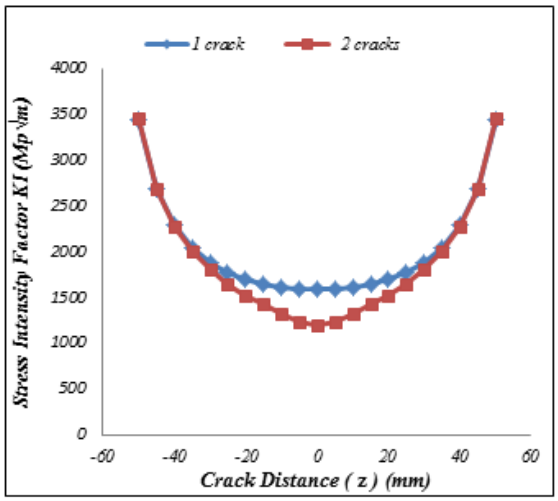

Figure 12: Variation of KI with crack distance for 1 and 2 cracks (z).

3.4. Effect the DENT inclination angle on the KI and KII

The variation of KI and KII values with the double edge crack angle (β) for model IV are shown in figures 13 and 14, respectively. From these figures, it is too easy to see that the maximum KI and KII occur at $\beta = 0^o$ and $\beta = 45^o$, respectively. Furthermore, KI gradually decreases when $0^o > \beta > 0^o$ while KII gradually decreases when $45^o > \beta > 45^o$. In addition, it is shown that a small difference between KI values in numerical and theoretical solution but this difference will increase when calculate the KII especially when $60^o > \beta > 30^o$ and $-60^o < \beta < -30^o$. It is clear that the crack angle has a considerable effect on the KI and KII values as a result of the shear stresses and normal stresses depend on the angle values.

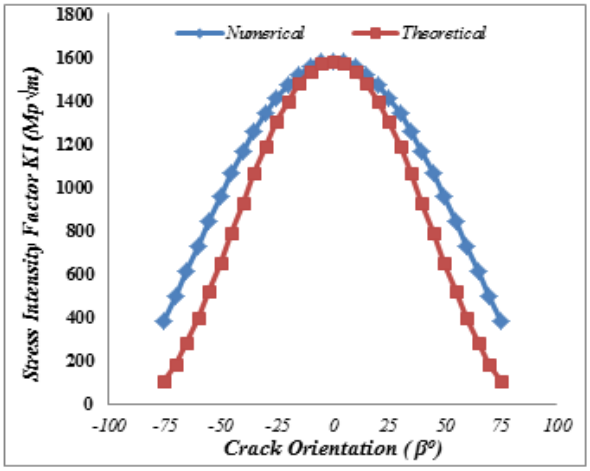

Figure 13: Variation of KI with the crack Orientation β^o.

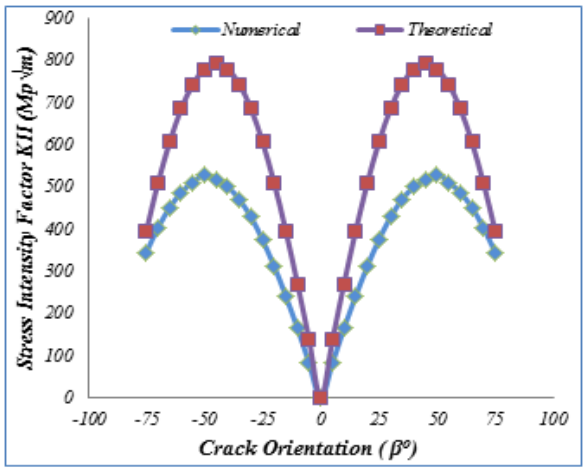

Figure 14: Variation of KII with the crack Orientation β^o.

3.5. Effect of the DENT inclination angle with kinked on the KI_A and KII_A

Figures 15 and 16 illustrate a compression between theoretical and numerical of KI_A and KII_A values (KI_A and KII_A= KI and KII at crack tip A, respectively as shown in Figure 6g) with variation of crack orientation plus kink angles ((α+β) = 0^o, 15^o, 30^o, 45^o, 60^o, 75^o, 80^o, 85^o and 90^o)) at crack angle (β = 15^o). From Figure 15 , it can be seen that there is a considerable effect between two curves when α < 0^o after that, the difference decreases slightly and vanished at α > 60^o. In the other hand, From Figure 16, it is clear that there in no significant difference between theoretical and numerical values at α≤45^obut the difference slightly increase after this angle.

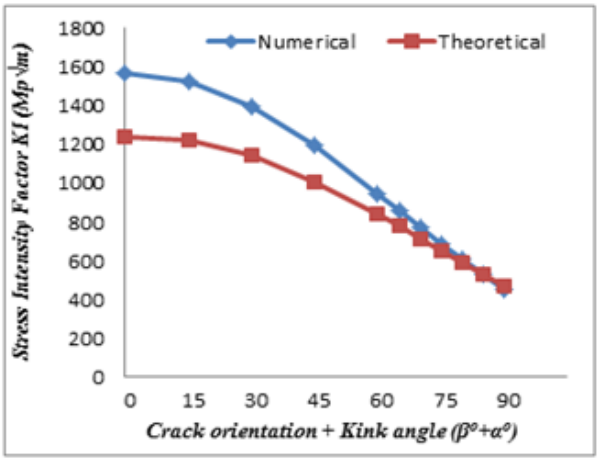

Figure 15: Theoretical and numerical variation of KI with the (β^o+α^o) for (β^o=15^o).

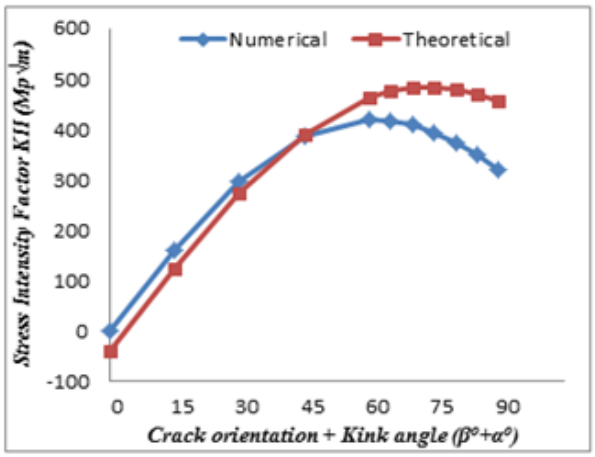

Figure 16: Theoretical and numerical variation of KII with the(β^o+α^o) for (β^o=15^o).

Furthermore, the variation of KI_A and KII_A with the ((α+β) = 0^o, 15^o, 30^o, 45^o, 60^o, 75^o, 80^o, 85^o and 90^o) at crack angles (β = 15^o, 45^o and 75^o) are explained in the Figures 17 and 18, respectively. Figure 17 illustrates that the increasing in the angles β and (β+α) lead to slightly decrease in the KI_A values while, from figure 18, it can be seen that the increasing

in the β lead to decrease in KII_A values. In addition, KII_A increases with the increase of (β+α) angles until 60^o and then it starts decreasing. Hence, maximum value of KI_A and KII_A occur at when (β+α) = 0^o and 60^o, respectively. In fact, the mixed mode crack (crack with mode I and II) become a mode I crack only due to the crack tend to propagate perpendicular to the applied normal stress.

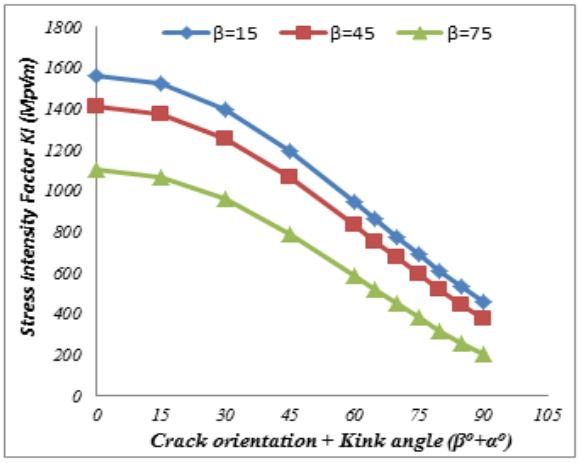

Figure 17: Numerical variation of KI with the (β^o+α^o) for different β^o.

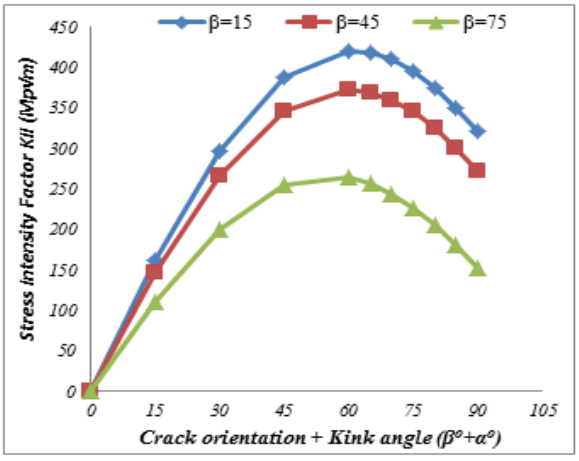

Figure 18: Numerical variation of KII with the (β^o+α^o) for different β^o.

Furthermore, Figures 19 and 20 are graphically illustrated Von-Mises stresses countor plots with the variation of the locations and angle of the crack. Figures 19a, b, c, d, and e explain the variation of Von-Mises stresses for DENT in the middle of the plate length, near the plate edge, parallel cracks, with angle and with kinked, respectively while the variation of Von-Mises stresses with different values of crack and kinked angles are illustrate in the Figures 20a, b, c, d and e. From these figures, it is clear that all cases mentioned above have a considerable effect on the plate stresses.

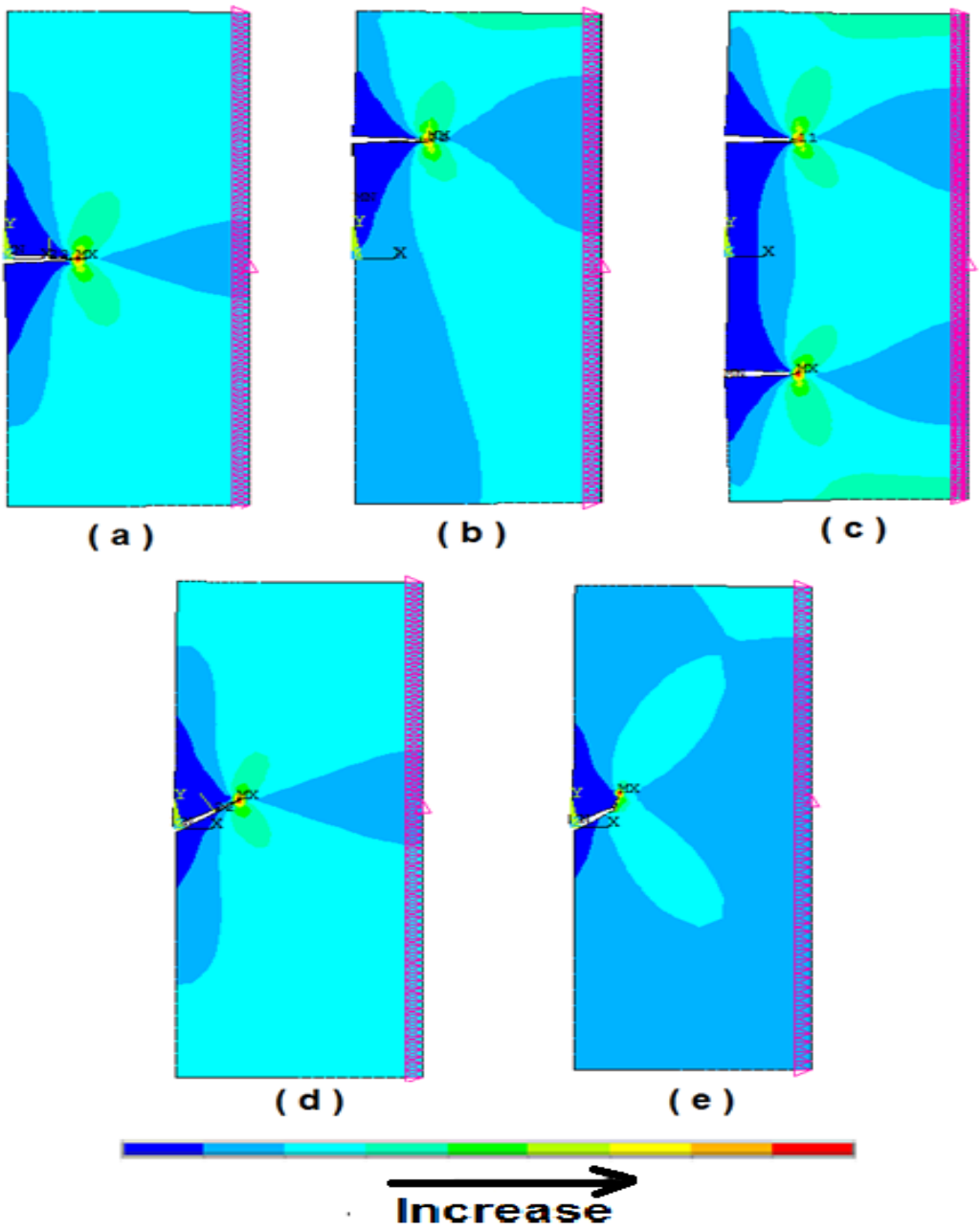

Figure 19: Countor plots of Von-Mises stress with the variation for double edge crack for different cases.

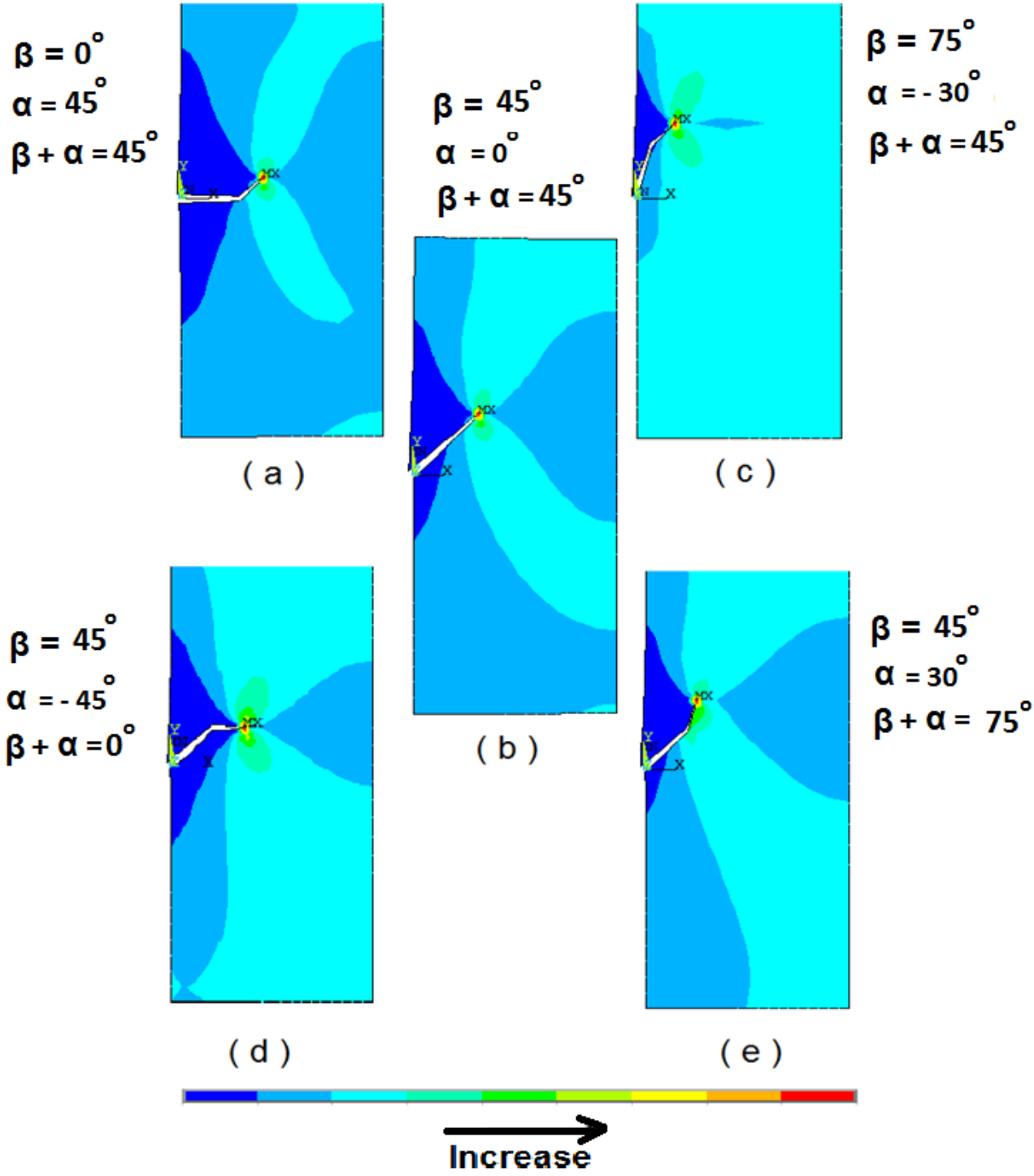

Figure 20: Countor plots of Von-Mises stress for different double edge crack orientations and kink angles.

4. CONCLUSIONS

The following conclusion can be drawn from the present study:

1- In all studied cases, a good agreement is observed between the theoretical and numerical results with a maximum discrepancy of 0.79%.

2- KI increases with increasing the relative crack length and tensile stress and when the crack position draw near the plate edge but this value decreased in the case of two parallel cracks as a result of the mutual shielding effect KI reduces in each crack.

3- The maximum values of KI and KII occur at crack angle $\beta=0^o$ and 45^o, respectively. In addition, KII vanished at $\beta = 0^o$ and 90^o while KI vanished at $\beta = 90^o$.

4- In kinked crack case, the maximum value of KI_A and KII_A occur at $(\beta+\alpha) = 0^o$ and 60^o, respectively. It was seen that the orientation of the kinked crack have a significant effects on the KI and KII.

5. REFERENCES

1. Z.Ali,K.E.S.Meysam, AsadiIman, B. Aydin, B.Yashar. Finite Element Method Analysis of Stress Intensity Factor in Different Edge Crack Positions, and Predicting their Correlation using Neural Network Method. Research Journal of Recent Sciences, Vol. 3(2), 69-73, 2014.
2. N. A. H. Saleh. A Study on Second Mode Stress Intensity Factor (KII) of Cracked Plates under Compression Load. Basrah Journal for Engineering Science, pp. 54-65, 2012.
3. D. Arencón and J. I. Velasco. Review, Fracture Toughness of Polypropylene-Based Particulate Composites. Journal of Materials, Vol. 2, pp. 2046-2094, 2009.
4. O. L. Bowie. Analysis of an Infinite Plate Containing Radial Cracks Originating at the Boundary of an Internal Circular Hole “, Journal of Math. & Phys. (MIT), Vol. 35, pp. 60-71, 1956.
5. J. C. Newman. An Improved Method of Collocation for the Stress Analysis of Cracked Plates with Various Shaped Boundary. NASA Technical Note TN D-6376, Langley Research Center, Hampton, VA, 1971. Aavailable at http://hdI.handle.net/2060/19710022830.
6. Y. Murakami. A Method of Stress Intensity Factor Calculation for the Crack Emanating from a Arbitrarity Shaped Hole or the Crack in the Vicinity of an Arbitrarity Shaped Hole. Trans. Jpn. Soc. Mech. Eng., Vol. 44:378, pp. 423-432, 1978.
7. M. Isida and Y. Nakamura. Edge Cracks Originating from an Elliptical Hole in a Wide Plate Subjected to Tension and in – Plan Shear. Trans. Jpn. Soc. Mech. Eng., VoL. 46:409, pp. 947-956, 1980.

8. A.K. Yavuz, S.L. Phoenix and S.C. TerMaath. An Accurate and Fast Analysis for Strongly Interacting Multiple Crack Configurations Including Kinked (V) and Branched (Y) Cracks. International Journal of Solids and Structures, Vol. 43, pp. 6727–6750, 2006.
9. D. F. Li, C. F. Li, H. Qing and J. Lu. The ElasticT-stress for Slightly Curved or Kinked Cracks. International Journal of Solids and Structures, Vol. 47, pp. 1753–1763, 2010.
10. F.V. Antunes, A.G. Chegini ,L.M. Correia and A.L. Ramalho. Effect of Crack Propagation on Crack Tip Fields. Frattura ed Integrità Strutturale, Vol. 25, pp. 54-60, 2013.
11. A. Spagnoli, A. Carpinteri and S. Vantadori. On a Kinked Crack Model to Describe the Influence of Material Microstructure on Fatigue Crack Growth. Frattura ed Integrità Strutturale, Vol. 25, pp. 94-101, 2013.
12. N. R. Mohsin. Comparison between Theoretical and Numerical Solutions for Center, Single Edge and Double Edge Cracked Finite Plate Subjected to Tension Stress. International Journal of Mechanical and Production Engineering Research and Development (IJMPERD), Vol. 5(2), pp. 11-20, 2015.
13. A. Fatemi. Fundamentals of LEFM and Applications to Fatigue Crack Growth –Chapter 6-LEFM & Crack Growth Approach. Available at https://www.efatigue.com/training/Chapter_6.pdf .
14. C. Rae. Natural Sciences Tripos Part II- Materials Science- C15: Fracture and Fatigue. Available at https://www.msm.cam.ac.uk/teaching/partII/courseC15/C15H.pdf .
15. V. E. Saouma. Lecture Notes in:Fracture Mechanics – Chapter 4, 2000. Available at http://civil.colorado.edu/~saouma/Lecture-Notes/lecfrac.pdf.
16. T.L.Anderson. Fracture Mechanics Fundamentals and Applications. Third Edition, Taylor &Francis Group, CRC Press, 2005.
17. G. C. Sih, P. C. Paris and G. R. Irwin. On Crakes in Rectilinearly Anisotrpic Bodies. International Journal of fracture Mechanics, Vol. 1, pp. 189-302, 1965.
18. S. G. Kulkarni. MachineDesign. McGraw-Hill Companies, Sixth Reprint, New Delhi, 2012.
18. A. A. Nassar. Evaluation of Critical Stress Intensity Factor (K_{IC}) for Plates Using New Crack Extension Technique. Eng. & Tech. Journal, Vol. 31, No. 4, 2013.
19. H. Tada, P. C. Paris and G. R. Irwin. The Stress Analysis of Cracks Handbook. Third Edition, ASME presses, 2000.
20. ANSYS. Release 15. Documentation.